Estimating Turbulence Statistics and Parameters from Ground- and Nacelle-Based Lidar Measurements

IEA Wind Expert Report

Sathe, Ameya; Banta, Robert ; Pauscher, Lukas ; Vogstad, Klaus ; Schlipf, David; Wylie, Scott

Publication date:
2015

Document Version
Publisher's PDF, also known as Version of record

Estimating Turbulence Statistics and Parameters from Ground- and Nacelle-Based Lidar Measurements

IEA Wind Expert Report

IEA Wind Task 32
Expert Report
2015

Lead Author: Ameya Sathe (DTU Wind Energy, Denmark)

Co-Authors:
Robert Banta (National Oceanic and Atmospheric Administration , USA)
Lukas Pauscher (Fraunhofer IWES, Germany)
Klaus Vogstad (Meventus, Norway)
David Schlipf (University of Stuttgart, Germany)
Scott Wylie (ZephIR Ltd., UK)

October 2015

Title: Estimating Turbulence Statistics and Parameters from Ground-Based Lidar Measurements

Organization: International Energy Agency Wind Implementing Agreement

Foreword: The International Energy Agency Implementing Agreement for Co-operation in the Research, Development and Deployment of Wind Energy Systems (IEA Wind) is a vehicle for member countries to exchange information on the planning and execution of national, large-scale wind system projects and to undertake co-operative research and development projects called Tasks or Annexes.
As a final result of research carried out in the IEA Wind Tasks, Recommended Practices, Best Practices, or Expert Group Reports may be issued. These documents have been developed and reviewed by experts in the specialized area they address. They have been reviewed and approved by participants in the research Task, and they have been reviewed and approved by the IEA Wind Executive Committee as guidelines useful in the development and deployment of wind energy systems. Use of these documents is completely voluntary. However, these documents are often adopted in part or in total by other standards-making bodies.
A Recommended Practices document includes actions and procedures recommended by the experts involved in the research project.
A Best Practices document includes suggested actions and procedures based on good industry practices collected during the research project.
An Experts Group Studies report includes the latest background information on the topic as well as a survey of practices, where possible.
Previously issued IEA Wind Recommended Practices, Best Practices, and Expert Group Reports can be found here on the Task 11 web pages.

October 2015

Grant no: 0602-02486B

Sponsorship:
Danish Ministry of Science, Innovation and Higher Education - Technology and Production

Approved by:
IEA Executive Committee
Paris, October 2015

Pages: 111

ISBN: 978-87-93278-35-6

DTU Wind Energy
Frederiksborgvej 399
4000 Roskilde
www.vindenergi.dtu.dk

Executive Summary

The purpose of this summary is to provide brief suggestions on how this report could be useful, either to the industry or a research institution. First and foremost it is to be noted that this report is not a recommended practice. Therefore, this report does not provide a step-by-step procedure on how to use lidars for performing turbulence measurements.

Instead this report provides a detailed overview of the current state-of-the-art with regards to characterizing atmospheric turbulence from lidar measurements. Discussion on some of the commonly asked questions by the industry has been carried out. For example, the readers could get a brief idea of how the turbulence statistics, lidar measurements and wind energy applications are related to each other. The readers could potentially benefit from a comprehensive discussion on several commercial and research lidar measurement configurations, which clearly outlines the benefits and shortcomings of each of them with regards to turbulence estimation. Description and analysis of a number of experimental campaigns from across the world could provide a deeper understanding of the real-world turbulence measurements from lidars.

Preface

This expert report is prepared as a written contribution to the IEA task 32 activity, that was carried out withing the framework of the International Energy Agency. The goal of this report is to provide an overview of the state-of-the-art with regards to estimating turbulence statistics from lidar measurements, as well as providing experimental evidence from different measurement campaigns from across the world. It is to be noted that this report by no means contains an exhaustive list of the measurement campaigns that have focused on atmospheric turbulence analysis. The list of the measurement campaigns is limited to that contributed by the participants of this task. Objectively the attempt is to provide the readers with answers to two questions:

1. With the existing technology and knowledge, can we routinely use wind lidars to estimate turbulence statistics?

2. What improvements in the existing lidar technology and knowledge are required in order to estimate turbulence statistics, where the degree of accuracy and precision is comparable to that estimated using the traditional meteorological mast anemometry?

The report is structured such that each chapter is as independent as possible of each other (except chapter 1). A reader that is interested in only a specific topic can skip other chapters and simply jump to the concerned chapter without much loss of information.

A report on turbulence measurements is impossible without providing some basic mathematical terminology. Therefore in chapter 1, basic turbulence terminology is defined and used in the rest of the report. It is highly recommended that the reader goes through the definitions and familiarizes with the notations in this chapter, since they will be frequently used in the remaining chapters. A reader familiar with the basic terminology can simply skip this chapter and refer to the nomenclature provided at the beginning of this report. Consistency of the notations is maintained as much as possible throughout the report. However, there might be instances, particularly in chapter 5, where it is sometimes difficult to maintain the consistency owing to the international nature of the report. On those occasions reference to the equivalent notations used in this report is made in order to avoid confusion.

Chapter 2 begins with the motivation of using lidars to estimate turbulence statistics, followed by basics of coherent Doppler lidars with regards to two different technologies, namely the continuous wave and the pulsed lidars. A brief description of the turbulence statistics relevant for wind energy is also provided.

In chapter 3, illustrations of different measurement configurations are provided, where further division is made between the commercial and research configurations. Some of these illustrations are referred to in chapters 4 and 5, where the reader who has not gone through the description of these configurations can simply refer to the respective figures. Additionally for some of the measurement configurations, mathematical formulations are provided for different turbulence parameters. Although a bit complicated, we believe that this will further help the readers in understanding what is possible with the respective measurement configurations in terms of estimating turbulence parameters.

Chapter 4 provides a review of the state-of-the-art with regards to estimating turbulence statistics using lidar measurements. The review is performed by grouping the turbulence statistics, where the definitions introduced in chapter 1 are used.

In chapter 5, results from different measurement campaigns across the world are provided. This chapter is divided into several studies. The structure of each study is consistent such that the goals are described at first, followed by detailed information of the measurement campaign. As far as possible uniformity in describing the measurement campaigns is maintained. Comparisons of the estimated first- and second-order statistics is described subsequently. It is to be noted that for almost all studies, information regarding uncertainty of the reference instruments was not available. It therefore becomes difficult to assess the true potential of lidar measurements in estimating turbulence statistics. Nevertheless standard instruments such as the cup and sonic anemometers have been mainly used as reference instruments, which provide confidence in the comparisons with lidar measurements.

The report ends with chapter 6, where an attempt is made to answer the aforementioned questions. A section on future perspectives specifically tackles the second question stated above.

It is quite likely that in the due course of preparation of the report, the authors have missed some of the important recent studies on lidars and turbulence. However, given the magnitude of the task, it is simply impossible to include all the relevant studies and be up-to-date. Therefore we express our regret beforehand for having missed such important works. We hope that with the studies included in this report, the readers would get a fair understanding of the (relatively) current status of turbulence characterization from lidar measurements.

An international report of this nature is simply not possible without the contribution of international participants. To this end, as the leader of this report, I would like to express my sincere thanks to all the participants of this work package, and especially to those who actively contributed with the written material and became co-authors. The final contents of the report have been approved by the participants.

The quality of any written contribution can only be assessed and improved with an independent peer review by international experts. Therefore I extend my heartfelt gratitude to the three international experts in this topic, Dr. Alfredo Peña and Prof. Jakob Mann from DTU Wind Energy, Denmark, and Dr. Jennifer Newmann from NREL, USA, for meticulously going through the report and providing valuable feedback. The quality of this report has certainly improved due to their feedback. Furthermore, comments from the participants, both from the research institutions and the industry are highly appreciated.

October, 2015

Place: Roskilde, Denmark

Name: Ameya Sathe

Nomenclature

$C \approx 1.5$	universal Kolmogorov constant
$C_2 \approx 2$	Kolmogorov constant related to $D_{11}(r_1)$
$D_{ij}(\boldsymbol{r})$	velocity structure function
$F_{ij}(k_1)$	one-dimensional velocity spectrum
I	longitudinal turbulence intensity
L_p	range gate length ($c\tau/2$)
$R_{ij}(\boldsymbol{r})$	cross covariance function
$\mathbf{R} = \mathbf{R}(0)$	covariance matrix
$\boldsymbol{k}$	wave vector in the Fourier domain
$\boldsymbol{n}$	unit directional vector
$\boldsymbol{r}$	separation vector in three dimensions
$\boldsymbol{x}$	position vector in three dimensions
$\mathrm{coh}_{ij}(k_1)$	coherence function
$\langle S(v_\mathrm{r})\rangle$	mean Doppler spectra
$\langle u\rangle$	mean wind speed
$\langle u'^2\rangle$	variance of the u component
$\langle u'v'\rangle$	covariance between the u and v components
$\langle u'w'\rangle$	covariance between the u and w components
$\langle v_\mathrm{r}'^2\rangle$	radial velocity variance
$\langle v'^2\rangle$	variance of the v component
$\langle v'w'\rangle$	covariance between the v and w components
$\langle w'^2\rangle$	variance of the w component
$\langle w'^3\rangle$	third moment of the vertical velocity
$\mathbf{v}$	wind vector
$\tilde{D}(\delta)$	filtered radial velocity structure function for a separation distance $d_f\delta$
$\tilde{D}(r)$	filtered radial velocity structure function for a separation distance r
$\tilde{D}(r_1)$	filtered radial velocity structure function for a separation distance r_1
$\tilde{F}(k_1)$	filtered radial velocity spectrum
$\tilde{R}(r)$	filtered covariance function of the radial velocity for a separation distance r
c	speed of light
d_f	focus distance for a C-W lidar and center of the range gate for a pulsed lidar
$i,\ j$	indices that take values $1, ., 3$ and denote the component of the wind vector

k_1, k_2, k_3	components of the wave vector along the x_1, x_2, x_3 axes respectively
l	Rayleigh length
r	separation distance along the lidar beam
r_1, r_2, r_3	separation distances along the x_1, x_2, x_3 axes respectively
r_b	lidar beam radius
u	longitudinal component of the wind vector in the x_1 direction
v	transversal component of the wind vector in the x_2 direction
v_r	radial velocity
w	vertical component of the wind vector in the x_3 direction
w_p	pulse width
x_1, x_2, x_3	axes defining the right handed cartesian coordinate system
z	height above the ground
$\mathscr{L}$	outer length scale of turbulence
$\Phi_{ij}(\boldsymbol{k})$	three-dimensional spectral velocity tensor
β	angle between the lidar beam and the mean wind
Θ	mean wind direction
α	elevation angle
$\chi_{ij}(k_1, r_2, r_3)$	cross spectra at separation distances r_2 and r_3
δ	angle subtended by two lidar beams in a VAD scanning mode
ℓ_{ij}	integral length scale
$\langle \sigma_\mathrm{s}^2 \rangle$	second central moment of the Doppler spectrum (Doppler spectrum width)
ϕ	zenith angle
g	acceleration due to gravity
L	Obukhov Length
u_*	friction velocity
θ_v	virtual potential temperature
$\overline{w'\theta'_v}$	surface virtual kinematic heat flux
κ	von Kármán constant
τ	pulse duration
λ_b	wavelength of the emitted radiation
θ	azimuth angle
ε	energy dissipation rate
RHI	range height indicator
VAD	velocity azimuth display
CW	continuous-wave

Contents

Chapter 1

Mathematical Preliminaries

The main purpose of writing this chapter is to introduce the mathematical notations and concepts, which would be helpful in understanding the following chapters.

Turbulence statistics are usually described in some standard coordinate system. If the selection of a coordinate system is left at the prerogative of the scientist or an engineer performing the measurement, then interpreting turbulence statistics would be very cumbersome. Fortunately in the meteorological world, a consensus has been achieved where the wind vector components are described in a coordinate system such that one of its components is in the mean wind direction. In some literature [Wilczak et al., 2001], such a coordinate system is also called as the streamline coordinate system. Therefore at first we define the base coordinate system to be right-handed as shown in Fig. 1.1, where the x_1 axis can be considered to be pointing east, the x_2 axis can be considered to be pointing north, and x_3 axis can be considered to be pointing vertically upwards. The mean wind direction is shown to make a positive angle Θ with respect to the x_2 axis, i.e. north in the clockwise direction such that a wind direction of 0° denotes the wind blowing from north to south. It is to be noted that throughout the report the upper-case Θ refers to the wind direction, whereas the lower-case θ refers to the azimuthal angle of the lidar beam (defined in chapter 3).

Measurements of components of the wind vector are usually carried out in arbitrary base coordinate system. It is therefore necessary to perform a coordinate transformation on the measured wind vector components in the some arbitrary base coordinate system such that the final coordinate system is aligned with the streamline coordinate system. However to avoid increasing the complexity of equations by the introduction of the rotation matrices, in the rest of the report it is assumed that the streamline coordinate system is aligned with the base coordinate system.

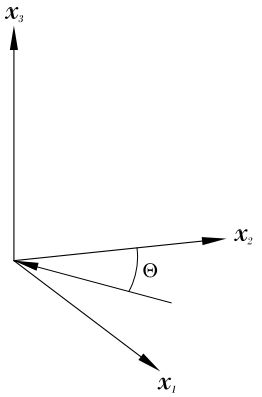

Figure 1.1: Standard meteorological convention of depicting the mean wind direction

In this report we will often switch between the bold faced vector notation and the Einstein indical notation. We define the wind vector as $\mathbf{v} = (u, v, w)$, such that u (longitudinal component) is in the mean wind direction, v (transversal component) is perpendicular (in a right-handed system) to the mean wind direction, and w is in the vertical x_3 direction. If we consider that the fluctuations of the wind vector are homogeneous in space, i.e. the statistics of turbulence do not change in space, then the auto or cross covariance functions can be defined only in terms of the separation distance as,

$$R_{ij}(\boldsymbol{r}) = \langle \mathrm{v}_i'(\boldsymbol{x})\mathrm{v}_j'(\boldsymbol{x}+\boldsymbol{r})\rangle, \tag{1.1}$$

where $R_{ij}(\boldsymbol{r})$ is the auto or cross correlation function, $i,\ j = (1,2,3)$ are the indices corresponding to the components of the wind vector, $\boldsymbol{x}$ is the position vector in the three dimensional Cartesian coordinate system, $\boldsymbol{r} = (r_1, r_2, r_3)$ is the separation vector, $\langle\rangle$ denotes ensemble averaging, and $'$ denotes fluctuations about the ensemble average. Eq. (1.1) denotes a two-point turbulent statistic. At $\boldsymbol{r} = 0$ we then get a single-point turbulent statistic, which we can denote as the variances and covariances. In matrix form it can be written as,

$$\mathbf{R} = \begin{bmatrix} \langle u'^2\rangle & \langle u'v'\rangle & \langle u'w'\rangle \\ \langle v'u'\rangle & \langle v'^2\rangle & \langle v'w'\rangle \\ \langle w'u'\rangle & \langle w'v'\rangle & \langle w'^2\rangle \end{bmatrix}, \tag{1.2}$$

where the diagonal terms are the variances of the respective wind vector components and the off-diagonal terms are the covariances. Here, it is implied that $\mathbf{R} = \mathbf{R}(0)$, and we drop the argument and the bracket for simplicity. In wind energy, one frequently used statistic is the turbulence intensity, which according to the IEC [2005a] standards is defined as,

$$I = \frac{\sigma_u}{\langle u\rangle}, \tag{1.3}$$

where I is the turbulence intensity, and $\sigma_u = \sqrt{\langle u'^2\rangle}$ is the standard deviation of the horizontal (or the longitudinal component) wind speed. From the definition of $\boldsymbol{R}(\boldsymbol{r})$ and $\boldsymbol{R}$, we can define integral length scale as,

$$\ell_{ij} = \frac{1}{R_{ij}} \int_0^\infty R_{ij}(r_1)\ dr_1, \tag{1.4}$$

which can be interpreted as the distance over which turbulent fluctuations remain correlated. Similar to $R_{ij}(\boldsymbol{r})$, another useful two-point statistic to characterize turbulence is the velocity structure function, which is defined as,

$$D_{ij}(\boldsymbol{r}) = \langle (\mathrm{v}_i'(\boldsymbol{x}+\boldsymbol{r}) - \mathrm{v}_i'(\boldsymbol{x}))(\mathrm{v}_j'(\boldsymbol{x}+\boldsymbol{r}) - \mathrm{v}_j'(\boldsymbol{x}))\rangle. \tag{1.5}$$

On many occasions it is convenient to study turbulence in the Fourier domain instead of the time domain. To this extent, we can define the spectral velocity tensor (or the three-dimensional spectral density) as the Fourier transform of $R_{ij}(\boldsymbol{r})$,

$$\Phi_{ij}(\boldsymbol{k}) = \frac{1}{(2\pi)^3} \int R_{ij}(\boldsymbol{r}) \exp(\mathrm{i}\ \boldsymbol{k}\cdot\boldsymbol{r})\ d\boldsymbol{r}, \tag{1.6}$$

where $\Phi_{ij}(\boldsymbol{k})$ is the three-dimensional spectral velocity tensor, $\boldsymbol{k} = (k_1, k_2, k_3)$ is the wave vector, and $\int d\boldsymbol{k} = \int_{-\infty}^{\infty}\int_{-\infty}^{\infty}\int_{-\infty}^{\infty} dk_1\ dk_2\ dk_3$. From Eq. (1.6) it is obvious that $R_{ij}(\boldsymbol{r})$ is the inverse Fourier transform of $\Phi_{ij}(\boldsymbol{k})$. A single-point statistic is then given as,

$$R_{ij} = \int \Phi_{ij}(\boldsymbol{k})\ d\boldsymbol{k}. \tag{1.7}$$

Practically, it is not possible to measure a spectral velocity tensor, since we would need measurements at all points in a three-dimensional space. A one-dimensional velocity spectrum is then used, which is defined as,

$$F_{ij}(k_1) = \frac{1}{2\pi}\int_{-\infty}^{\infty} R_{ij}(r_1)\exp(-\mathrm{i}k_1 r_1)\ dr_1 \tag{1.8}$$

$$= \int_{-\infty}^{\infty}\int_{-\infty}^{\infty} \Phi_{ij}(\boldsymbol{k})\ dk_3 dk_2. \tag{1.9}$$

Alternatively, one can use a semi-empirical turbulence model [Mann, 1994]. In this model, the turbulence structure in the neutral atmospheric surface layer is characterized by $\Phi_{ij}(\boldsymbol{k})$, which is quantified as a function of only three parameters, $C\varepsilon^{2/3}$, a product of the universal Kolmogorov constant $C \approx 1.5$ [Pope, 2000] and the turbulent kinetic energy dissipation rate to the two-third power $\varepsilon^{2/3}$, the outer length scale of turbulence $\mathscr{L}$, which is the length scale corresponding to the maximum spectral energy, and an anisotropy parameter. Another important statistic in the Fourier domain is the coherence function defined as,

$$\mathrm{coh}_{ij}(k_1) = \frac{|\chi_{ij}(k_1, r_2, r_3)|^2}{F_{ii}(k_1)F_{jj}(k_1)}, \tag{1.10}$$

where $\chi_{ij}(k_1, r_2, r_3)$ denotes the cross spectra between the components i and j, and $F_{ii}(k_1) = \chi_{ii}(k_1, 0, 0)$, $F_{jj}(k_1) = \chi_{jj}(k_1, 0, 0)$ (no summation over repeated indices) are the one-dimensional spectra of the i and j components respectively.

In turbulence studies it is common to classify the observations based on atmospheric stability. There are several ways to characterize atmospheric stability. In this report we characterize it by Obukhov length L, which can be physically interpreted as the height at which the mechanical rate of production of turbulence (due to friction at the surface) becomes equal to that of the buoyant rate of production of turbulence[Wyngaard, 2010]. Mathematically it is given as,

$$L = -\frac{{u_*}^3\theta_v}{\kappa g\overline{w'\theta'_v}}, \tag{1.11}$$

where u_* is the friction velocity, $\kappa = 0.4$ is the von Kármán constant, g is the acceleration due to gravity, θ_v is the virtual potential temperature and $\overline{w'\theta'_v}$ (covariance of w and θ_v)is the virtual kinematic heat flux. u_* is defined as [Wyngaard, 2010],

$$u_* = \sqrt[4]{\overline{u'w'}^2 + \overline{v'w'}^2}, \tag{1.12}$$

where $\overline{u'w'}$ (covariance of u and w) and $\overline{v'w'}$ (covariance of v and w) are the vertical fluxes of the horizontal momentum. The concept of θ_v is important since the atmosphere consists of moist and dry air, which influences the gas constants. For the ideal gas law to be valid one must resort to using the gas constant for moist air, which could be a bit cumbersome. Therefore the concept of virtual temperature is necessary, which denotes the temperature that the dry air must have in order to have the same pressure and density of the moist air. Having used virtual temperature the use of gas constant for dry air is then permitted. The term potential temperature denotes the temperature that the air parcel will have if it is adiabatically brought down to a standard reference pressure. It takes care of the variations in temperature due to altitude differences. Combining the concept of virtual temperature and potential temperature leads to virtual potential temperature. For mathematical details the reader is referred to [Stull, 1988].

Chapter 2

Introduction

Wind turbines have been and will be installed in different parts of the world where atmospheric conditions differ significantly from each other. Understanding and measuring atmospheric turbulence is vital to efficient harnessing of wind energy and to estimating the structural integrity of a wind turbine. Traditionally, meteorological mast (met-mast) anemometry has been used; in this method, either cup or sonic anemometers are mounted on slender booms at one or several heights to measure turbulence over a certain period of time. For wind energy purposes, much interest is focused on the turbulence of the wind, although some attention is also paid to other atmospheric variables such as temperature, pressure, humidity, density, etc. Particularly the turbulent temperature fluctuations are used to characterize atmospheric stability.

Turbulence affects the wind turbines mainly in two ways: first, the fluctuations that are caused in the extracted wind power [Gottschall and Peinke, 2008, Kaiser et al., 2007], and second, the fluctuations in the loads on different components of a wind turbine [Sathe et al., 2013]. These fluctuations result in inefficient harnessing of wind energy and have the potential to inflict fatigue damage. Wind turbines are generally designed for a period of twenty years [Burton et al., 2001, IEC, 2005a], with fatigue loads significantly reducing the design lifetime.

The size of a wind turbine has grown significantly over the past few decades such that the upper tip of a modern wind turbine blade can easily reach heights up to 200 m above the ground. Thus, measuring and understanding the turbulent wind field at higher heights is essential. It is very expensive to install and operate a met-mast at such heights for a sustained period of time; especially offshore, the costs increase significantly owing to the large foundation needed to support the met-mast. Moreover, a met-mast cannot be moved from one place to another, thus limiting the physical range of the studies. Because of all these factors, collecting measurements at different locations on a wind farm site (e.g. to study turbine wakes) or at heights that extend to the top of a turbine rotor disk, becomes quite a challenge. Lidars have the potential to counter these disadvantages of the met-mast anemometry. Doppler lidars have been used extensively to measure the mean wind speed and wind profiles in a variety of studies and locations [Banta et al., 1992, 1993, 1999, 2002, 2013, Darby et al., 1999, 2006, Hall et al., 1984, Kindler et al., 2007, Peña et al., 2009, Smith et al., 2006, Wagner et al., 2011]. However, despite having been researched for years all over the world (particularly for meteorological studies), lidars have not yet been accepted for turbulence measurements. Lidars' lack of acceptance can be attributed to several reasons, such as large measurement volumes leading to spatial averaging of turbulence along the line-of-sight of its measurement axis, cross-contamination by different components of the wind vector, low sampling rates, etc. In order for lidars to be widely accepted for turbulence measurements, these factors must be carefully considered and quantified.

2.1 Basics of lidars

The introduction to this section was contributed by Chris Slinger from ZephIR Ltd. There are many different types of lidars, which are capable of performing a diverse range of tasks (e.g. 3D imaging and range finding, gas species detection, remote measurement of vibrations). In this report we restrict ourselves specifically with systems for the measurement of wind speed in the atmosphere. Such systems fall into two broad categories, namely the coherent lidars and direct detection lidars. Coherent lidar measures Doppler shifts by comparing the frequency of backscattered radiation to that of a reference beam via a light beating process, whereas direct detection lidar performs its frequency shift measurements by passing the light through an optical filter, such as a Fabry-Perot etalon. By operating in the ultra-violet, direct detection lidars can exploit molecular scattering processes, guaranteeing signal returns even in very clean air where there is an absence of scattering particles. Coherent wind lidar systems can be categorised according to their emission waveform (pulsed or continuous), waveband (visible, near-IR, far-IR), and their transmit/receive geometry (monostatic or bistatic). These notes concentrate specifically on continuous-wave (CW) and pulsed lidars, as these are the types of lidars most commonly used in wind energy studies.

2.1.1 Continuous Wave Lidar

The basic principle of a CW lidar is to focus a continually transmitting laser beam at a particular measurement height (range) so that the Doppler shift of the backscattered light from that range can be detected. If the motion of a particle along the beam direction is towards the lidar, it compresses the laser wavelength and increases its frequency (âĂIJblue shiftâĂİ), while movement away from the lidar stretches the wavelength and reduces the frequency ("red shift "). This frequency shift can be measured by mixing the backscattered signal with a small portion of the original beam, allowing the difference in frequency to be detected. The resulting signal will oscillate at the so called âĂIJbeatâĂİ frequency (the difference between the two signals being compared), which can be used to calculate the speed at which the particles are moving (i.e. the wind speed).

If more than one measurement height is to be interrogated, the CW lidar will adjust its telescope to focus on each of the heights in sequence. The ranges possible from any CW lidar are controlled by the focal properties of the systems optics. The focal depth of any telescope increases proportionally with the square of the distance to the measurement point of interest; the shorter the measurement distance, and the bigger the lens, the smaller the focal depth, where smaller focal depths are associated with less volume averaging of the subsequent radial velocity measurements. This optical property limits the maximum range that can be achieved with a CW lidar; current CW technologies produce wind speed measurements at ranges up to approximately 200 m. Beyond that range, the focal depth is too large to provide accurate wind speed measurements. The minimum range that a CW lidar can measure is very short (in principle it is zero) whereas a pulsed system is effectively blind while the pulse is leaving the transmitter. This leads to a minimum range in the order of tens of meters for pulsed system, something in the region of 40-50 m is common. It is for eye safety reasons that a minimum measurement range of around 10 m is used for CW systems.

Figure 2.1 depicts the basic operation of how a CW lidar measures the wind speed. Unlike in a pulsed system, which utilises the time of flight to distinguish between measurements at different ranges, a CW lidar operates at a given range by focusing its beam. Focusing of the beam results in a Lorentzian spatial weighting function along its axis, with a peak in the sensitivity located at the beam waist.

A single lidar measurement will only provide the component of wind speed along its beam

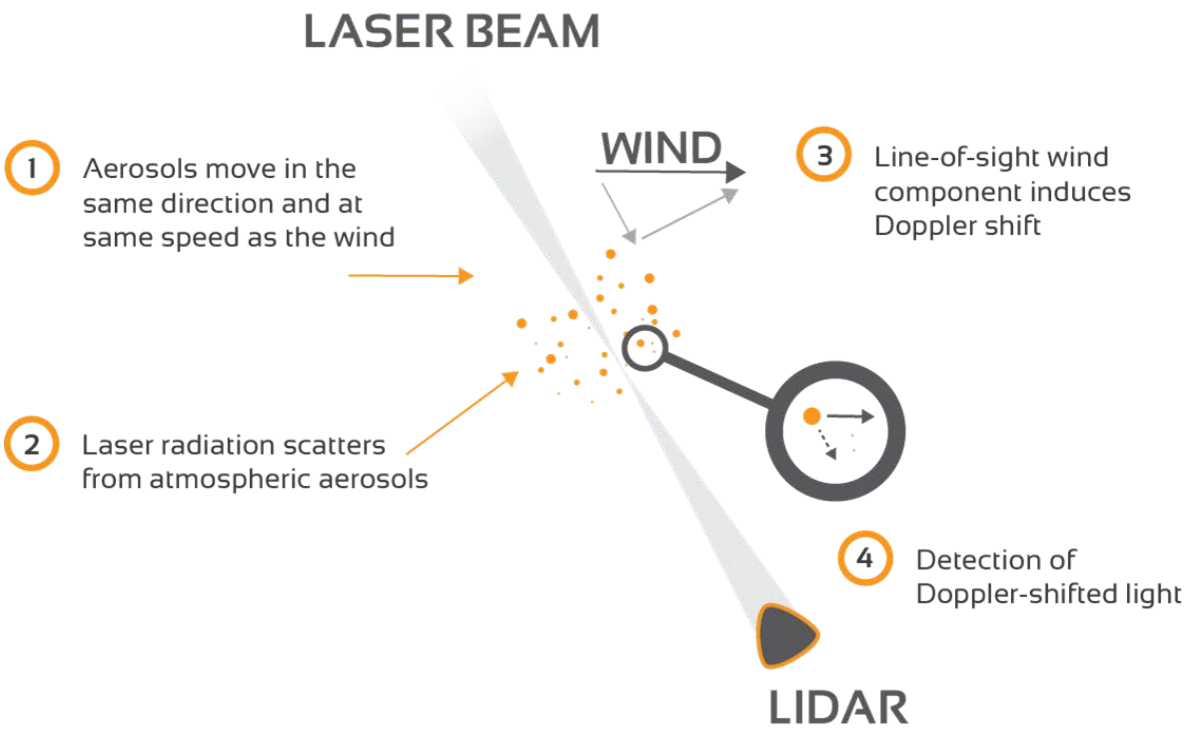

Figure 2.1: Principle of how a CW lidar detects backscatter from aerosols present in the atmosphere

axis, and it is for this reason why a scan is needed to generate a measurement of the wind speed vector. A conical scan pattern is common practice here. As the beam moves, it intercepts the wind at different angles and builds up a series of measurements around its scan perimeter, which are then used to derive the wind speed vector. The peak Doppler shift is detected when the angle of the azimuth scan aligns with the upwind and downwind direction of the wind, with a Doppler shift close to zero arising when the azimuth angle is perpendicular to the flow. In uniform flow, a plot of the measured line-of-sight wind speed against the azimuth angle takes the form of a cosine wave, which is rectified in the case of a homodyne lidar system that cannot distinguish the sign of the Doppler shift. The distribution of wind speed with height is then achieved through wind profiling, the process of continually conducting circular scans at each of the preset ranges in turn. The rapid sampling rate inherent to CW lidar gives rise to measurements on the order of one second per range.

2.1.1.1 Optics

Coupled with a transmitter and receiver (or transceiver in a homodyne system), the optics role is to provide a focused beam at a desired location. This location can be altered by changing the focus range or passing the beam through a scanning element such as a wedge (rotating prism). The angle of the wedge with respect to zenith, if used in a wind profiling setup, is usually of the order 30° but can change based on the specific application; e.g. a turbine mounted system may have a reduced wedge angle to account for its mounting position. If the CW lidar is a monostatic system then the backscattered light returns through the transmission optics, which can be isolated and then passed through the lidar for signal processing.

What is detected by the optics is the Doppler-shifted contribution generated by light scattering from any moving part of the atmosphere that is illuminated by the beam. The contribution from any point is weighted by the square of the intensity at that point. The

sensitivity of the focused beam is at its peak at the beam waist, and tails off symmetrically either side. To a good approximation the axial weighting function for a CW monostatic lidar is given by a Lorentzian function [Sonnenschein and Horrigan, 1971],

$$\varphi(s) = \frac{1}{\pi}\frac{l}{l^2 + s^2}, \tag{2.1}$$

where $\varphi(s)$ is the axial weighting function, s is the distance along the beam from the focus, and l is the Rayleigh length given as,

$$l = \frac{\lambda_\mathrm{b} d_\mathrm{f}^2}{\pi r_b^2}, \tag{2.2}$$

where λ_b is the wavelength of the emitted radiation, and r_b mm is the beam radius.

2.1.1.2 Backscattering

The backscattered light detected by a CW lidar experiences a Doppler shit in frequency given by,

$$\delta f = 2\frac{v_\mathrm{r}}{\lambda_\mathrm{b}} = 2\frac{v_\mathrm{r} f_\mathrm{b}}{c}, \tag{2.3}$$

where f_b is the frequency of the emitted radiation, v_r is the radial velocity, λ_b is the wavelength of the emitted radiation, and $c \approx 3 \times 10^8$ m/s is the speed of light. The backscattered signal detected by the lidar is made up of a range of different frequencies, which is a result of contributions from the different wind velocities (at strengths determined by the weighting function) measured over the probe length (space occupied by the focused lidar beam).

2.1.1.3 Beat Phenomena

The detected Doppler-shifted radiation is optically mixed with a reference beam (sometimes called the local oscillator), which leads to the creation of the well-known âĂIJbeatâĂİ phenomenon. Here the amplitude of the resulting signal oscillates at the difference frequency. For lidar, conveniently, this reduces the optical frequency of the Doppler shifted return from hundreds of GHz range to a signal more manageable in the MHz range. Detection of the âĂIJbeatâĂİ signal is achieved by directing the optically-mixed beam onto a photodetector that measures fluctuations in the light's intensity. The photodetector outputs a measurable current (or voltage) that can be amplified for signal processing.

2.1.1.4 Signal Processing

Figure 2.2 illustrates an example of signal processing for a CW lidar, but the details can vary from one lidar to the other. Spectral analysis is required to extract the relevant Doppler frequency information from the photodetector output, which for convenience is done digitally. The use of an analogue to digital convertor (ADC) with a sampling rate of 100 MHz allows spectral analysis up to a maximum frequency of 50 MHz, corresponding to peak $v_\mathrm{r} \approx 38.8$ ms^{-1} assuming use of a 30° wedge. Using digital Fourier transform (DFT), the spectra are analysed; a 512 point DFT gives rise to 256 points in the output spectrum with a bin width of ≈ 200 KHz, corresponding to v_r range of 38.8 m/s, and a resolution of approximately 0.16 m/s. Each of the line of sight measurements are sampled, representing ≈ 5 μs of data; successive DFTs are then calculated, and the resulting âĂIJvoltageâĂİ spectra are squared in order to generate a power spectrum. These power spectra are then averaged to find a mean spectrum for the averaging period. The random noise contained in the signal reduces with the square

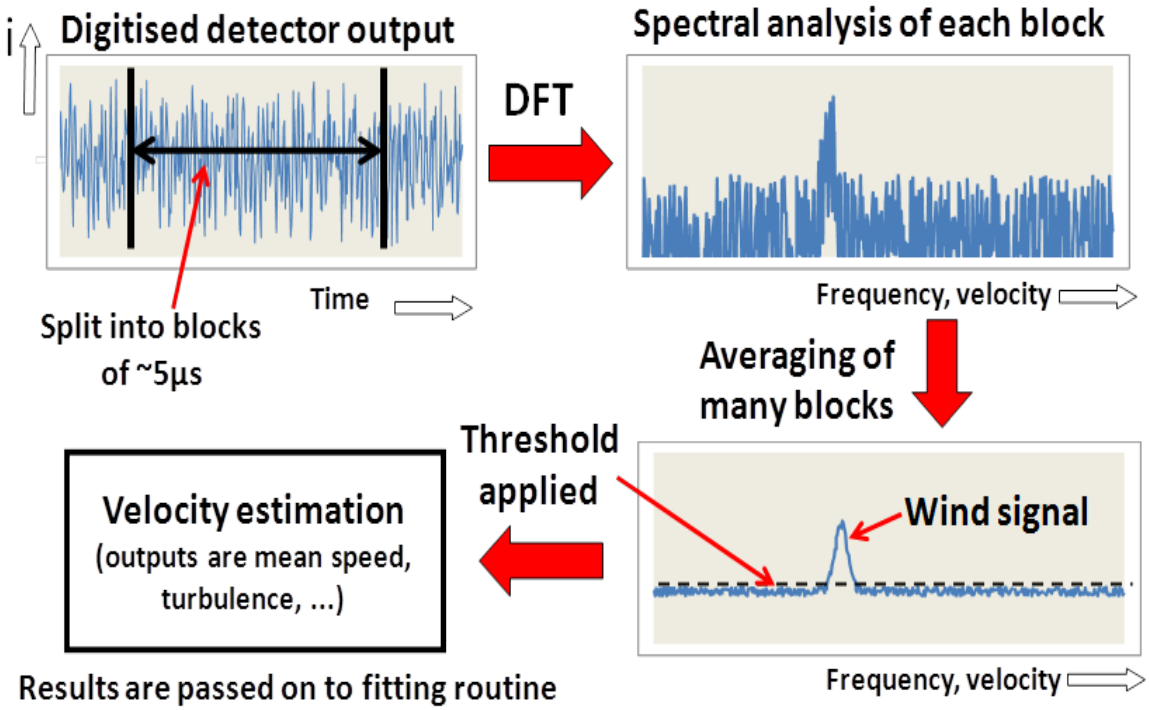

Figure 2.2: Typical signal processing stages undertaken to produce wind vector from line of sight measurements

root of the number of averages taken, with the sensitivity increasing by the same factor. Four thousand averages are taken for each line of sight measurement, which gives a data rate close to 50 Hz and a measurement time of around 20 ms. The width of the Doppler spectrum is determined by the following:

- Instrumental width – This is closely linked to the DFT bin width mentioned earlier
- Transit-time broadening – This is associated with the scan (assuming it is conical), the beam passes through the aerosols in a timescale of $\approx 10 - 15$ μs, corresponding to a broadening of the order 200 KHz
- Turbulence broadening – This is an effect from measuring over a volume, as opposed to point measurement such as a cup. When a large volume is probed in the atmosphere, a range of Doppler shifts can be detected, corresponding to parts of the atmosphere moving at different speeds. The impact of this is to have more than one peak in the detected spectrum. In general, this contribution will be increased during times of high turbulence and shear, meaning there is a potential to use this as an indication or measure of turbulence at a site.

2.1.2 Pulsed Lidar

The description of the operating principles of a pulsed lidar is taken from Vasiljevic [2014]. As described in chapter 1, the notations used in this section may differ slightly than the ones used in the rest of the report. However, this does not hinder the readability of the rest of the report, as consistent notations are used throughout. A coherent pulsed Doppler lidar performs three fundamental processes that enable measurements of the radial velocity:

Table 2.1: Type of laser pulses

Type	Wavelength (nm)	Temporal Length (ns)	Energy (μJ)	PRF (kHz)
Long	1543	400	100	10
Middle	1543	200	50	20

1. Emission of laser pulses
2. Acquisition of the backscattered light
3. Analysis of the acquired backscattered light

2.1.2.1 Emission of the laser light

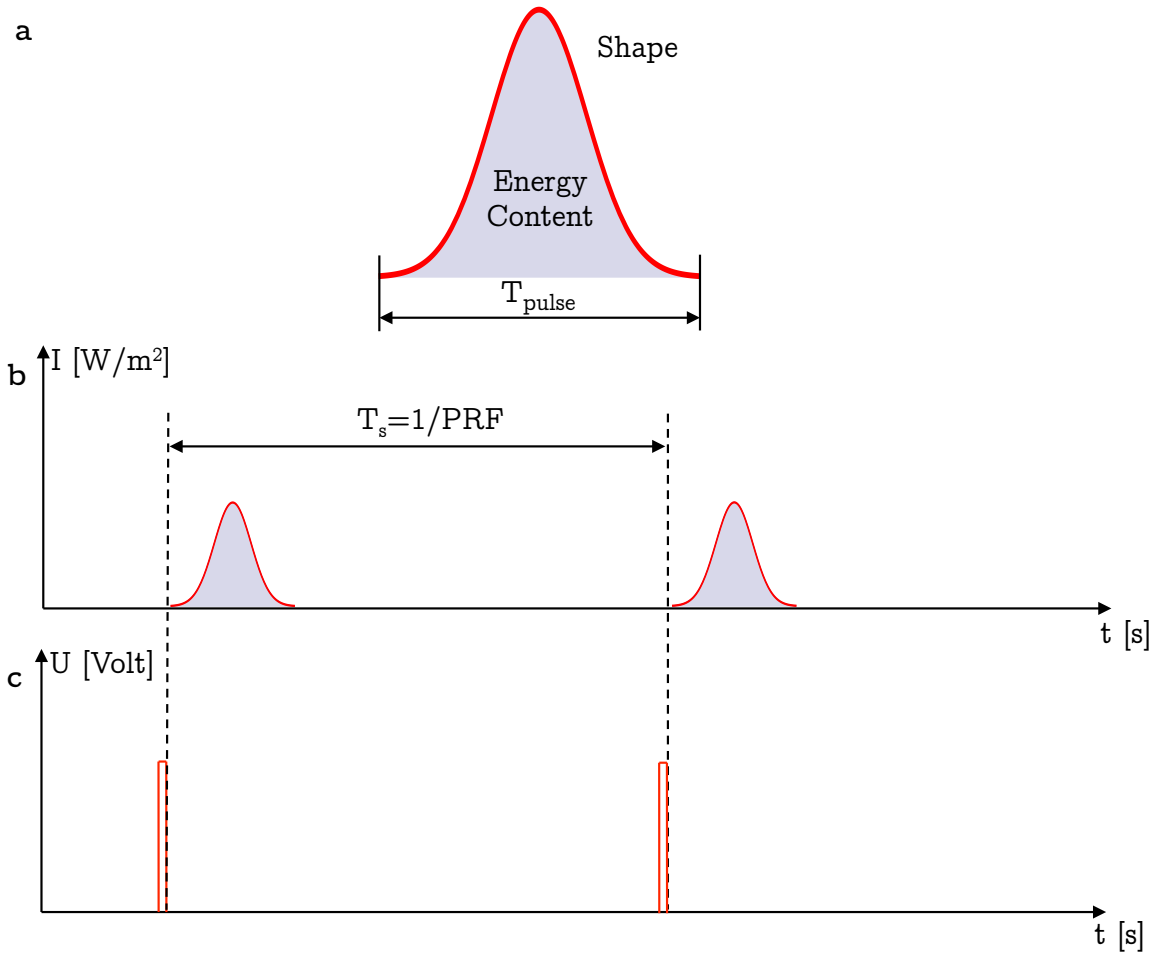

Figure 2.3: Emission: a - laser pulse, b - pulse train, c - trigger signal

A measurement process starts with the emission of the laser pulses. Each emitted laser pulse has a characteristic Gaussian shape with a certain temporal length T_{pulse}, energy content E and wavelength λ_{b} (see Fig. 2.3a). Laser pulses are usually emitted in bursts that last continuously over some period of time (see Fig. 2.3b). The emission frequency is constant and is known as the pulse repetition frequency (PRF). Different types of laser pulses can be emitted, where two examples are listed in table 2.1. The Long pulses contain more energy

than the Middle pulses, and due to the two times larger temporal length the aerosol particles at any distance are exposed to the laser light for a longer period. This results in higher carrier-to-noise ratio (CNR), which directly influences the maximum distance from which the radial velocity can be retrieved. The drawback of the Long pulses is that the retrieved radial velocity is characterized by the two times larger range resolution than in the case of the Middle pulses, which means that eddies smaller than the range resolution are filtered out. Typically the Long pulses are used to retrieve the radial velocity from distances of up to 8 km. On the other hand, the Middle pulses are suitable for the retrieval of radial velocity from distances of up to 4 km with the half range resolution of the Long pulse.

The emission process begins with the start of the trigger signal (see Fig. 2.3c). Each time the pulse generator receives a trigger, it sends an analog signal of the pulse shape and a copy of the trigger to the acousto-optic modulator (AOM). Based on these two input signals and the low-energy laser light from the CW laser, the AOM forms a low-energy laser pulse. In comparison to the original CW light, the laser pulse frequency is shifted to $f_\mathrm{b} = f_\mathrm{CW} + f_\mathrm{AOM}$, where f_CW is the frequency of the monochromatic low-energy laser light, and f_AOM is the frequency of the AOM. The AOM frequency is equal to about 60 MHz, and the shift in the frequency allows determining the retrieved radial velocity sign.

Once the low-energy laser pulse is formed, it is directed to the Erbium-doped fiber amplifiers (EDFA), which increase the energy content of the pulse. This forms the high-energy laser pulse. After the EDFA, the high-energy laser pulse passes through the optical circulator and telescope. The optical circulator has the role to separate directions of the outgoing laser pulses and the incoming backscattered light. By using the optical circulator, the transmitter of the laser pulses and the receiver of the backscattered light can both use the same optical path. The telescope is used to magnify the laser beam and to focus the beam at a certain distance. The magnification reduces the beam divergence in the far field, while the focusing is used to optimize the distribution of the laser beam power along the line of sight.

2.1.2.2 Acquisition of the backscattered light

As the laser pulse propagates through the atmosphere, along a direction given by the azimuth and elevation angles of the scanner head, it interacts with dispersed moving aerosol particles in the atmosphere. It is assumed that the particle velocities are equal to the wind velocity. Due to the optical Doppler effect, the particles perceive the incoming laser pulse light with slightly shifted frequency f_d (also called the Doppler frequency), where the difference in frequency corresponds to the velocity of the particles projected on the laser pulse propagation path, i.e. radial or line-of-sight (LOS) velocity. In the interaction between the particles and laser pulse, a small portion of the laser pulse light is reflected from the moving particles back to the lidar. Because of the movement of the particles, the backscattered light has the original frequency f_b shifted by twice the radial velocity divided by the wavelength of the emitted radiation. This shift in the frequency of the backscattered light is commonly known as the Doppler shift given as,

$$\delta f = 2\frac{v_\mathrm{r}}{\lambda_\mathrm{b}}, \tag{2.4}$$

where v_r is the radial velocity. The sign of the Doppler shift could be be positive or negative for the particles moving away from the lidar depending on the conventions used in a particular type of lidar. Due to the laser pulse's propagation through the atmosphere, the lidar continuously receives the backscattered light from different distances and thus the information about the radial velocity. Using the range gating technique, distinction between distances is achieved by using the backscattered light's time of arrival in relation to the start of the laser pulse.

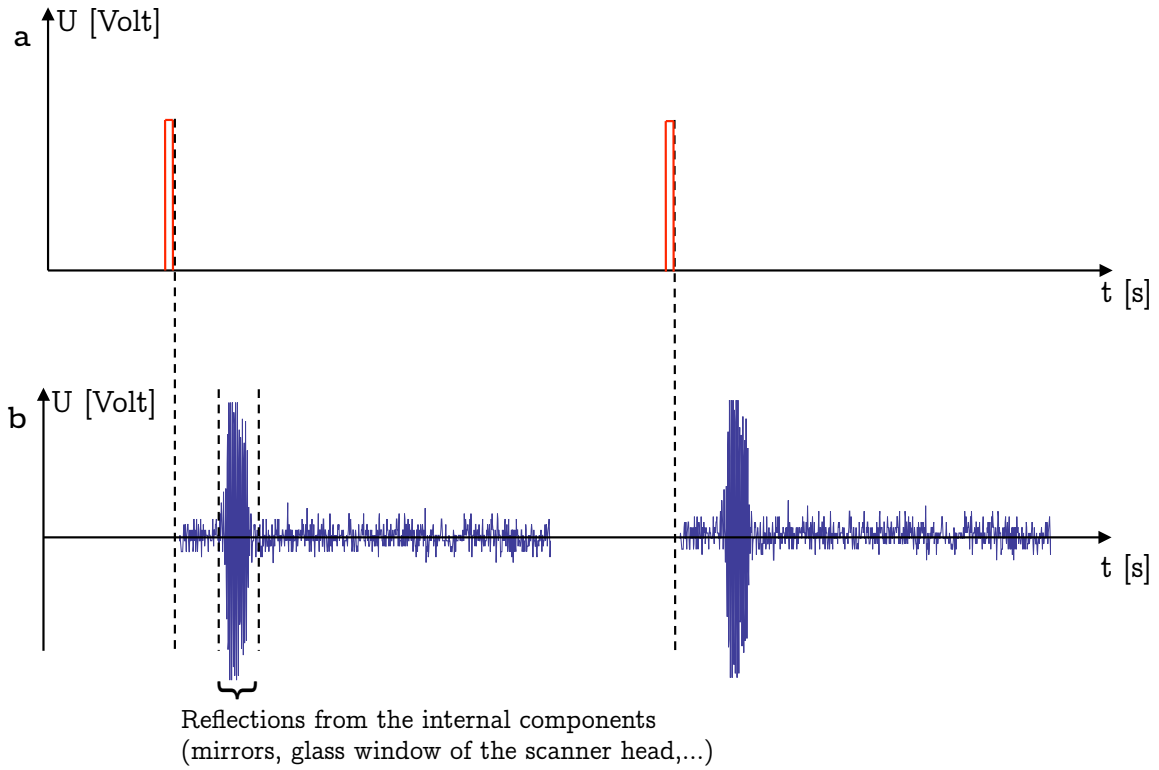

Figure 2.4: Emission: a - trigger signal, b - acquired analog signal

Once the backscattered light reaches the lidar, it follows the path of the outgoing laser pulses. It reflects on the mirrors, and it passes through the telescope after which it enters the optical circulator. Through the system of optical fibers, the backscattered light is directed towards the optical mixer, where it is optically mixed with the copy of the low-energy CW laser light, known as the local oscillator (LO) beam. The mixing of two light signals leads to the 'beat' phenomenon, in which the amplitude of the resulting light oscillates at the frequency difference between two light signals. This beating light signal is focused on the photodetector that transforms the light signal into an analog signal that follows the oscillation of the light intensity. The acquisition of the photodetector output occurs each time the acquisition board receives a trigger from the motion controller (see Fig. 2.4). The number of sample points of the digitized signal determines the maximum distance at which the radial velocity will be retrieved.

2.1.2.3 Analysis of the acquired backscattered light

The radial velocity at a distance d (note that in the rest of the report d_f is used instead) can be retrieved from the return of a single laser pulse by the estimation of the mean Doppler shift δf from M sample points of the corresponding digitized output of the photodetector. These M sample points define the observation time $T_\mathrm{FFT} = MT_s$, and they include the information regarding the backscattered light that originates from a range of distances $(d-\Delta d/2, d+\Delta d/2)$ centered at the distance d (see Fig. 2.5). If the finite discrete signal, given with M sample points, is transformed to the frequency domain, and spectrum of the transformed signal calculated, then by applying a frequency estimator on the spectrum, e.g. a Maximum Likelihood Estimator (MLE) [Valla, 2005], the frequency of the spectral peak can be estimated. Subtracting f_AOM from the estimated frequency yields the mean Doppler shift of the backscattered

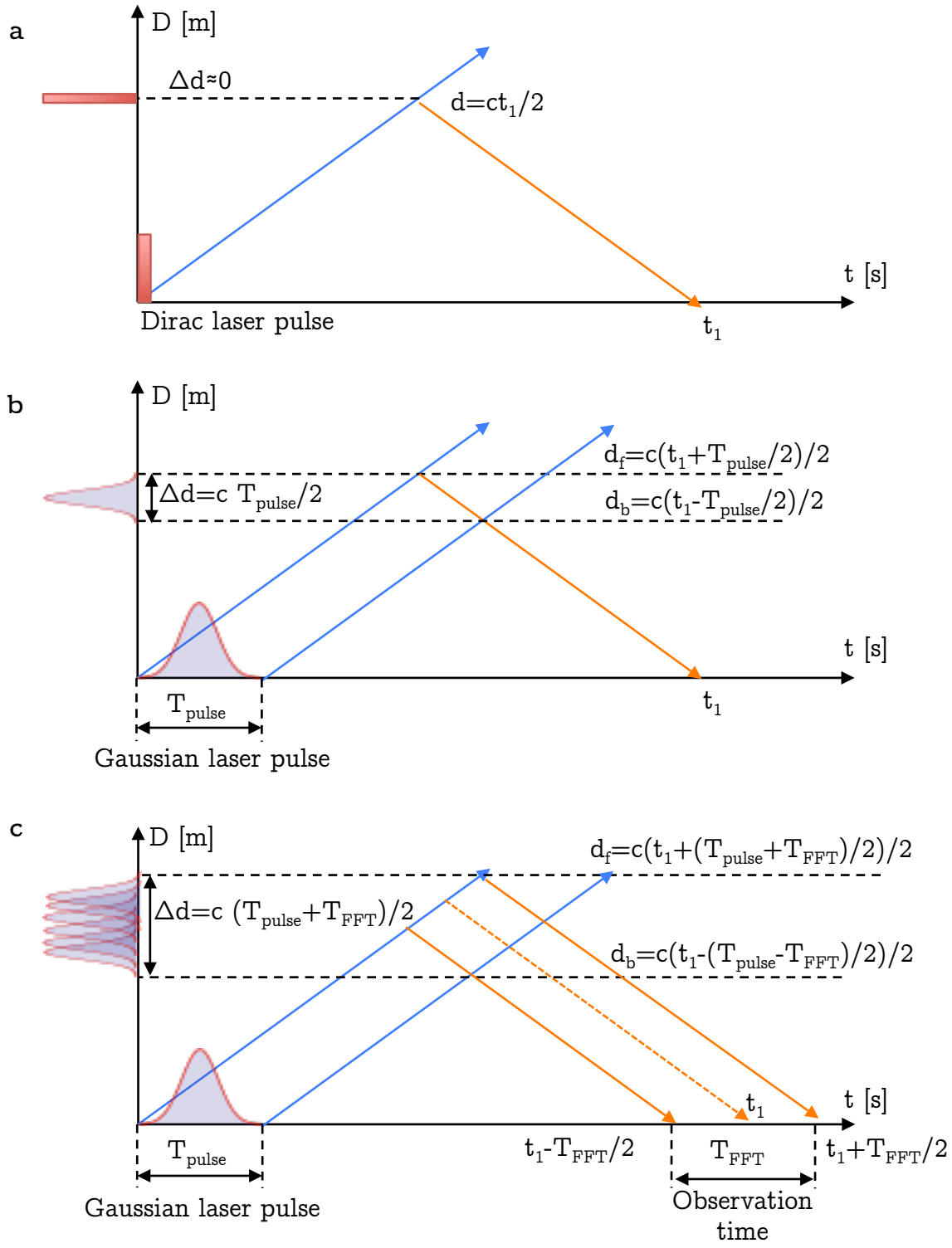

Figure 2.5: Retrieval of the radial velocity: a - one sample point of the dirac return, b - one sample point of the Gaussian return, c - M sample points of the Gaussian return

light from the range of distance centered at the distance d. Along with the Doppler shift, the MLE estimates the spectral broadening and CNR from the signal spectrum.

In order to express the signal of M sample points in terms of the spectrum, the observation

time T_{FFT} should be larger than the backscattered light correlation time, which can be approximated as the temporal length of the emitted laser pulse T_{pulse} [Frehlich et al., 1994]. The narrower the spectrum is, the more sample points are used to derive the spectrum. Obtaining more sample points results in improved velocity resolution, since each frequency bin in the spectrum will be defined on the smaller frequency range. The consequence of this is an increase in the length of the range gate, since more sample points mean bigger range of distance from which the backscattered light is acquired and analyzed. Due to the tradeoff between the velocity and range resolution, the observation time T_{FFT} is usually set to the temporal length of the emitted laser pulse T_{pulse}, which provides one independent retrieval of the radial velocity per observation time.

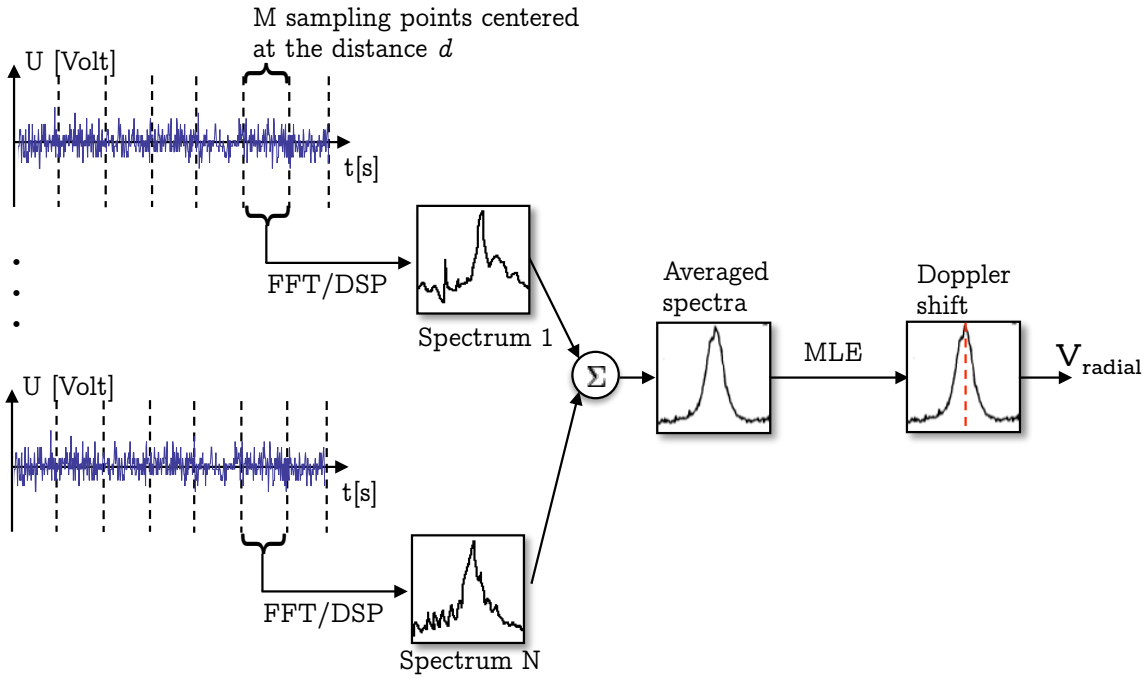

Figure 2.6: Accumulation Method

The retrieval of the radial velocity from a single laser pulse return encompasses the random error that originates from the uncorrelated noise [Frehlich, 2001], which leads to the incorrect estimate of the spectral peak. As an alternative, the estimation of the mean Doppler shift from N accumulations of the laser pulse returns leads to the suppression of the random error and improvement of the Doppler shift estimation accuracy [Davies and Collier, 1999]. In this method, the frequency estimator is applied on the averaged sum of N spectra (see Fig. 2.6). It has been shown in Frehlich et al. [1994] that the number of accumulations N of the order of 10 is useful for eliminating incorrect estimates of the radial velocity at low CNR.

2.2 Turbulence statistics relevant for wind energy

According to IEC [2005a] standards, a wind turbine should be designed for different classes of turbulence intensities. The turbulence intensity is defined according to Eq. (1.3). It is thus crucial to perform measurements of $\langle u'^2 \rangle$. Apart from I, it is also important to measure the mean wind speed profile, which is dependent on the velocity covariances $\langle u'w' \rangle$ and $\langle v'w' \rangle$ [Wyngaard, 2010]. This has a consequence for the mean wind gradient, since the larger the momentum fluxes the larger the mean wind gradient, and thereby potential for larger fatigue

loads on wind turbines. The diagonal components of $\mathbf{R}$, i.e., $\langle u'^2 \rangle$, $\langle v'^2 \rangle$ and $\langle w'^2 \rangle$ influence the loads significantly. Thus for wind energy purposes, it is very important to measure R_{ij}.

A current practice in the wind energy industry to perform load simulations is that a turbulent wind field is generated using either the Mann [1994] model or an empirical Kaimal et al. [1972] spectrum is combined with some coherence model [IEC, 2005a]. As discussed in chapter 1, the need to measure ε and $\mathscr{L}$ is then clearly evident. These parameters are normally obtained by fitting the Mann [1994] model to the measurements of $F_{ij}(k_1)$, which could be obtained using lidars. $\mathscr{L}$ and coh_{ij} are important for estimating the loads and wake meandering [Larsen et al., 2008]. The influence of atmospheric stability on the wind speed profile and on wind turbine loads is becoming increasingly evident [Sathe et al., 2011a, 2013]. For this reason, measurement of $\langle w'\theta' \rangle$, the vertical heat flux is quite important for wind energy, as it can be used to calculate atmospheric stability parameters. According to Lenschow et al. [1994], ℓ_{ij} is useful in estimating the averaging time required to keep the random errors below a certain threshold for a particular turbulence statistic, and hence is a desirable measurement quantity for wind energy purposes.

Recently, lidars are being considered for wind turbine control. The concept is such that the lidar is either placed on a nacelle of a wind turbine [Schlipf et al., 2013], or mounted inside a spinner [Mikkelsen et al., 2013, Simley et al., 2013] in order to detect the incoming wind field and carry out a feed-forward control to reduce the structural loads on a wind turbine. The degree to which such a concept can be successfully applied depends on how well the lidars are able to detect the incoming turbulent structures. From Sathe et al. [2013] we understand that different components of a wind turbine are affected by different scales of turbulent structures. It is thus important to be able to detect the range of turbulence scales, up to the order of or less than the probe volume length.

Chapter 3

Measurement Configurations

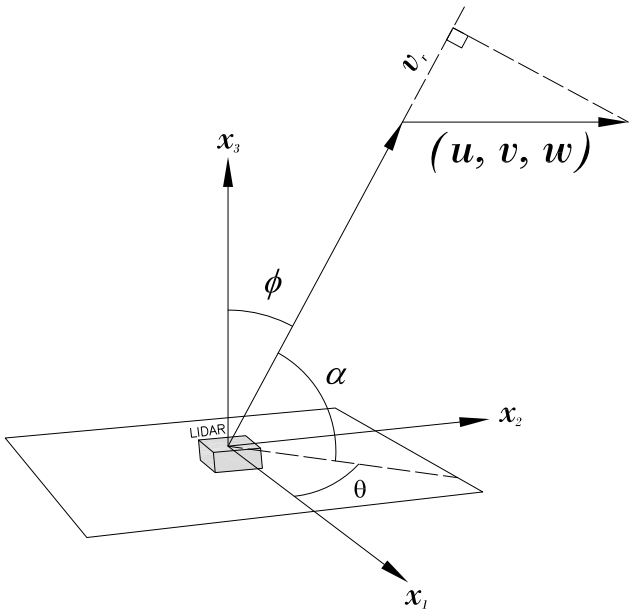

Figure 3.1: Coordinate system of a lidar

In order to understand different measurement configurations better, we first define a coordinate system in which a lidar performs measurements. It is to be noted that the coordinate system defined in this section is not a universally accepted system, but simply a reference based on which different measurement configurations could be understood. We choose a base coordinate system in accordance with that defined in chapter 1, where the positive x_1 axis is pointing East, the positive x_2 axis is pointing North and the positive x_3 axis is vertical. As shown in Fig. 3.1, at a given instant of time if we assume that a lidar measures at a point, and that the lidar beam is inclined at a certain zenith angle ϕ (in some literature the complement of ϕ is used, which is called as the elevation angle $\alpha = 90° - \phi$) from the vertical axis, and makes a positive azimuth angle θ in a counterclockwise direction with respect to the x_1 axis in the horizontal plane, then the radial velocity (also called as the line-of-sight velocity) can be mathematically written as,

$$v_{\mathrm{r}}(\phi, \theta, d_{\mathrm{f}}) = \boldsymbol{n}(\phi, \theta) \cdot \mathbf{v}(\boldsymbol{n}(\phi, \theta) d_{\mathrm{f}}), \tag{3.1}$$

where v_{r} is the radial velocity measured at a point, $\boldsymbol{n} = (\cos\theta \sin\phi, \sin\theta \sin\phi, \cos\phi)$ is the unit directional vector for a given ϕ and θ, d_{f} is the distance at which the measurement is

obtained, and $\mathbf{v} = (u, v, w)$ is the wind vector. As also mentioned in chapter 1, in order to avoid the complexity of equations by the introduction of the rotation matrices, in the rest of the report it is assumed that the streamline coordinate system is aligned with the base coordinate system, i.e. the mean wind direction is aligned with the x_1 axis.

For simplicity in the rest of the report, it is assumed that the streamline coordinate system is aligned with the coordinate system of the lidar such that u is along the positive x_1 axis . In Eq. (3.1), we have implicitly assumed that v_r is positive for the wind going away from the lidar axis, the coordinate system is right-handed, and u is aligned with the x_1 axis in a horizontal plane, i.e. from west to east. In reality, a lidar never receives backscatter from exactly a point, but from all over the physical space. Fortunately the transverse dimensions of a lidar beam are much smaller than the longitudinal dimensional, and for all practical purposes we can consider that the backscatter is received only along the lidar beam axis. Mathematically the radial velocity can be represented as the convolved signal,

$$\tilde{v}_\mathrm{r}(\phi, \theta, d_\mathrm{f}) = \int_{-\infty}^{\infty} \varphi(s)\ \boldsymbol{n}(\phi, \theta) \cdot \mathbf{v}(\boldsymbol{n}(\phi, \theta)(d_\mathrm{f} + s))\ ds, \tag{3.2}$$

where $\tilde{v}_\mathrm{r}$ is the weighted average radial velocity, $\varphi(s)$ is any weighting function integrating to one that depends on the type of lidar, i.e. a continuous wave (c-w) lidar or a pulsed lidar, and the integration variable s is the distance along the beam from the measurement point of interest. In the following sections, where possible, only the point representation of the radial velocity, i.e. v_r will be used for simplicity.

3.1 Commercial configurations

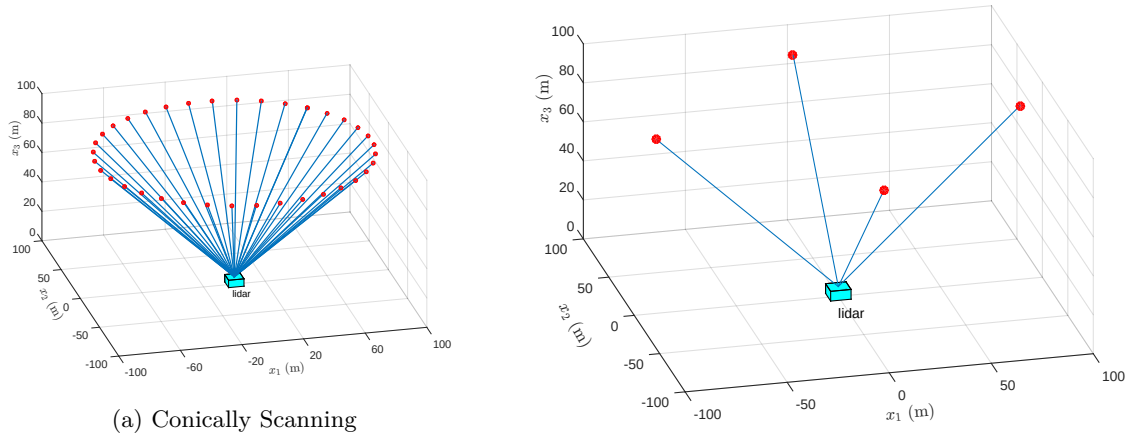

(a) Conically Scanning

(b) Doppler Beam Swinging

Figure 3.2: The two most commonly used measurement configurations in commercial lidars

Figure 3.2 shows the two most commonly used scanning configurations by commercial lidars. The conically scanning configuration performs a conical scan, where several measurements of the radial velocity (v_r) are performed over the base of a cone. The Doppler Beam Swinging (DBS) scanning configuration also performs a conical scan, but with v_r measurements of only a few beams on the base of the cone. Here we use four beams as an example, but it could also be five beams. Both configurations use the so-called velocity azimuth display (VAD) method of data processing to deduce the wind vector components u, v and w. In principle to deduce the wind vector components we only need three v_r measurements at different θ and ϕ. However for the conically scanning configuration (Fig. 3.2a), we have several

measurements of v_r, which results in an over-determined system. Least-squares analysis is thus used to deduce the wind vector components as,

$$\begin{aligned} u &= \frac{1}{\pi \sin\phi} \int_0^{2\pi} v_\mathrm{r}\ \cos\theta\ d\theta, \\ v &= \frac{1}{\pi \sin\phi} \int_0^{2\pi} v_\mathrm{r}\ \sin\theta\ d\theta \\ w &= \frac{1}{2\pi \cos\phi} \int_0^{2\pi} v_\mathrm{r}\ d\theta, \end{aligned} \tag{3.3}$$

where the argument of v_r is dropped for simplicity. For the DBS scanning configuration (Fig. 3.2b), let us denote the beams in the positive and negative x_1 direction as east (E) and west (W) respectively. Similarly the beams in the positive and negative x_2 direction are defined as north (N) and south (S) respectively. The wind vector components are then deduced as,

$$\begin{aligned} u &= \frac{v_{\mathrm{r}E} - v_{\mathrm{r}W}}{2\sin\phi}, \\ v &= \frac{v_{\mathrm{r}N} - v_{\mathrm{r}S}}{2\sin\phi}, \\ w &= \frac{v_{\mathrm{r}E} + v_{\mathrm{r}N} + v_{\mathrm{r}W} + v_{\mathrm{r}S}}{4\cos\phi}. \end{aligned} \tag{3.4}$$

Equations (3.3) or (3.4) denote the VAD method of data processing that involves estimating the wind vector components by combining v_r measurements from several beams for each scan. For a given averaging period the deduced wind vector components from each scan produce a time series, which are used to estimate the turbulence statistics.

3.1.1 Estimating components of R using VAD technique of processing lidar data

In wind energy, we are usually interested in statistics defined by Eqs. (1.7) or (1.9)(see also section 2.2). However, different lidar data processing techniques produce different estimates of turbulence statistics than those given by Eqs. (1.7) or (1.9). Commercial lidars usually use the VAD/DBS technique of data processing, where the v_r measurements at different azimuth angles are combined to deduce u, v and w. The deduced time series of the wind vector components is further processed to estimate turbulence statistics within a given averaging period. As a result, we do not obtain the standard turbulence statistics defined by Eq. (1.7), but some filtered (on small scales) statistic and contaminated by cross-correlations between different wind vector components. Mathematically, it is given as,

$$R_{mn_\mathrm{lidar}} = \int \Phi_{ij}(\boldsymbol{k}) X_i^m(\boldsymbol{k}) X_j^{*n}(\boldsymbol{k})\ d\boldsymbol{k}, \tag{3.5}$$

where the subscript lidar denotes the estimated statistic using the lidar measurements, $\boldsymbol{X}(\boldsymbol{k})$ is the filter function in the Fourier domain, which depends on the type of lidar (CW or pulsed) and the Reynolds stress tensor component of interest.

The detailed derivation of Eq. (3.5) can be found in Sathe et al. [2011b], but even without going through the mathematical details, if we simply compare Eqs. (3.5) and (1.7), it is clear that they are very different from each other. The function $\boldsymbol{X}(\boldsymbol{k})$ acts as a filter to smaller scales of turbulence, whereas its combination with the spectral velocity tensor $\boldsymbol{\Phi}(\boldsymbol{k})$(by applying the Einstein summation notation) denotes the contamination due to the cross-correlation of different wind vector components. These two effects tend to counter each other, and therefore sometimes turbulence estimates from the VAD method can have comparable accuracy with

those estimated from the reference instruments. In colloquial language it could be understood as 'getting it right for the wrong reasons'. Hence one should be careful in using the VAD method to estimate turbulence statistics, since the accuracy of turbulence estimates may not be reproducible. In contrast to the VAD method, cup and sonic anemometers measure a value of $\mathbf{R}$ that is quite close to that described by Eq. (1.7). Volume averaging is very small for tower instruments, as they for all practical purposes provide point measurements, so there is no filtering function that affects small scales of turbulence. In addition, since tower instruments take measurements from a small volume of air, there is negligible variance contamination. However, tower measurements of turbulence can also be affected by sources of error, including tower icing, instrument noise, and for cup anemometers, cup overspeeding in gusty wind environments.

3.1.2 Estimating ε using conically scanning lidar

As also discussed in chapter 1 the importance of estimating ε can be understood when it comes to modelling, and especially for deriving the inertial subrange of spectra. In order to use this method the scanning speed of the lidar must be much larger than the advection speed of turbulence. An expression can then be derived for the radial velocity structure function for different separation distances $d_\mathrm{f}\delta$, on the base of the scanning cone, where $\delta = 2\sin^{-1}(\sin\phi\sin\theta)$ is the angle subtended by the two lidar beams in a conical scan. Banakh et al. [1996] were the first to formulate mathematical expressions, but Kristensen et al. [2012] re-derived their original expressions, where an additional $R(0)$ term was added. The contribution due to random instrumental noise was however neglected that was considered in Banakh et al. [1996]. For modern lidar systems, the instrumental noise can be neglected [Mann et al., 2009].

Two approaches were chosen in the derivation by Kristensen et al. [2012]: the time-domain autocorrelation approach, and the Fourier-domain wave-number approach. The Fourier-domain approach is derived for a CW lidar (assuming a Lorentzian function), whereas the time domain approach provides expressions as a function of $\varphi(s)$. By using appropriate expressions of $\varphi(s)$, the time-domain expressions can be applied to a CW or a pulsed lidar. The equations using both approaches are as follows. In the time domain,

$$\begin{aligned}\tilde{D}(\delta) &= 2(1-\cos\delta)R(0) + \frac{9}{55}\Gamma\left(\frac{1}{3}\right)C(\varepsilon d_\mathrm{f})^{2/3}\int_{-\infty}^{\infty}\int_{-\infty}^{\infty}\varphi(s_1')\varphi(s_2') \\ &\cdot\left(3\left(\left((s_2'-s_1')^2 + 4s_1's_2'\sin^2(\delta/2)\right)^{1/3}\cos\delta - |s_2'-s_1'|^{2/3}\right)\right. \\ &\left. + \frac{s_1's_2'\sin^2\delta}{\left((s_2'-s_1')^2 + 4s_1's_2'\sin^2(\delta/2)\right)^{2/3}}\right) ds_1'ds_2', \end{aligned} \tag{3.6}$$

where $\tilde{D}(\delta)$ is the filtered radial velocity structure function for a separation distance $d_\mathrm{f}\delta$, on the base of the cone, $R(0) = \langle u'^2\rangle = \langle v'^2\rangle = \langle w'^2\rangle$ for isotropic turbulence, and $s_1' = s_1/d_\mathrm{f}$,

$s_2' = s_2/d_\mathrm{f}$ are non-dimensional variables. In the Fourier domain, for a C-W lidar,

$$\begin{aligned}\tilde{D}(\delta) \;&= 2(1-\cos\delta)R(0) + C(\varepsilon d_\mathrm{f})^{2/3}\frac{3}{55}\Gamma\Big(\frac{1}{3}\Big)\\
&\Bigg(\frac{3}{\sqrt[3]{2}}(1+7\cos\delta)\sin^{2/3}(\delta/2) - 18\Big(\frac{d_\mathrm{f}}{l}\Big)^{-2/3}\\
&+ \frac{1}{\pi}\Big(\frac{2d_\mathrm{f}}{l}\Big)^{-2/3}\int_0^{\pi/2}\frac{\Gamma(1/2)\Gamma(1/3)}{\Gamma(5/6)}(7\cos\delta - 4\cos(2\xi))\\
&\cdot\;\Big(2\cos\Big(\frac{2}{3}\tan^{-1}\Big(\frac{4d_\mathrm{f}\sin(\delta/2)\sin\xi}{l(|\cos(\xi+\delta/2)|+|\cos(\xi-\delta/2)|)}\Big)\Big)\\
&\cdot\;\Big((|\cos(\xi+\delta/2)|+|\cos(\xi-\delta/2)|)^2 + 16\Big(\frac{d_\mathrm{f}}{l}\Big)^2\sin^2(\delta/2)\sin^2\xi\Big)^{1/3}\\
&- \big(4\frac{d_\mathrm{f}}{l}\sin(\delta/2)\sin\xi\big)^{2/3}\Big)\;d\xi\Bigg),\end{aligned} \tag{3.7}$$

where $\Gamma(n) = \int_0^\infty x^{n-1}\exp(-x)\,dx$ is the gamma function. The key to using this method is to appropriately select $d_\mathrm{f}\delta \ll \mathscr{L}$, so that turbulence is measured in the inertial subrange, and is locally isotropic. $\tilde{D}(\delta)$ can be measured using a lidar; then, by knowing $R(0)$, we can estimate ε. Banakh et al. [1996] did not include the $R(0)$ term in their equation, perhaps because at $\delta \ll \pi/2$, and $d_\mathrm{f} \gg \mathscr{L}$, this term is negligible. The advantage of using Eq. (3.7) is that we need to solve only a single integral numerically, whereas in Eq. (3.6) we need to solve a double integral numerically, and that may increase the numerical error. The estimation of $R(0)$ can be quite challenging, since it also contains information about the large-scale turbulence. Kristensen et al. [2012] used empirical models for convective turbulence [Kristensen et al., 1989] and estimated that $R(0) = 1.74\,\varepsilon^{2/3}(d_\mathrm{f}\cos\phi)^{2/3}$. Alternatively, one may use the von Kármán [1948] energy spectrum and derive expressions for $R(0)$.

3.2 Research configurations

3.2.1 Staring mode

This is the simplest of all the measurement configurations, where a lidar beam constantly points only at one height with a given θ and ϕ. Fig. 3.1 illustrates this measurement configuration. Because v_r is a function of three wind vector components, a single beam cannot be used to retrieve u, v and w. Despite its simplicity, one could use this configuration to understand the spatial (probe volume) averaging effects in the estimated second-order statistics, and to estimate a small scale turbulence parameter, namely the turbulent kinetic energy dissipation rate ε [Banakh and Smalikho, 1997b, Frehlich et al., 1998, Smalikho, 1995]. Two approaches can be used in estimating ε,

- Doppler spectrum width
- Radial velocity structure function

3.2.1.1 Spatial averaging effects on the estimated turbulence statistics

From Eq. (3.2), we understand that in reality the radial velocity measurements from any lidar (CW or pulsed) is a convolution of the wind vector by the weighting function within the probe

volume. Neglecting the arguments in the brackets for simplicity, Eq. (3.2) can equivalently be written as,

$$\tilde{v}_\mathrm{r} = (\boldsymbol{n} \cdot \mathbf{v}) \otimes \varphi, \tag{3.8}$$

where $\otimes$ denotes convolution. Then by using convolution theorem, taking the Fourier transform of Eq. (3.8),

$$\widehat{\tilde{v}}_\mathrm{r} = (\boldsymbol{n} \cdot \widehat{\mathbf{v}}) \times \widehat{\varphi}, \tag{3.9}$$

where $\widehat{\varphi}$ denotes Fourier transform. From the definition of spectrum, we can then write,

$$\tilde{F}(k_1) = (\boldsymbol{n} \cdot F_\mathbf{v}(k_1)) \times |\widehat{\varphi}|^2, \tag{3.10}$$

where $\tilde{F}(k_1)$ is the filtered radial velocity spectrum, $||$ denotes absolute value, and $F_\mathbf{v}(k_1)$ denotes the spectra of the three wind vector components. Depending on the form of $\varphi(s)$, the spatial averaging effects on the estimated radial velocity spectrum can be understood from Eq. (3.10).

3.2.1.2 Estimating ε using Doppler spectrum width

This method requires access to the raw Doppler spectra data, which is used to estimate v_r. Only the mathematical formulation for a CW lidar is provided, since the mathematics for a pulsed lidar is extremely complicated, and interested readers can refer to Smalikho et al. [2005]. For a CW lidar, if we define $l = \lambda_\mathrm{b} d_\mathrm{f}^2 / \pi r_\mathrm{b}^2$ as the Rayleigh length corresponding to the filtering of the small scale turbulence, where λ_b is the wavelength of the emitted radiation, r_b is the beam radius, and d_f is the distance at which the measurements are obtained, then

$$\langle \sigma_\mathrm{s}^2 \rangle = 1.22 C \varepsilon^{2/3} l^{2/3}, \tag{3.11}$$

where $\langle \sigma_\mathrm{s}^2 \rangle$ is the second central moment of the Doppler spectrum (or its width), and $C \approx 1.5$ is the universal Kolmogorov constant. For detailed derivation of Eq. (3.11) the readers are referred to Smalikho [1995].

$\langle \sigma_\mathrm{s}^2 \rangle$ can be measured and l is known, so ε can be estimated. The limitation of this method is that Eq. (3.11) can only be used when $l \ll \mathscr{L}$, where $\mathscr{L}$ is the outer scale of turbulence. Moreover, the effect of mean radial velocity gradient within the probe volume has not been taken into account. Equation (3.11) states that if there is no turbulence, then the Doppler spectral width should be zero. However, if there is a mean change of v_r with s (within the probe volume) then there is an additional term proportional to l^2. If the lidar is C-W and the shear is linear, then the coefficient of l^2 is infinite [Mann et al., 2010] and we cannot use this method.

3.2.1.3 Estimating ε using the radial velocity structure function

The main challenge in using this method lies in appropriately selecting an inertial subrange from the lidar data, where an assumption of isotropy of the turbulence can reasonably be assumed to be true [Pope, 2000]. A consequence of this assumption is that for a point measurement, the turbulence spectrum (or equivalently the structure function) becomes proportional to $\varepsilon^{2/3}$ only. As an example, the structure function of the u component in the inertial subrange can be expressed as [Pope, 2000]:

$$D_{11}(r_1) = C_2 \varepsilon^{2/3} r_1^{2/3}, \tag{3.12}$$

where $D_{11}(r_1)$ is the one-dimensional structure function of the longitudinal wind vector component u, and $C_2 \approx 2$ is the Kolmogorov constant related to $D_{11}(r_1)$. For a lidar, owing

to presence of a large measurement volume we need to consider the weighting function $\varphi(s)$ within the measurement volume, and as a result the equation of the structure function becomes much more complicated. Moreover $\varphi(s)$ is different for different types of lidars, i.e. a CW or a pulsed lidar.

3.2.1.3.1 CW lidar

The weighting function $\varphi(s)$ for a CW lidar can reasonably be assumed to be Lorentzian [Sonnenschein and Horrigan, 1971], which results in filtering of the small scale turbulence. For a staring lidar one could only estimate the radial velocity structure function, which mathematically can be expressed as [Kristensen et al., 2011, Smalikho, 1995],

$$\tilde{D}(r_1) = C\varepsilon^{2/3} l^{2/3} \frac{\Gamma(1/3)}{5\sqrt{\pi}\Gamma(5/6)} \int_0^{2\pi} \Big(1 - \frac{8}{11}\cos^2\xi\Big) \Psi(r_1, \beta, \xi)\, \mathrm{d}\xi, \tag{3.13}$$

where $\tilde{D}(r_1)$ is the filtered radial velocity structure function measured by the lidar, $r_1 = \langle u \rangle t$ is the separation distance along the x_1 axis, $\beta = \arcsin(\sqrt{(d_\mathrm{f}\cos\phi)^2 + (d_\mathrm{f}\sin\phi\sin\Theta)^2}/d_\mathrm{f})$ is the angle between the lidar beam and the mean wind $\langle u \rangle$, and

$$\begin{aligned} \Psi(r_1, \beta, \xi) = {} & \frac{3}{2}\Gamma\Big(\frac{1}{3}\Big)\Bigg(\Big(\cos^2\xi + \big(\frac{r_1}{l}\big)^2 \cos^2(\xi+\beta)\Big)^{1/3} \\ & \cdot \cos\Big(\frac{2}{3}\tan^{-1}\Big(\frac{r_1}{l}\Big|\frac{\cos(\xi+\beta)}{\cos\xi}\Big|\Big)\Big) - |\cos\xi|^{2/3}\Bigg). \end{aligned} \tag{3.14}$$

r_1 is computed using the Taylor hypothesis [Taylor, 1938], where turbulence is assumed to be advected by the mean wind $\langle u \rangle$ in time t.

For the measured and known parameters $\tilde{D}(r_1)$, β, r_1, l and C, the unknown ε can be estimated, where the one-dimensional integral in Eq. (3.13) can be solved numerically. It is to be noted that due to the dependence of $\tilde{D}(r_1)$ on β, it is essential to estimate Θ, which could be done by alternating between staring and VAD scanning, or by using estimated Θ from the met-mast anemometry. The advantage of alternating the scans is then obvious, since it obviates the need for a met-mast. Comparing Eqs. (3.12) and (3.13), it is clear that estimating ε using a lidar is quite complicated, but nevertheless possible.

3.2.1.3.2 Pulsed lidar

For a pulsed lidar, different shapes of weighting functions have been suggested, e.g. triangle and Gaussian [Frehlich, 1997, Lindelöw-Marsden, 2009]. Here we present the mathematical formulation for a Gaussian pulse. We define w_p to be the pulse width (standard deviation of the Gaussian pulse), and $L_p = c\tau$ to be the range gate length of a pulsed lidar, where c is the speed of light and τ is the pulse duration. If we introduce a length scale $l_\mathrm{p} = \sqrt{L_\mathrm{p}^2/12 + w_\mathrm{p}^2}$ then the same Eq. (3.13) can be used by replacing l with l_p, where the $\Psi(r_1, \beta, \xi)$ function is now given as

$$\Psi(r_1, \beta, \xi) = \frac{3}{2}\Gamma\Big(\frac{2}{3}\Big)|\cos\xi|^{2/3}\Bigg({}_1F_1\Big(-\frac{1}{3}; \frac{1}{2}; -\frac{r_1^2\cos^2(\xi+\beta)}{4l_\mathrm{p}^2\cos^2\xi}\Big) - 1\Bigg), \tag{3.15}$$

where ${}_1F_1(a; b; x)$ is the Kummer confluent hypergeometric function [Abramowitz and Stegun, 1965]. It is to be noted that using Eqs. (3.13) and (3.15), for some combinations of β and r_1/l (or r_1/l_p), $\tilde{D}(r_1)$ becomes negative, but Kristensen et al. [2011] provide the range within which Eqs. (3.13) and (3.15) are valid. An advantage of using a pulsed lidar is also that we do not need to apply Taylor's hypothesis in order to compute the separation distance. Thus,

instead of using r_1 in Eq. (3.15) we can use the separation distance r (provided that $r \ll \mathscr{L}$) along the lidar beam, since a pulsed lidar measures at different range gates simultaneously, and hence measure $\tilde{D}(r)$ along the lidar beam axis [Frehlich, 1997].

3.2.2 Six-Beam Scanning

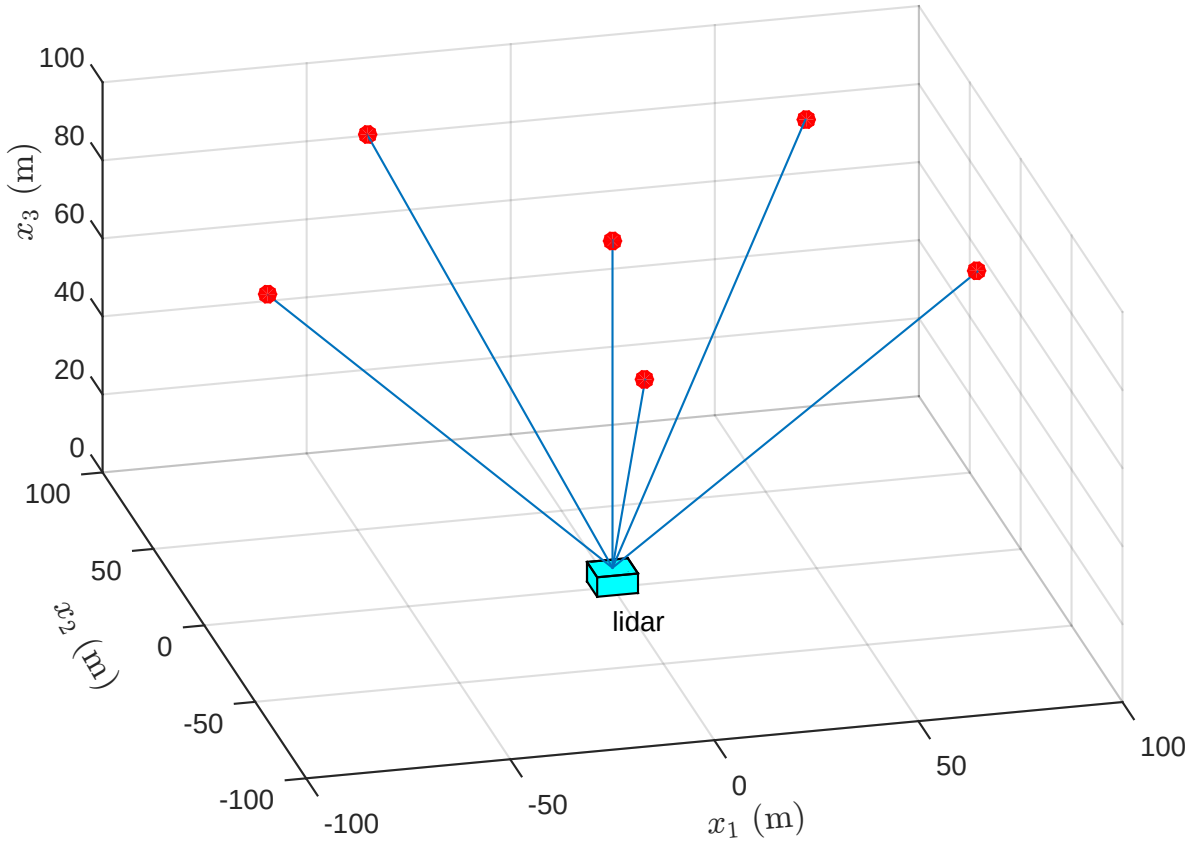

Figure 3.3: Six-Beam Scanning

As seen in section 3.2.1, using only one beam precludes estimation of any turbulence statistics from the lidar data, whereas section 3.1.1 demonstrates that the VAD method of data processing from the scanning lidars results in significant systematic errors. An alternative to the VAD method is the six-beam scanning technique as shown in Fig. 3.3, where two different ϕ are used such that five beams at equally spaced θ subtend an angle ϕ, and the sixth beam is vertical ($\phi = 0$). This is a very recent configuration which has been used to estimate $\mathbf{R}$ [Sathe et al., 2015].

3.2.2.1 Estimating components of R using six-beam scanning

Instead of using the VAD method to deduce the wind vector components for each scan from the lidar data, in this method variances of radial velocities $\langle v_r'^2 \rangle$ are used. Mathematically it can be represented as,

$$\begin{aligned}\langle v_r'^2 \rangle = {} & \langle u'^2 \rangle \sin^2\phi \cos^2\theta + \langle v'^2 \rangle \sin^2\phi \sin^2\theta + \langle w'^2 \rangle \cos^2\phi \\ & + 2\langle u'v' \rangle \sin^2\phi \sin\theta \cos\theta + 2\langle u'w' \rangle \sin\phi \cos\phi \cos\theta + 2\langle v'w' \rangle \sin\phi \cos\phi \sin\theta,\end{aligned} \tag{3.16}$$

where $\langle v_r'^2 \rangle$ is the radial velocity variance. From Eq. (3.16) we can see that for a given θ and ϕ, if we have six measurements of $\langle v_r'^2 \rangle$ then there are six unknowns to be determined, which in a matrix form can be written as,

$$\mathbf{M} \underbrace{\begin{bmatrix} \langle u'^2 \rangle \\ \langle v'^2 \rangle \\ \langle w'^2 \rangle \\ \langle u'v' \rangle \\ \langle u'w' \rangle \\ \langle v'w' \rangle \end{bmatrix}}_{\mathbf{\Sigma}} = \underbrace{\begin{bmatrix} \langle v_{r_1}'^2 \rangle \\ \langle v_{r_2}'^2 \rangle \\ \langle v_{r_3}'^2 \rangle \\ \langle v_{r_4}'^2 \rangle \\ \langle v_{r_5}'^2 \rangle \\ \langle v_{r_6}'^2 \rangle \end{bmatrix}}_{\mathbf{S}}, \tag{3.17}$$

where $\mathbf{\Sigma}$ is a vector of the components of $\mathbf{R}$ (because $\mathbf{R}$ is symmetric, we only need six components), $\mathbf{M}$ is a 6×6 matrix of the coefficients of $\mathbf{\Sigma}$ that consist of different combinations of θ and ϕ (see Eq. 3.16), and $\mathbf{S}$ is a vector of measurements of $\langle v_r'^2 \rangle$ at different θ and ϕ (where the suffices denote measurements from beam 1 to 6). In principle we can then estimate $\mathbf{\Sigma}$ using the relation $\mathbf{\Sigma} = \mathbf{M}^{-1}\mathbf{S}$, where $^{-1}$ denotes matrix inverse. It is interesting to know beforehand, whether the measurements from the six beams on only one zenith angle are adequate, i.e. whether we can have six θs and only one ϕ.

From fundamental algebra we understand that Eq. (3.17) will have a finite solution if and only if $\det \mathbf{M} \neq 0$, where det denotes the determinant of a matrix. In other words $\mathbf{M}$ should not be a degenerate matrix. From the properties of determinants we know that if any two rows (or columns) of a matrix are identical then its determinant is zero. Also, if the elements of any row (or column) are increased (or decreased) by equal multiples of the corresponding elements of any other row (or column), the value of determinant is unchanged. If we use only one ϕ at different θ, and add the first two columns of $\mathbf{M}$, we get the first and the third columns of $\mathbf{M}$ to be multiples of each other, which according to the property of determinants implies $\det \mathbf{M} = 0$. Thus $\mathbf{M}$ becomes degenerate if we use only one ϕ, and thus need $\langle v_r'^2 \rangle$ measurements from more than one ϕ.

Table 3.1: Optimum six-beam configuration

Beam no.	1	2	3	4	5	6
θ (°)	0	72	144	216	288	288
ϕ (°)	45	45	45	45	45	0

The challenge then is to obtain an optimum combination of θ and ϕ. Measured $\mathbf{S}$ is stochastic, and the random error of $\mathbf{\Sigma}$ will depend on the particular choice of the θs and ϕs. The objective function is chosen such that the sum of the random errors of the components of $\mathbf{\Sigma}$ are minimized and results in the optimum configuration as given in table 3.1.

It is to be noted that using this method, one can only minimize the problem of cross-contamination, but the problem of filtering of small-scale turbulence still remains. Nevertheless it is a much more reliable method than the VAD technique in estimating turbulence statistics [Sathe et al., 2015].

3.2.3 Range Height Indicator Scanning

Fig. 3.4 shows the Range Height Indicator (RHI) scanning technique, where the scanning is performed in a vertical $(x_1 - x_3)$ plane at different ϕ, but at a constant θ. Measurements from different beams at the same height can be used to deduce the wind vector components, but it usually requires assumption of horizontal homogeneity over large distances and scanning in

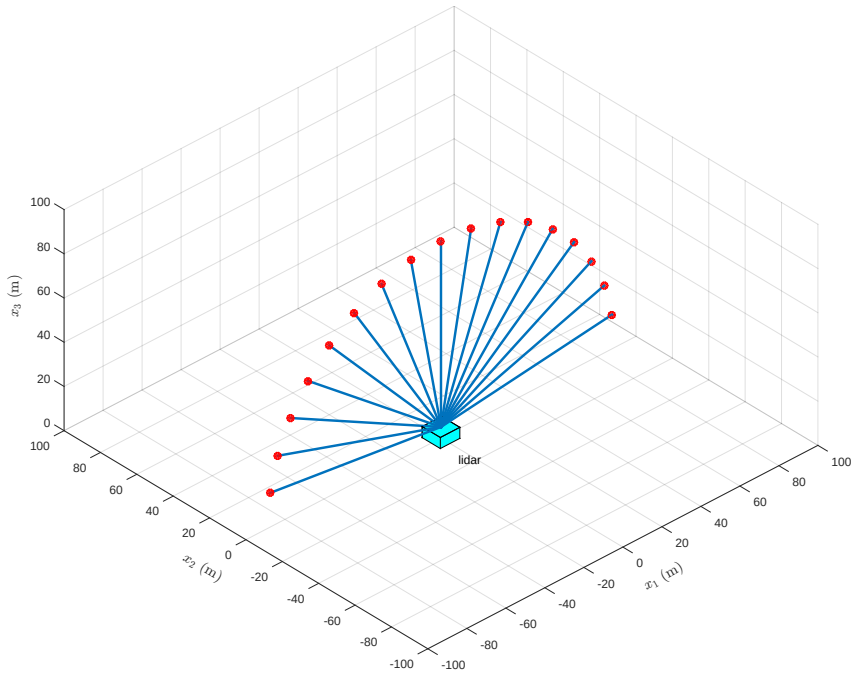

Figure 3.4: Range Height Indicator Scanning

at least two vertical planes preferably 90° apart. It is however to be noted that if the wind vector components are deduced for each scan and then the statistics are estimated over some averaging interval, it is equivalent to the VAD method of data processing, and the resulting turbulence statistics will be subjected to both, the filtering and the cross-contamination effects as seen for the commercial lidars. Instead using the variances of radial velocities $\langle v_r'^{\,2} \rangle$ is a much better way of estimating components of $\mathbf{R}$ [Gal-Chen et al., 1992].

3.2.3.1 Estimating components of R using the RHI scanning technique

As proposed by Gal-Chen et al. [1992], components of $\mathbf{R}$ can be estimated from the RHI scanning data if the scanning is performed in the mean wind direction and perpendicular to the mean wind direction. Mathematically it can be represented as,

$$\langle v_r'^{\,2} \rangle = \langle u'^2 \rangle \sin^2\phi + \langle w'^2 \rangle \cos^2\phi \pm \langle u'w' \rangle \sin(2\phi), \tag{3.18}$$

for the lidar beam aligned in the mean wind direction. The $\pm$ sign for $\langle u'w' \rangle$ indicates whether the wind is blowing away from or towards the lidar beam. Similarly, for the cross-wind direction we have

$$\langle v_r'^{\,2} \rangle = \langle v'^2 \rangle \sin^2\phi + \langle w'^2 \rangle \cos^2\phi \pm \langle v'w' \rangle \sin(2\phi), \tag{3.19}$$

where the $\pm$ sign indicates positive or negative cross wind beam direction. Equations (3.18) and (3.19) are then solved using the least squares analysis to obtain components of $\mathbf{R}$ (except $\langle u'v' \rangle$).

It is to be noted that using this method, one can only minimize the problem of cross-contamination, but the problem of filtering of small-scale turbulence still remains. Also it is logistically quite challenging to orient the scanning in the along-wind and cross-wind directions. The lidar would need information of the mean wind direction beforehand in order to orient the scanning pattern in the respective directions. However this information could be obtained by conducting periodic VAD scans.

3.2.4 Arc-scanning

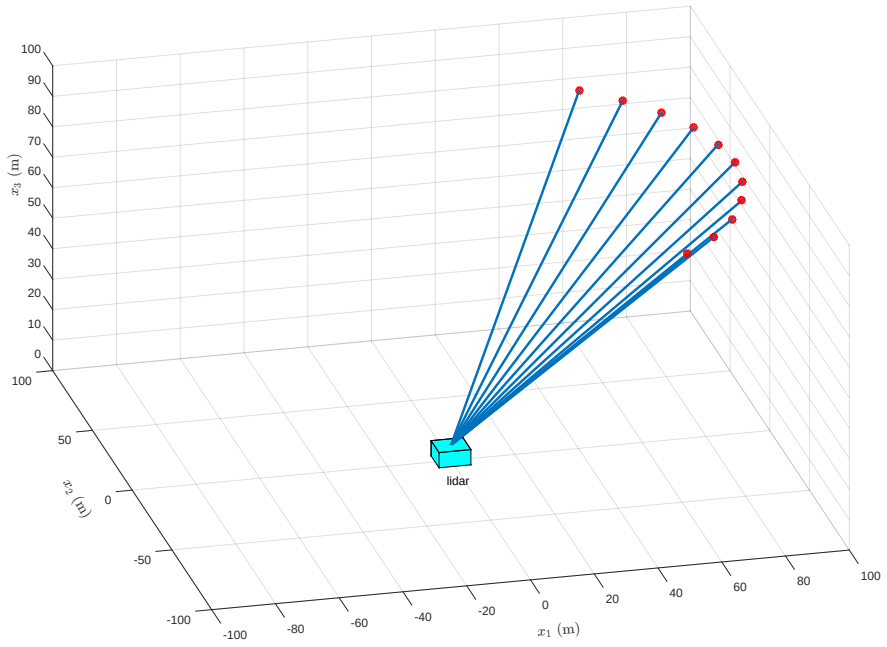

Figure 3.5: Arc Scanning

Fig. 3.5 shows the arc-scanning technique, where similar to the VAD technique of data processing, the wind vector components are deduced from the v_{r} measurements at different θ for a given ϕ (see Eq. 3.1). However the scan is restricted to only an arc, where for example θ varies between 0 and 60°, as opposed to 0 and 360° for a full VAD conical scan. One of the obvious advantages of this method is the increase in the sampling frequency, which potentially can capture more (smaller) turbulence scales as compared to the VAD technique. A disadvantage could be increased uncertainty due to random selection of the arc angle within which the measurements are performed.

3.2.5 Triple lidar systems - WindScanners

One of the biggest disadvantages of using a single lidar is the necessity of the horizontal homogeneity assumption that almost precludes its use in complex terrains/flows, as well as within wind turbine wakes. We are then forced to use a triple lidar system, where the beams cross at a point. Fig. 3.6 shows such a system. The wind vector components can be deduced from the v_{r} measurements of the three beams. With the ability of lidars to scan in space and meticulous design of synchronizing the beams, measurements from different points in space can be obtained in any kind of terrain/flows.

Deducing the wind vector components is then straightforward. If we denote estimates of radial velocities from the three beams as a vector $\mathbf{v}_{\mathrm{r}} = (v_{\mathrm{r}_1}, v_{\mathrm{r}_2}, v_{\mathrm{r}_3})$, and $\mathbf{N}$ as a 3×3 matrix of trigonometric coefficients (consisting of ϕ and θ) of the wind vector components then from Eq. (3.1) $\mathbf{v}$ can be written as,

$$\mathbf{v} = N^{-1}\mathbf{v}_{\mathrm{r}} \tag{3.20}$$

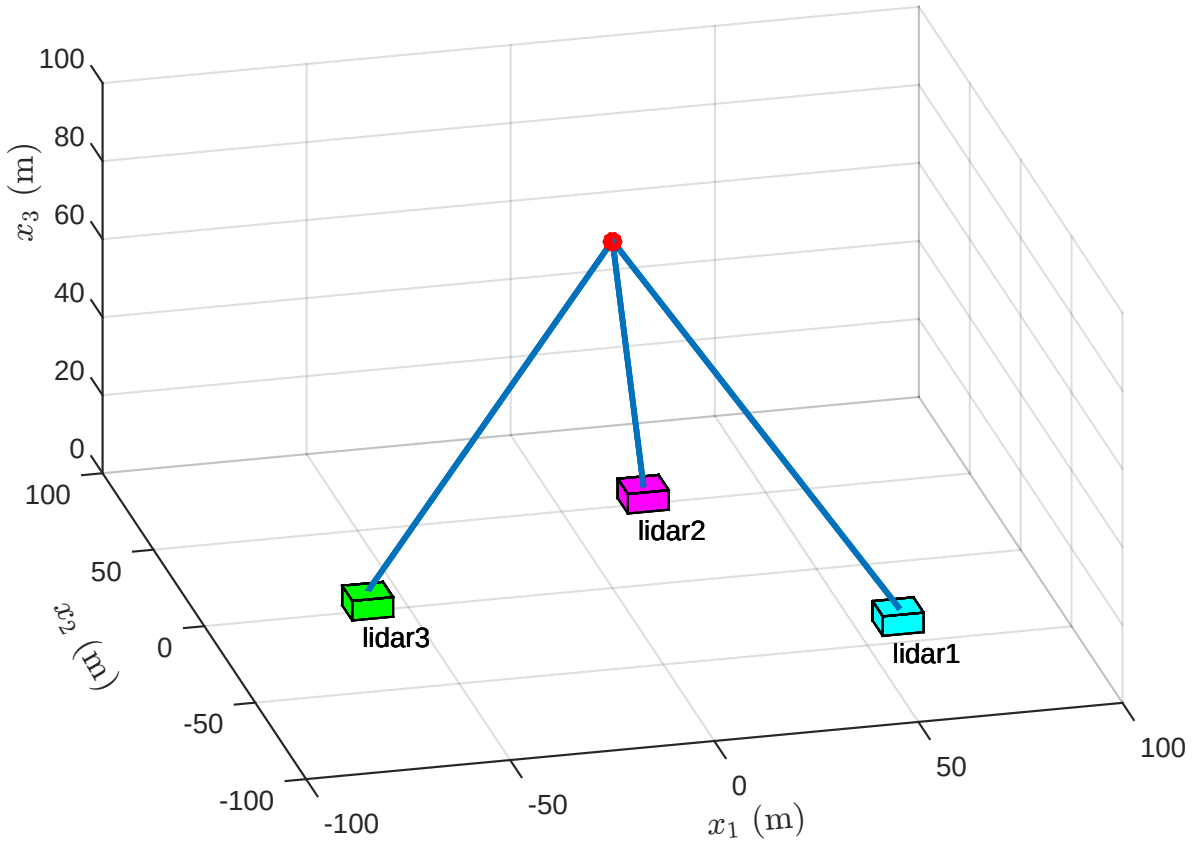

Figure 3.6: Three lidars measuring at one height

3.2.6 Dual lidar systems

Fig. 3.7 shows the dual lidar system, where only two lidars are used to deduce two wind vector components. Usually it is assumed that the vertical component (w) is very small compared to the horizontal components u and$v$, but it requires very small elevation angles α (and consequently large scanning distances) as can be seen in Fig. 3.7 [Newsom et al., 2015]. Such a system can be quite useful in scanning an offshore wind field, where the three lidar systems may not be practical to use. Also an additional savings in the costs can be achieved by getting rid of one lidar.

3.2.7 Nacelle-Based Lidar

Fig. 3.8 shows an example of scanning from a nacelle-based lidar from a spinner/nacelle lidar developed by DTU Wind Energy. Different scanning patterns can be produced, e.g. in commercial lidars such as the Leosphere Avent lidar, only five points are scanned, whereas a ZephIR nacelle lidar scans a circle. Several factors need to be considered before analyzing the measurements from a nacelle-based lidar. Amongst others, the most important is the identification of the blade passing events, which is not straightforward especially at low wind speeds. Estimating the wind vector components, and consequently the components of $\mathbf{R}$ can be carried out in different ways, depending on the scanning pattern, and the number of available beams. In principle Eq. (3.1) can be used with only three scan points. However the assumption of homogeneity of the wind vector components over the scanning plane that is

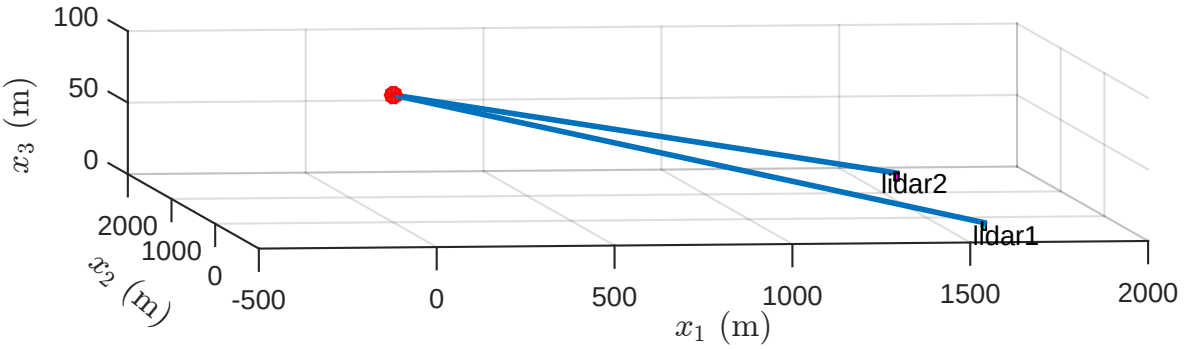

Figure 3.7: Two lidars measuring at one height

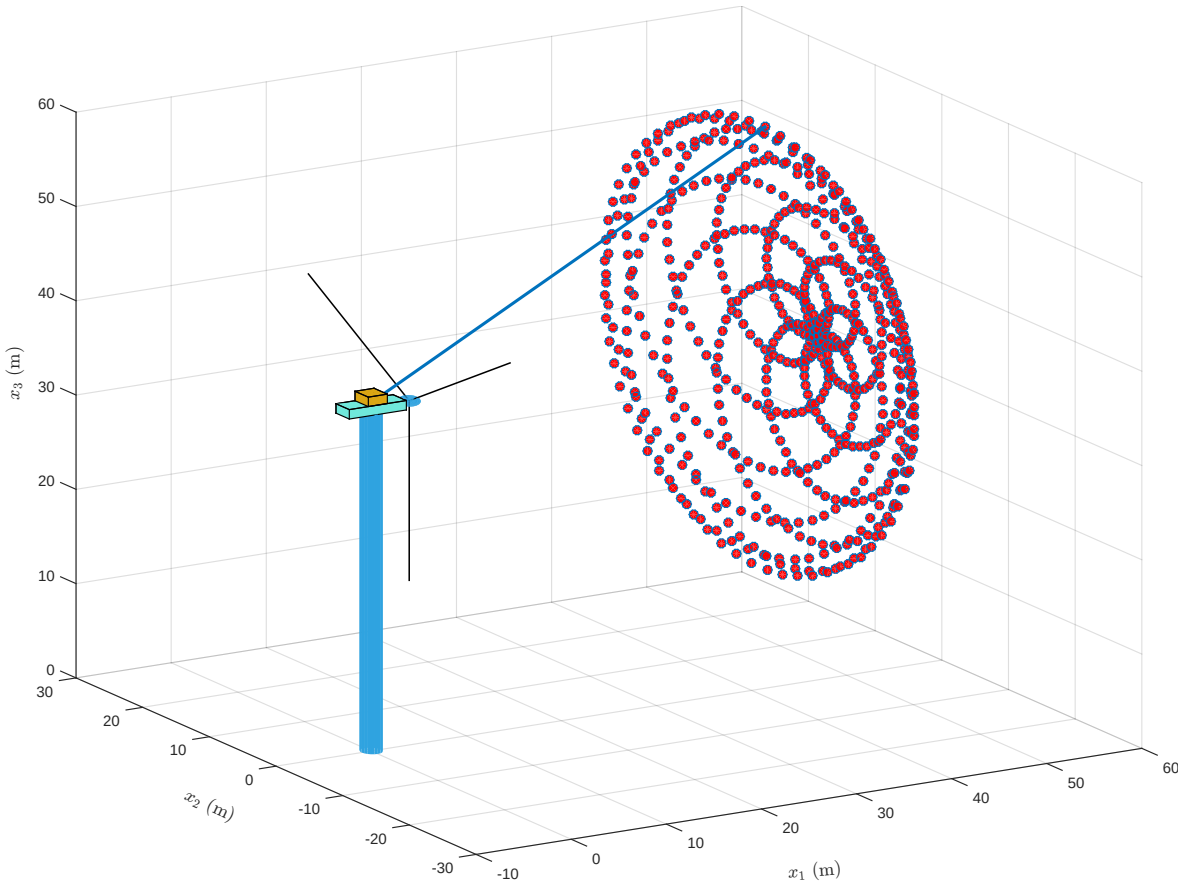

Figure 3.8: Scanning from a Nacelle-Based Lidar

central to the use of Eq. (3.1) is more likely to be violated in the vertical plane than in the horizontal plane. Therefore, it is recommended to use Eq. (3.1) in combination with some

mean wind profile model in order to remove the vertical inhomogeneities.

3.2.7.1 Estimating components of R

Equation (3.16) can in principle also be used to estimate the components of **R**. As with the wind vector components, the assumption of homogeneity of R_{ij} is more likely to fail in a vertical plane than in the horizontal plane. Nevertheless, considering that the industry standard Mann [1994] model is used to simulate a three-dimensional wind field, which assumes homogeneity in all directions, Equation (3.16) can still be worthwhile to estimate R_{ij}. It is to be noted that as for the six-beam method, at least two cone angles are required for Eq. (3.16) to work (see section 3.2.2).

Another method of estimating **R** is the model-based wind field reconstruction from Schlipf et al. [2012] that can be applied to obtain the time series of the u, v, and w components. If we denote n_b as the number of beams, and if we have v_r measurements from $3 \leq n_b < 6$, then assuming u, v, and w are equal in all measurement points, Eq. (3.1) can be written for several measurements in the form

$$\begin{bmatrix} v_{r,1} \\ \vdots \\ v_{r,n_b} \end{bmatrix} = \underbrace{\begin{bmatrix} n_{1,1} & n_{2,1} & n_{3,1} \\ \vdots & \vdots & \vdots \\ n_{1,n_b} & n_{2,n_b} & n_{3,n_b} \end{bmatrix}}_{A} \begin{bmatrix} u \\ v \\ w \end{bmatrix}, \tag{3.21}$$

where the u, v, and w are obtained in each time point by inverting the measurement matrix A. For $n_b > 3$, the MooreâĂŞPenrose pseudoinverse or a least square method (equivalent to each other) can be used. The components of **R** can then be calculated from the u, v, and w time series. It is to be noted that this method is very similar to that explained in section 3.1 for the ground-based lidars, and therefore will be subjected to the probe volume filtering effects and the cross contamination by wind vector components described for the ground-based lidars in section 3.1.

3.2.8 Volumetric scanning

Scanning, pulsed Doppler lidar can be used to provide a 3-D volume of atmospheric radial-velocity measurements by scanning a sector, incrementing moving the lidar pointing angle a small increment in the direction orthogonal to the sector scan direction, then repeating the sector scanning and orthogonal incrementing until the desired volume is completed. A depiction of this volume scan pattern for azimuth (conical) sector scanning is shown in Fig. 3.9. Such a 3-D volume can be used in a retrieval technique called four-dimensional variational data assimilation (4DVAR) to provide a 3-D Cartesian grid volume of u, v, w, θ and pressure that may be several kilometers across at data intervals that resolve the large eddies of the atmospheric boundary layer, at least for the daytime unstable mixed layer [Newsom and Banta, 2004a]. The resulting retrieved volume of kinematic and thermodynamic data, resembling the output of large-eddy simulation (LES) models, can be analyzed in a manner similar to such models to give mean profiles of the calculated quantities and to calculate variances and covariances (fluxes) of the deviations from those means. A major difference between these approaches is that in the 4DVAR volume, the magnitudes and scales of the fluctuations are constrained by the measurements, whereas the eddy structure of the LES fields is purely model driven.

The retrieval is accomplished by fitting the output of a prognostic model to the lidar volume measurements. The model initial conditions serve as control parameters that are adjusted in an iterative procedure to optimize agreement between the lidar measurements and

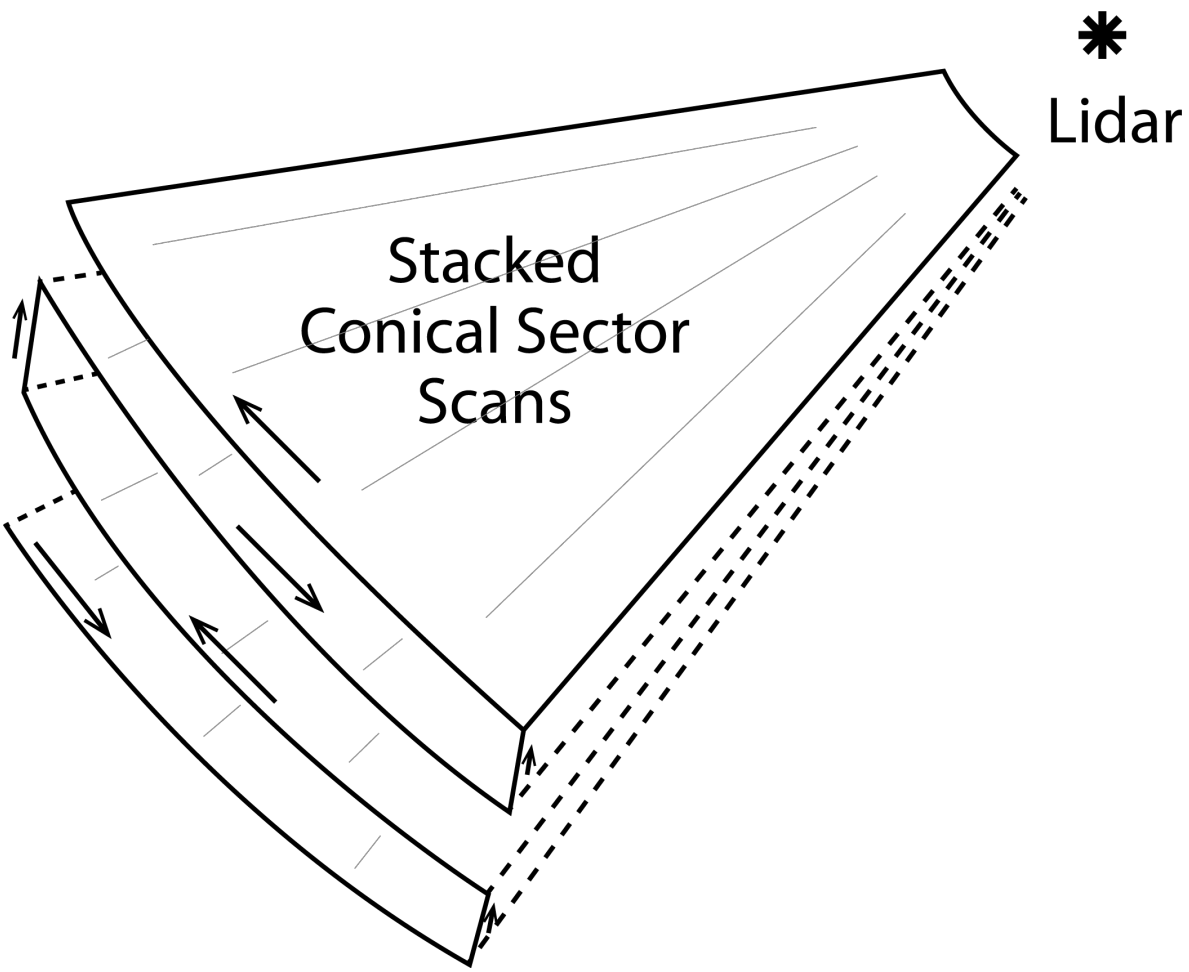

Figure 3.9: 3-D volume scanning pattern for four repeated azimuth sector scans, with each successive sector executed at increasing elevation angles.

the model predictions of radial velocity. Newsom and Banta [2004a,b] altered and adapted the scheme developed for Doppler radar, then applied it to a Doppler lidar dataset of 8 sequential 3-D volumes obtained using NOAA's high-resolution Doppler lidar (HRDL, [Grund et al., 2001]) during afternoon convective boundary layer (CBL) conditions over Kansas, in the U.S. Great Plains. Turbulence quantities calculated from the retrieved 3-D volumes, such as velocity and θ variances and fluxes, exhibited the profiles shapes expected in a CBL, for example, the retrieved heat-flux profile is linear through the CBL and negative at the top.

Chapter 4

State-of-the-art

Estimation of the turbulence statistics using lidars has been a topic of research since the 1970s, but there has been a significant growth in lidar turbulence studies since the mid 1990s. Several measurement configurations as described in chapter 3 have been used in the past studies. Sathe and Mann [2013] summarize these studies, where mathematical formulations of the deduced turbulence statistic is also presented. In this chapter we only classify the turbulence studies based on the estimated turbulence statistic defined in chapter 1. A reader who is interested in mathematical formulations is referred to section 4.1 of Sathe and Mann [2013].

Until the mid- and late 1990s, the focus was more on developing new data-processing methods to extract turbulence information. New algorithms for efficiently processing the raw lidar data are still being developed, as seen in the recent work by Mann et al. [2010]. Nevertheless, many studies have benefited from the continuous developments in the past, where simulation studies and measurement campaigns have been carried out. Because lidar is not yet an established technology to measure atmospheric turbulence, it is important to compare lidar measurements with a reference instrument, as emphasized in the review article by Wilczak et al. [1996]. In their review, lidar technology was termed to be a "young adult" in comparison to sodars and radars. With the recent spurt in the measurement campaigns using lidars, we think that it has grown beyond its status of "young adult".

Table 4.1 groups the studies that have focused on estimation of turbulence quantities using either simulation or lidar measurements. For each turbulence quantity, the total number of studies is also given. It is evident that significant effort has been focused on estimation of ε, followed by R_{ij}, ℓ_{ij}, outer length scale of turbulence $\mathscr{L}$, radial velocity variance $\langle v_{\mathrm{r}}'^2 \rangle$, filtered radial velocity structure function $\tilde{D}(r)$for a separation distance r, filtered radial velocity spectrum $\tilde{F}(k_1)$, and $F_{ij}(k_1)$.

Table 4.1: Grouping of the past studies according to the estimated turbulence quantity using a lidar.

No.	Quantities Estimated	List of references	Total

1	Turbulent kinetic energy dissipation rate, ε	Banakh and Smalikho [1997a,b], Banakh and Werner [2005], Banakh et al. [1995b, 1996, 1997, 1999, 2010], Chan [2011], Collier et al. [2005], Davies et al. [2004, 2005], Davis et al. [2008], Dors et al. [2011], Drobinski et al. [2000], Frehlich [1997], Frehlich and Cornman [2002], Frehlich and Kelley [2008], Frehlich et al. [1994, 1998, 2006, 2008], Gal-Chen et al. [1992], Kristensen et al. [2011, 2012], Kunkel et al. [1980], Lothon et al. [2009], O'Connor et al. [2010], Smalikho et al. [2005]	29
2	Components of the auto-covariance matrix, R_{ij}	Banta et al. [2006], Cohn et al. [1998], Collier et al. [2005], Davies et al. [2003, 2005], Davis et al. [2008], Drobinski et al. [2004], Eberhard et al. [1989], Frehlich et al. [1998], Gal-Chen et al. [1992], Kunkel et al. [1980], Lang and McKeogh [2011], Mann et al. [2010], Pichugina et al. [2008], Sathe et al. [2011b], Tucker et al. [2009], Wagner et al. [2009]	17
3	Integral turbulent length scale ℓ_{ij}, outer scale of turbulence $\mathscr{L}$	Banakh and Werner [2005], Banakh et al. [1999], Cohn et al. [1998], Collier et al. [2005], Davies et al. [2004, 2005], Drobinski et al. [2000], Frehlich [1997], Frehlich and Cornman [2002], Frehlich and Kelley [2008], Frehlich et al. [1998, 2006, 2008], Lothon et al. [2006, 2009], Smalikho et al. [2005]	16
4	Radial velocity variance, $\langle {v'_{\mathrm{r}}}^2 \rangle$	Banakh and Werner [2005], Branlard et al. [2013], Davies et al. [2004], Drobinski et al. [2000], Eberhard et al. [1989], Frehlich [1997], Frehlich and Kelley [2008], Frehlich et al. [1998, 2006, 2008], Gal-Chen et al. [1992], Mayor et al. [1997]	12
5	Filtered radial velocity spectrum, $\tilde{F}(k_1)$	Angelou et al. [2012], Banakh et al. [1997, 1999], Davies et al. [2004], Dors et al. [2011], Drobinski et al. [1998, 2000], Frehlich et al. [1998], Kristensen et al. [2011], Mann et al. [2009], Mayor et al. [1997], Sjöholm et al. [2009]	12
6	Filtered radial velocity structure function, $\tilde{D}(r)$ (or $\tilde{D}(r_1)$)	Banakh and Smalikho [1997b], Banakh et al. [1999, 2010], Chan [2011], Davies et al. [2004], Frehlich [1997], Frehlich and Cornman [2002], Frehlich et al. [1994, 1998, 2008], Kristensen et al. [2011, 2012]	12
7	One-dimensional spectrum of the components of the wind vector, $F_{ij}(k_1)$	Canadillas et al. [2010], Davies et al. [2005], Drobinski et al. [2004], Hardesty et al. [1982], Lawrence et al. [1972], Lothon et al. [2009], O'Connor et al. [2010], Sathe and Mann [2012]	8
8	Third order moments $\langle {w'}^3 \rangle$	Cohn et al. [1998], Gal-Chen et al. [1992], Lenschow et al. [2000]	3

9	Kinematic heat flux, $\langle w'\theta' \rangle$	Davis et al. [2008], Gal-Chen et al. [1992]	2
10	Coherence of the components of the wind vector, $\mathrm{coh}_{ij}(k_1)$	Kristensen et al. [2010], Lothon et al. [2006]	2

4.1 ε, $\tilde{F}(k_1)$, $\tilde{D}(r)$

The greatest advantage of estimation of ε is that we can exploit the universal behavior of isotropy in the inertial subrange, either in the Fourier domain (using velocity spectrum) or the temporal domain (using structure function) [Pope, 2000]. Thus, estimation of ε involves estimation of either $\tilde{F}(k_1)$ or $\tilde{D}(r)$ in the inertial subrange from the lidar beam that is oriented in any direction. The associated challenges are then threefold: proving the existence of the inertial subrange, identifying the inertial subrange from the lidar data, and averaging inside the probe volume. From Pope [2000], we understand that in order to have a well-defined inertial subrange, we need large Reynolds number flows. Fortunately, atmospheric flows are usually characterized by large Reynolds numbers [Wyngaard, 2010], especially during convective daytime conditions. Stable atmospheric conditions that normally occur during the late night and early morning, can however present challenges since they are associated with low Reynolds number turbulence [Wyngaard, 2010]. We can then assume that inertial subrange is well defined for most of the day, except during late night and early morning conditions.

The challenge associated with identifying the inertial subrange from lidar measurements is mainly due to the probe length of a lidar. In principle, we need only one measurement – of either $\tilde{F}(k_1)$ or $\tilde{D}(r)$ – in the inertial subrange. However, in order to avoid statistical uncertainty, it is recommended that one take multiple measurements, and fit a model to these measurements. From Mann et al. [2009], Sjöholm et al. [2009] and Sathe [2012], it is clear that due to the probe length of a lidar, most of the turbulence scales in the inertial range are filtered out. Modeling the lidar filter function then becomes inevitable, which has fortunately been carried out by Smalikho [1995], Banakh et al. [1996], Frehlich [1997], Smalikho et al. [2005], Sjöholm et al. [2009] and Mann et al. [2009]. In Sjöholm et al. [2009] and Mann et al. [2009], the goal was only to compare the lidar volume-averaged measurements of the radial velocity spectrum with reference point measurements; an estimation of ε was not carried out. These studies could be extended further to estimate ε by using the isotropic or anisotropic form of spectral tensor with a given energy spectrum. Apart from the filtering effect, we also need to identify the cut-off low wavenumber range when using $\tilde{F}(k_1)$, and the maximum separation distance when using $\tilde{D}(r)$ in order to identify the inertial subrange.

In summary, there are four ways of estimating ε: width of the Doppler spectra (Smalikho, 1995; Banakh et al., 1995a, 2010; Smalikho et al., 2005), radial velocity spectrum [Banakh and Smalikho, 1997a, Banakh et al., 1995b, 1997, Collier et al., 2005, Davies et al., 2005, Davis et al., 2008, Dors et al., 2011, Drobinski et al., 2000, Gal-Chen et al., 1992, Kristensen et al., 2011, Lothon et al., 2009, O'Connor et al., 2010], line-of-sight radial velocity structure function [Banakh and Smalikho, 1997a,b, Banakh and Werner, 2005, Banakh et al., 1999, Davies et al., 2004, Frehlich, 1997, Frehlich and Cornman, 2002, Frehlich et al., 1994, 1998, Smalikho et al., 2005], and radial velocity azimuthal structure function [Banakh and Smalikho, 1997a, Banakh et al., 1996, 1999, Chan, 2011, Frehlich and Kelley, 2008, Frehlich et al., 2006, 2008, Kristensen et al., 2012]. Very few studies have exploited the Doppler spectral width to estimate ε; the reasons could be that for a C-W lidar the applicability of the Doppler spectral width is limited to $l \ll \mathscr{L}$, and for a pulsed lidar it is quite complicated to process the data

[Smalikho et al., 2005]. Nevertheless, as shown by Banakh et al. [2010], for a pulsed lidar it could be advantageous to use the Doppler spectral width approach, since the random errors in ε can be reduced at higher turbulence levels than they can in the structure function approach, or equally, using the radial velocity spectrum approach.

4.2 $\langle v_r'^2 \rangle$, ℓ_{ij}, $\mathscr{L}$

Apart from ε, another important parameter that characterizes turbulence is the length scale. The two most commonly used definitions of the length scale are ℓ_{ij} and $\mathscr{L}$, which have physically different interpretations. $\mathscr{L}$ (also called the outer length scale of turbulence) is the length scale corresponding to the maximum spectral energy, whereas ℓ_{ij} can be interpreted as the length scale up to which turbulence is correlated. The two scale lengths can, however, be shown to be related to each other, as was done by Frehlich and Cornman [2002], Smalikho et al. [2005] and Lothon et al. [2006]. Thus, ℓ_{ij} can be estimated from its relationship with $\mathscr{L}$ [Collier et al., 2005, Davies et al., 2004, Frehlich and Cornman, 2002, Frehlich et al., 2006, Lothon et al., 2006, 2009, Smalikho et al., 2005], or by using the definition given in Eq. (1.4) [Cohn et al., 1998]. Practically, ℓ_{ij} is estimated from the values of the autocorrelation function at the first zero crossing, but Davies et al. [2005] estimated the same using some properties of the autocorrelation function. $\mathscr{L}$ can be estimated using the structure function approach [Frehlich, 1997, Frehlich and Kelley, 2008, Frehlich et al., 1998, 2008]. Drobinski et al. [2000] followed a slightly different approach, in which the radial velocity spectrum is split into two regions; one is the energy-containing range, and the other contains the inertial subrange up to the dissipation range. Measurements of the radial velocity spectrum can thus be fitted to this model and $\mathscr{L}$, ε estimated simultaneously. Interestingly, Banakh et al. [1999] and Banakh and Werner [2005] also use the term outer length scale for ℓ_{ij}, but we believe that it is important to distinguish between the two length scales.

Fewer studies have been carried out to estimate $\langle v_r'^2 \rangle$ than to estimate ε (see Table 4.1). This is perhaps because information of all turbulence scales is required to estimate $\langle v_r'^2 \rangle$, and a universal isotropic relation does not suffice. Although Eberhard et al. [1989] and Gal-Chen et al. [1992] have estimated $\langle v_r'^2 \rangle$ from lidar measurements, no consideration to probe volume averaging was given, and thus any other turbulence statistic derived using these measurements would not contain information on small-scale turbulence. All subsequent studies have followed the pioneering work of Frehlich [1997], in which information about small-scale turbulence was recovered by modeling the filter function. The main contributions of the Frehlich [1997] method are first, that it presents a technique to derive expressions of the radial velocity structure function (or, equivalently, the radial velocity spectrum) for a lidar pulse with any given shape; second, it presents a turbulence model, with which we can estimate $\langle v_r'^2 \rangle$ and ℓ_{ij}. One can thus use a non-Gaussian shape for the pulse and derive a different functional form of the spatial filter [Davies et al., 2004], or use a different turbulence model, e.g. von Kármán [1948] isotropic spectral tensor model [Frehlich and Cornman, 2002], or a more realistic anisotropic Mann [1994] spectral tensor instead of the empirical Kaimal et al. [1972] models [Frehlich, 1997, Frehlich et al., 1998]. Using $\tilde{D}(r)$ to estimate $\langle v_r'^2 \rangle$ from a pulsed lidar has the limitation of coarse vertical resolution. An azimuthal structure function approach can then be used to improve the vertical resolution [Banakh et al., 1996, Frehlich and Kelley, 2008, Frehlich et al., 2006, Kristensen et al., 2012]. Without using any turbulence model, Mann et al. [2010] suggested a technique (only for C-W lidars) to estimate $\langle v_r'^2 \rangle$ using the mean Doppler spectrum. The validity of this technique is successfully demonstrated in Branlard et al. [2013].

4.3 R_{ij}, $F_{ij}(k_1)$

R_{ij} is one of the most important turbulence statistics used in the wind energy industry, due to the use of $\langle u'^2 \rangle$ in the definition of turbulence intensity (see Eq. 1.3). Unfortunately, it is also one of the most challenging statistics to obtain from the lidar data, partly due to challenges in data processing, and partly due to economic reasons. If economics is not a major constraint, then three lidars with beams intersecting at one point will provide spatially filtered turbulence statistics [Mann et al., 2009]. With two lidars, we are restricted to estimating the turbulence statistics of only two components, i.e., horizontal and vertical [Collier et al., 2005, Davies et al., 2005].

Normally, the economics of a project are important and we are then restricted to using only one lidar. In this case, a lidar beam can be oriented in the direction of the turbulence statistic that we are interested in estimating. For example, if we are interested in estimating $\langle u'^2 \rangle$, then ideally the lidar beam should be pointed horizontally in the mean wind direction at the height of interest, and for the period within which $\langle u'^2 \rangle$ is obtained [Lawrence et al., 1972]. For a ground-based lidar system this would be impossible since the beam would only measure wind that is very close to the ground. Alternatively, we could point the lidar beam at a very small elevation angle and assume that the contributions from the vertical velocity are negligible [Banta et al., 2006, Collier et al., 2005, Drobinski et al., 2004, Pichugina et al., 2008]. An open question then is, how small the elevation should be so that the vertical velocity contributions can be neglected? Drobinski et al. [2004], Banta et al. [2006], and Pichugina et al. [2008] neglected the vertical velocity contributions up to an elevation angle of 20°, but provided no justification for the assumption of negligible vertical velocity contributions. This method also requires that the horizontal homogeneity assumption is valid over a larger area, particularly if we are interested in measuring turbulence statistics at greater heights and/or several heights. Measurements of $\langle w'^2 \rangle$ can be relatively easier to take, since we only need to point the beam in the vertical direction [Cohn et al., 1998, Tucker et al., 2009]. In principle, following Frehlich [1997] and Banakh and Smalikho [1997b] approach, we can then obtain unfiltered $\langle w'^2 \rangle$ from $\langle v_r'^2 \rangle$.

R_{ij} can also be obtained using scanning lidar data, either using RHI scanning [Davies et al., 2003, Davis et al., 2008, Gal-Chen et al., 1992] or VAD scanning [Eberhard et al., 1989, Mann et al., 2010]. If, say for a VAD scan, we use use high-frequency v_r measurements, deduce the u, v, and w components at every measurement time step, and obtain, say, $\langle u'^2 \rangle$ or $F_{11}(k_1)$, then apart from the probe volume averaging effect, large systematic errors will also be introduced in the measurement of $\langle u'^2 \rangle$ due to the contamination by the diagonal and cross components of $\mathbf{R}$ [Sathe and Mann, 2012, Sathe et al., 2011b]. In such cases, one should be very careful in using the R_{ij} measurements obtained from a scanning lidar, since removing only the probe volume filtering effect [Wagner et al., 2009] without giving consideration to cross-contamination, or neglecting the effects of systematic errors completely [Lang and McKeogh, 2011] will provide erroneous values. Using $\langle v_r'^2 \rangle$ instead of high frequency v_r measurements to obtain R_{ij} is then essential in order to avoid contamination by the components of $\mathbf{R}$ [Eberhard et al., 1989, Gal-Chen et al., 1992, Mann et al., 2010, Sathe, 2012]. The cross-contamination effect is minimized using the six-beam method, but compensating for the spatial averaging effects for pulsed lidars still remains a challenge. Experimental evidence suggests that the six-beam method partly overcomes the problem of significant probe volume averaging that is otherwise observed by the VAD method [Sathe et al., 2015]. The unfiltered $\langle v_r'^2 \rangle$ can be obtained using methods suggested by Frehlich [1997] and Mann et al. [2010], and hence unfiltered R_{ij} will also be obtained.

Estimating $F_{ij}(k_1)$ from lidar data is even more challenging than estimating R_{ij}, since we need high frequency measurements of v_r. For a scanning lidar, combining high frequency

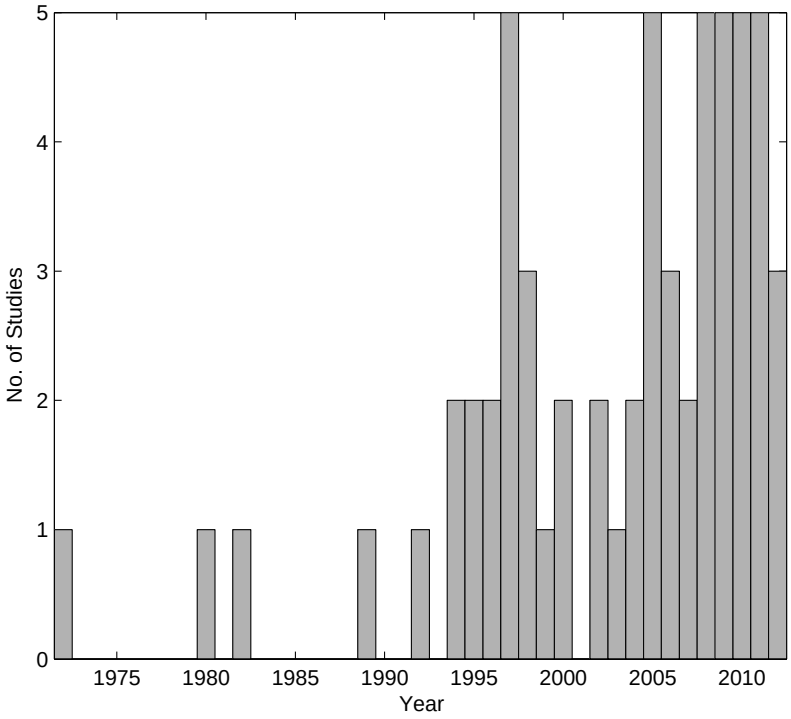

Figure 4.1: Number of studies per year on lidar turbulence measurements.

measurements from the lidar beams oriented in different directions (VAD method) results in erroneous measurements of $F_{ij}(k_1)$ [Canadillas et al., 2010, Sathe and Mann, 2012]. Most studies in the past have thus used either a staring lidar configuration [Davies et al., 2005, Lawrence et al., 1972, Lothon et al., 2009, O'Connor et al., 2010], or neglected contributions from the w component at small elevation angles [Drobinski et al., 2004, Hardesty et al., 1982].

4.4 $\langle w'^3 \rangle$, $\langle w'\theta' \rangle$, $\mathbf{coh}_{ij}(k_1)$

Very little effort has been focused on the estimation of the third order moment $\langle w'^3 \rangle$, $\langle w'\theta' \rangle$ and $\mathrm{coh}_{ij}(k_1)$. One of the reasons could be the complexity of data processing and the associated errors that present great challenges in their estimations. Particularly, an estimation of $\langle w'\theta' \rangle$, requires not only an estimation of ε, but also requires estimation of either $\langle w'^3 \rangle$ [Gal-Chen et al., 1992], or $\langle w'^2 \rangle$ [Davis et al., 2008]. Estimating higher order moments, particularly third and fourth order, introduce large errors in the measurements [Lenschow et al., 1994, 2000]. Fortunately, we can reduce the errors in higher moments using the autocorrelation technique [Lenschow et al., 2000] or the spectral technique [Frehlich et al., 1998], which increase the potential of estimating the heat flux using the [Gal-Chen et al., 1992] method. Schlipf et al. [2015] investigated the coherence between the longitudinal wind component u in two points, where a simple exponential model suggested by Pielke and Panofsky [1970] was assumed. This campaign resulted in a realistic estimate for the decay parameter. Simley and Pao [2015] fitted a simple coherence model, based on a formula for transverse and vertical coherence developed by Thresher et al. [1981] to coherence curves calculated from large-eddy simulation (LES).

4.5 Summary

Figure 4.1 summarizes the number of studies that have significantly contributed to the research on turbulence measurements using wind lidars from 1972–2012. Research on lidar turbulence measurements dates back to 1972, but it was not until 1997 that the publication rate picked up pace. If we consider that the lidar turbulence measurement research encompasses the period 1972–2012, then more than 80 % of the research was carried out in the latter half of the 40 year period, i.e., from 1997–2012. In the first 25 years of development, barring the works of Smalikho [1995] and Banakh et al. [1996], focus was more on extracting turbulence information without taking into account probe volume averaging. Since then substantial effort has been put into modeling the averaging effect inside the lidar probe volume, mainly by Professor V. A. Banakh and Dr. I. N. Smalikho from the V. E. Zuev Institute of Atmospheric Optics of Russian Academy of Sciences, Siberian Branch, Russia, and the late Dr. R. Frehlich from the University of Colorado, USA. Interestingly, these scientists pioneered new processing algorithms independently of each other during roughly the same period, i.e. from the mid 1990s until the mid 2000s, wherein they demonstrated how to extract unfiltered turbulence parameters [Banakh and Smalikho, 1997b, Banakh et al., 1996, Frehlich, 1997, Frehlich et al., 2006, Smalikho et al., 2005, Smalikho, 1995]. We believe that this development has significantly contributed to the number of research studies carried out in the last 15 years. Further development in processing algorithms will also greatly benefit from their works. We expect that the number of such studies will continue to increase due to increase in wind-energy development all over the world.

Chapter 5

Experimental Campaigns Across the World

In this chapter we provide details of some of the studies and experimental campaigns using lidars that have been carried out across the world with a focus on estimated turbulence statistics. Different methods of post processing the lidar data have been applied, and a variety of turbulence statistics estimated. Amongst others the commonly estimated turbulence statistics are the components of $\mathbf{R}$ and $F_{ij}(k_1)$. It is usually not straightforward to report different studies in a consistent manner. Therefore the reporting is structured such that for each study, at first the objective is stated clearly followed by the site and instrument details. Subsequently the illustrations of the mean and turbulence statistics are provided. In many studies the estimated turbulence statistics are compared with those estimated by some reference instrument such as a cup or a sonic anemometer. It is therefore important to know beforehand the measurement uncertainty of the reference instrument itself. According to JCG [2008], measurement uncertainty can be quantified as the dispersion of the measurand. Owing to a lack of a standard procedure, it is not straightforward to estimate the measurement uncertainty of the sonics, but is usually available for cup anemometers. Therefore where available they are stated along with the measurement uncertainty of the lidars used. It is to be noted that although the studies are numbered sequentially they are not sorted according to the dates of the experimental campaigns.

Because modern day lidars are known to measure the mean wind speeds as accurately and precisely as the reference cup/sonic anemometers, the illustrations of the mean wind speed comparisons provide an initial check that further provide reasonable confidence in the estimated turbulence statistics. In other words if the comparisons between the mean wind speeds estimated using a lidar and those estimated using a reference instrument are quite poor then there is very little reason to trust the estimation of the turbulence statistics for that experimental campaign.

5.1 Study 1 – Høvsøre, Denmark

5.1.1 Introduction

The objective of this study was to understand the estimation of the components of $\mathbf{R}$ (see Eq. 1.2), where the VAD method (see section 3.1.1) was used in post processing the lidar data. Modelling of the estimated $\mathbf{R}$ using the VAD method was carried out, and measurements from two (a CW and a pulsed) commercial lidars were used to verify the model. Comparisons of the estimated R_{ij} from the model and the data were also carried out with those estimated

by reference sonic anemometers at different heights. For details on the model the reader is referred to [Sathe et al., 2011b].

5.1.2 Measurement details

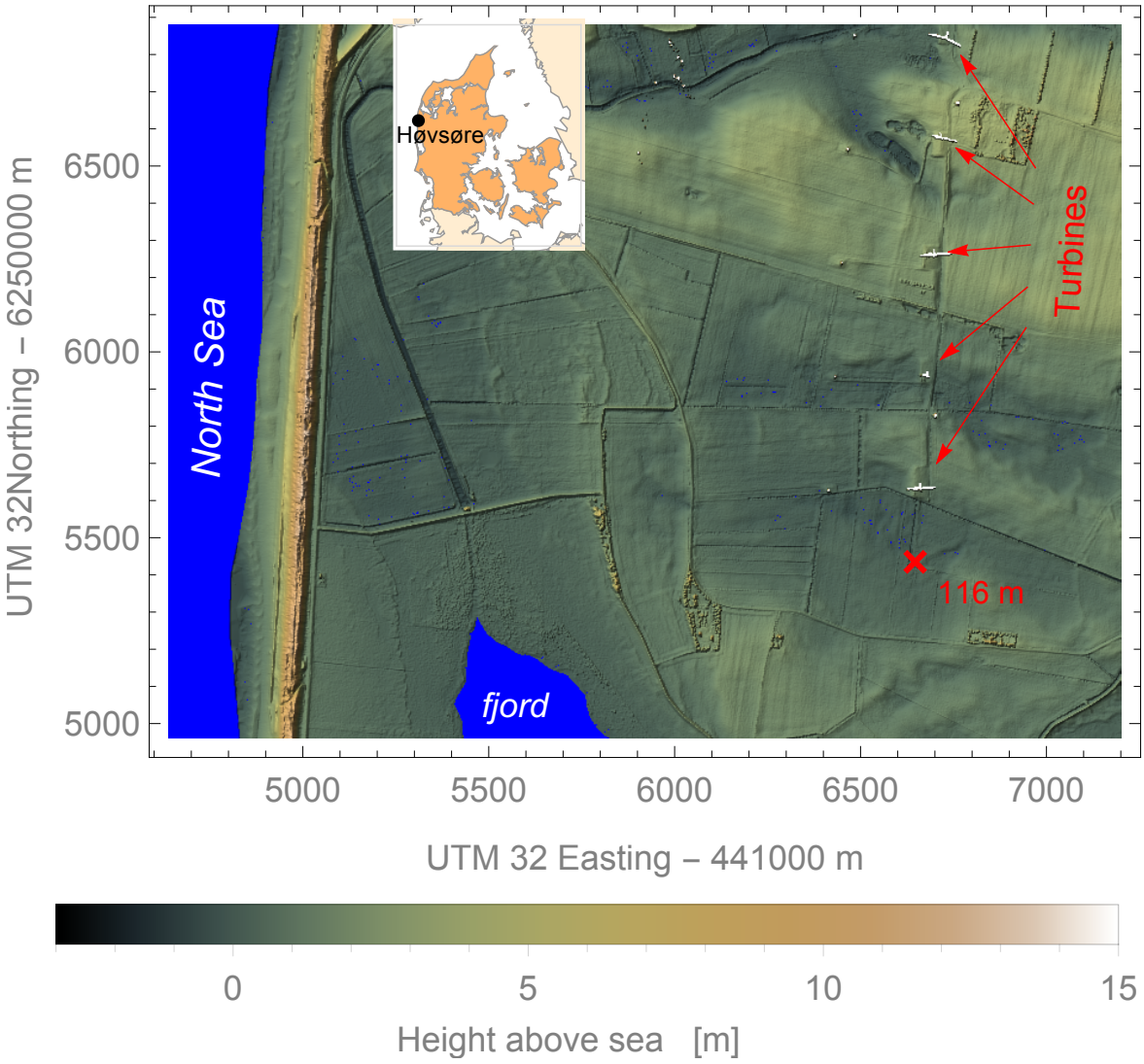

Figure 5.1: Location of the test site at Høvsøre, Denmark

The measurements were performed at the Danish National Test Center for Large Wind Turbines at Høvsøre, Denmark. Figure 5.1 shows the location of the test center in Denmark (see inset in Fig. 5.1). The site is about 1.7 km east from the North Sea at a mean height of 2 m above mean sea level. The Nissum Fjord lies ≈ 800 m south of the station's 116.5 m tall met mast. The site also comprises five turbine stands, which turbine manufacturers rent for the machine's testing and research. Besides this, (not shown in Fig. 5.1) there are five power curve masts, two lighting towers and a central service building. The eastern sector is characterized by a relatively flat homogeneous terrain.

The lidar measurements were used from two different types of commercial lidars, a CW ZephIR lidar and a pulsed WindCube lidar. The reference measurements were used from the sonic anemometers installed at different heights on a 116.5 m mast, also known as the Høvsøre met mast (see Fig. 5.2). The mast is an equilateral triangular lattice structure, where

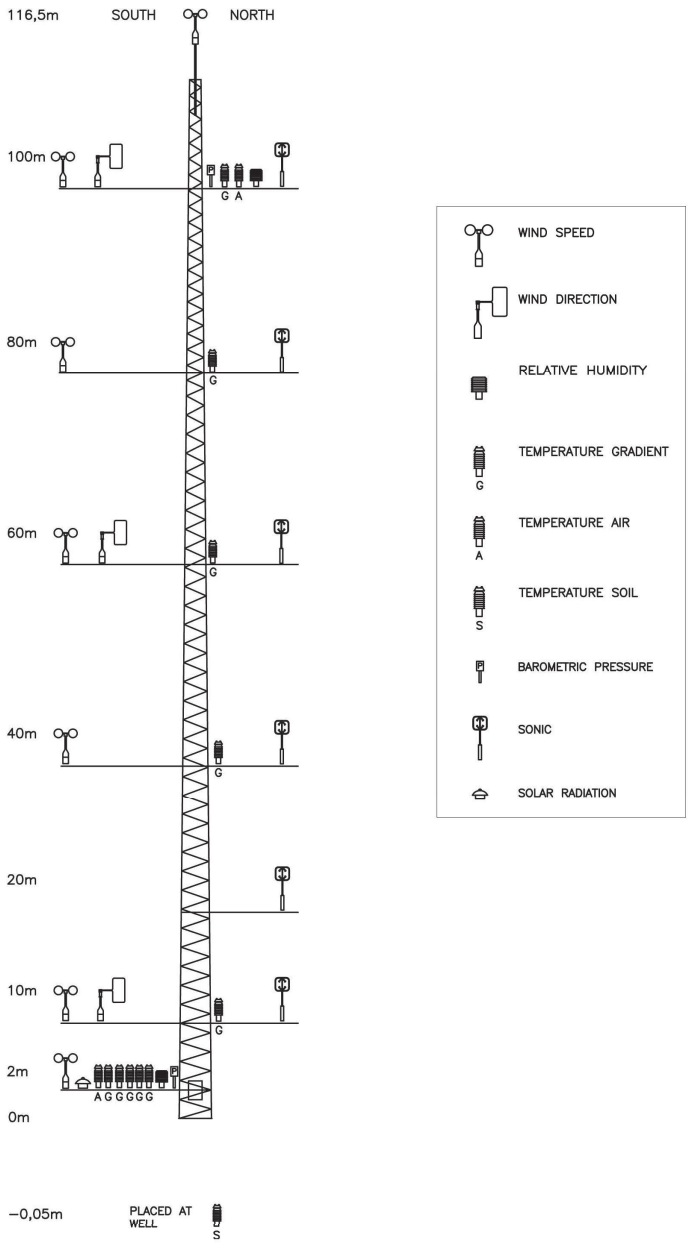

Figure 5.2: Sketch of the instruments on the 116.5 m met mast at Høvsøre

one of the vertices of the triangle points east and one of the bases of the triangle points in the North-South direction. The width of the mast decreases from 7.15 m at the ground to 1.10 m at 100.5 m. The sonic anemometers are installed on slender booms pointing North, whereas the cup anemometers and wind vanes are installed on the booms pointing South. In order to further avoid the influence of the wakes from the wind turbines and the met mast on lidar measurements, and inhomogeneities due to the sudden change of roughness (sea-land transition, see Fig. 5.1), only data periods with easterly winds (50°–150°) are analyzed. Table 5.1 provides some details of the experiment. It is to be noted that the sampling rate for the ZephIR lidar is low because seven measurement heights are scanned sequentially, and at each height three seconds v_r measurements at different θ are used to deduce the wind vector components. It is even more difficult to comprehend the sampling rate for the WindCube lidar, because one measurement of v_r is obtained in approximately 1.5 s, but the previous

three v_r measurements at three different θ are used to deduce the wind vector components. Strictly speaking the sampling rate of WindCube is thus not 1/1.5 s as stated in table 5.1.

Table 5.1: Instrument and Measurement Details of Study 1

	Reference Met Mast (Sonics)	CW Lidar, ZephIR	Pulsed lidar, WindCube
Location, UTM zone 32V WGS84 datum	447647 m, E and 6255435 m, N	447635 m, E and 6255467 m, N	447648 m, E and 6255439 m, N
Model/Version	Metek USA1 F2901A	v1	v1
Period of Measurement	Corresponding to the respective lidar	April–November 2009	January–April 2009
Sampling rate (Hz)	20	≈ 0.048	≈ 0.667
Averaging Period (min)	10		
Measurement Heights (m)	40, 60, 80 and 100		

5.1.3 Mean wind speed comparisons

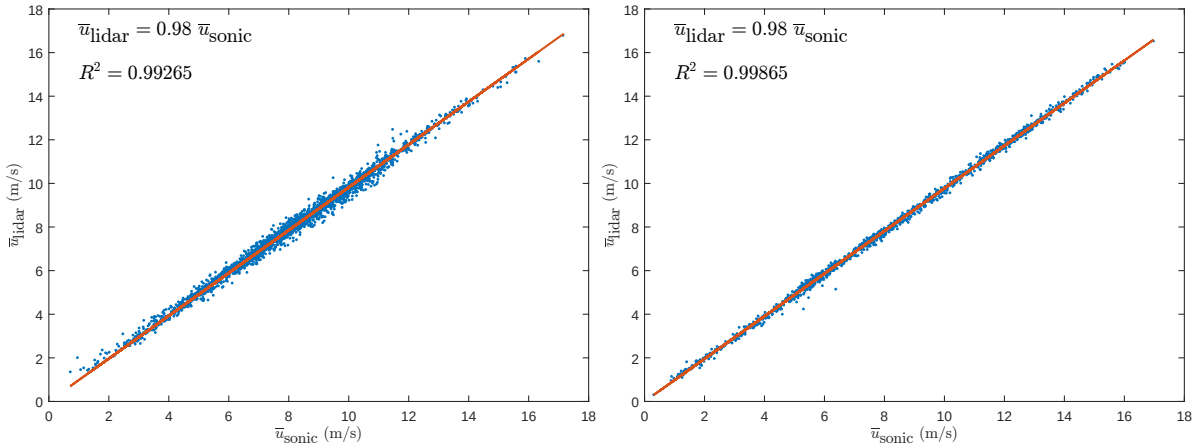

(a) CW lidar (b) Pulsed lidar

Figure 5.3: Comparing the mean wind speeds with a reference sonic anemometer at 100 m

Fig. 5.3 shows the comparison of the mean wind speeds estimated from lidar measurements and those estimated from a reference sonic at 100 m. For both types of lidars (CW and pulsed) the systematic error (characterized by the slope of the linear curve fit), and the uncertainty (characterized by the coefficient of determination R^2) are negligible. The closer the value of the slope to one, the smaller the systematic error, whereas the closer the value of R^2 to one, the smaller the uncertainty. Since for both types of lidars the systematic errors and uncertainties with respect to a reference sonic are $\approx$ 2% and $\lesssim$ 1% only, it gives enough confidence to proceed with the turbulence analysis.

5.1.4 Turbulence measurements

Owing to the availability of the high frequency (time series) data of v_r and $\mathbf{v}$ for both types of lidars and sonics respectively at different heights, variances of the u, v and w components

were estimated for several 10-min periods. The instrument and measurement details are given in table 5.1. The choice of the 10-min averaging period is driven by the common practice in the wind energy industry to use 10-min first- and second-order statistics of the wind vector components [IEC, 2005a]. Ideally the choice of an averaging period should be governed by the turbulent structure, i.e. the integral length/time scale of a turbulent time series [Lenschow et al., 1994](see section 1 and Eq. 1.4 for the definition of integral scales). However, in practice it is very difficult to implement such a technique. Therefore a compromise is usually made with regards to the choice of the averaging period, which is taken as 10-min in this experimental campaign.

From the lidar time series, the VAD method of post processing the data is implemented and the variances of the u, v and w components are estimated for every 10-min period. Simultaneously the corresponding statistics are also estimated using the sonics, which are used as reference measurements. For the respective measurement periods (depending on the type of lidar), several 10-min statistics were obtained representing different ensembles. In order to incorporate variation of the turbulent structure under different atmospheric stabilities, Obukhov length L (see Eq. 1.11) was estimated using the sonic measurements at 20 m (see Fig. 5.2). The ensembles were then classified based on L following the classification scheme in Sathe et al. [2011a]. For each stability condition, first, second (median) and third quartiles were computed. In the subsequent figures the first and the third quartiles represent the range of uncertainty of the respective turbulent statistic, whereas the second quartile denotes the median or approximately the ensemble average value. The choice of the second quartile is driven by the fact that the outliers do not influence ensemble statistics, which the mean value is normally influenced by (depending on the number of outliers). In the absence of too many outliers the mean and the median values are very close to each other.

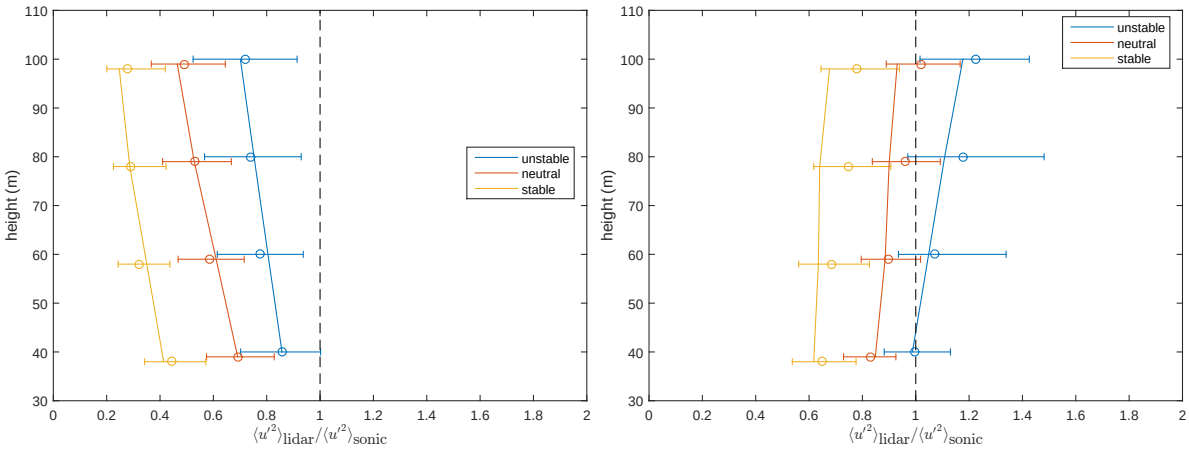

(a) CW lidar (b) Pulsed lidar

Figure 5.4: Ratio of the u variance estimated from the lidar measurements to that estimated by the sonics at different heights and atmospheric stabilities. The markers represent the measurements and the error bars represent the range determined by the first and the third quartiles. The solid lines represent model results. The plots are offset in heights for clarity.

Fig. 5.4 shows the ratio of $\langle u'^2\rangle$ estimated from lidar measurements to that estimated from the reference sonics for both types of lidars, i.e. a CW (Fig. 5.4a)and a pulsed lidar (Fig. 5.4b), at different heights and atmospheric stabilities. The measurements are shown by the markers and the error bars. The circles are the second quartiles and the error bars denote the range determined by the first and the third quartiles. Following the goal of this experimental campaign, a model was developed that attempted to understand the estimates

of the components of $\mathbf{R}$ by using the VAD method of processing the lidar data. Eq. (3.5) was used to compute the turbulence estimates from the model. The reference estimates from the model were computed using Eq. (1.7). Several inferences can be drawn from Fig. 5.4. First and foremost it is clear that for any type of lidar a ratio of one at all heights and atmospheric stability would indicate that the turbulence estimates from the lidar measurements are as good as those from the reference sonics. Unfortunately that is mostly not the case. The ratio of turbulence estimates not only deviate from the ideal one but they are also very different for different types of lidars and are significantly influenced by the turbulence structure in the atmosphere.

For a CW lidar the ratio decreases with height and with increasing stability, i.e. from unstable to stable conditions. As we understand from chapter 3, a lidar never receives backscatter from exactly a point, but from all over the physical space, and mainly along the line-of-sight. The significant contribution is received from a certain Rayleigh length l, which for a CW lidar is approximated as being proportional to the distance at which measurements are obtained d_f^2 [Sonnenschein and Horrigan, 1971](see also section 3.2.1.2). Clearly it shows that l increases quadratically with height, e.g. l at 80 m will be approximately four times that at 40 m above the ground. Simultaneously turbulence length scales do not increase quadratically with height, but approximately linearly [Peña et al., 2010]. As a consequence greater filtering of the turbulence signal occurs resulting in smaller estimations of turbulence statistics at higher heights than lower heights as compared to the reference sonics. Similarly turbulence scales are larger under unstable conditions than under stable conditions [Sathe et al., 2013], thereby resulting in smaller estimations of turbulence statistics under stable conditions than under stable conditions. Fortunately the modelled behaviour of the estimation of $\langle u'^2 \rangle$ from lidars and sonics correspond fairly well with the measurements, thereby increasing confidence in our understanding of turbulence estimations using the VAD method .

For a pulsed lidar the ratio increases with height but decreases with increasing stability. As opposed to a CW lidar, l remains constant with height. Considering that turbulence scales increase roughly linearly with height, it is obvious that larger estimates of turbulence statistics are observed at higher heights than at lower heights. The behaviour of the ratio under different atmospheric stabilities is similar to that observed for a CW lidar. However at some heights and atmospheric stabilities (mainly unstable conditions) the ratio is greater than one, which indicates that the estimates of $\langle u'^2 \rangle$ are larger than those estimated from the the reference sonics. This is explained by the cross contamination by the two-point correlations of the wind vector components as is manifested by the Einstein summation in Eq. (3.5). As for the CW lidar the model estimates correspond fairly well with the measurements.

Figures 5.5 and 5.6 show the ratio of $\langle v'^2 \rangle$ and $\langle w'^2 \rangle$ respectively estimated from lidar measurements to that estimated from the reference sonics for both types of lidars. As for $\langle u'^2 \rangle$ the behaviour of the ratio is similar for both types of lidars and under different atmospheric stabilities. There is however a significant difference in the magnitudes of the ratios between $\langle w'^2 \rangle$ and $\langle u'^2 \rangle$. Figure 5.6a shows that turbulence estimates from the lidar measurements could be as small as only 10 % of the reference estimates under stable conditions for a CW lidar. This difference can be explained by the fact that the turbulence scales are significantly larger for the u component than for the w component (see Fig. 7 in Sathe et al. [2013]). Consequently the turbulence estimates are filtered significantly for the w component. For the v component thre is not a significant difference in the magnitudes of the ratios, despite larger turbulence scales for the u component than for the v component as seen in Fig. 7 in Sathe et al. [2013]. On the contrary for $\langle v'^2 \rangle$, the ratios are slightly larger for both types of lidars than for $\langle u'^2 \rangle$. This could be due to the counteracting contribution of the cross-contamination as explained in section 3.1.1. The agreement between the model and measured estimates is slightly poorer than for $\langle u'^2 \rangle$. The following two reasons could contribute to this:

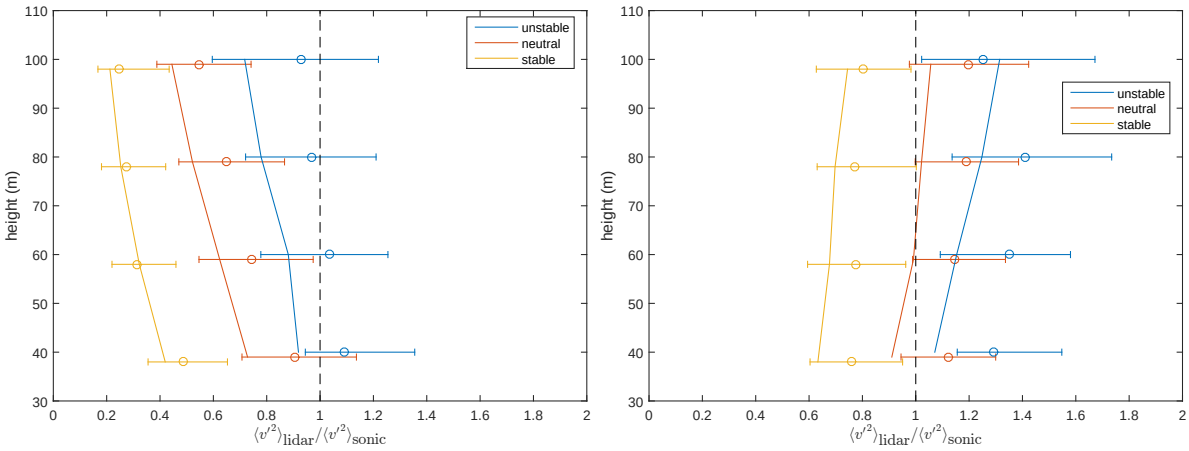

(a) CW lidar (b) Pulsed lidar

Figure 5.5: Same as Fig. 5.4, but for the v variance

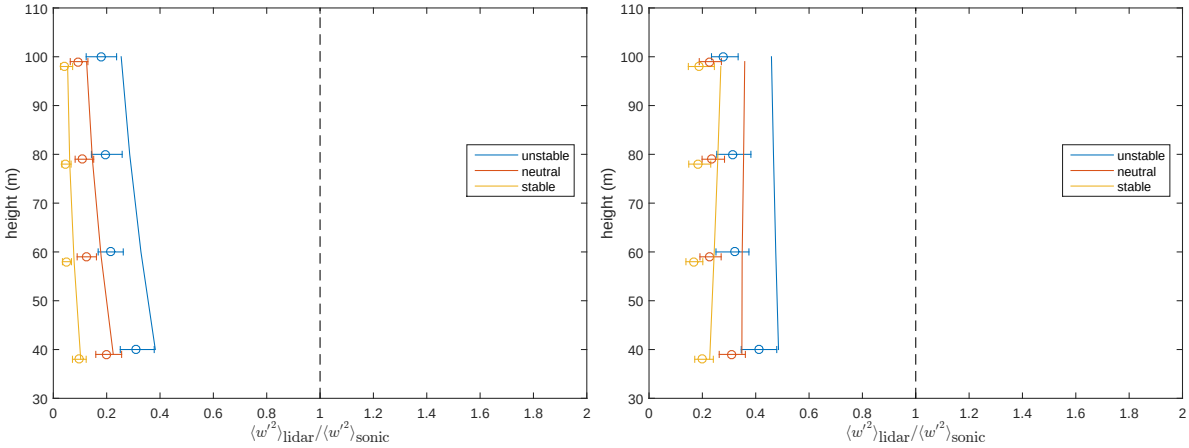

(a) CW lidar (b) Pulsed lidar

Figure 5.6: Same as Fig. 5.4, but for the w variance

- The attenuation in the w variances is quite large (up to 90%), as compared to the u and v variances (up to 70%). Thus a small difference in the model prediction and the measurement estimates could amplify the errors.
- For the CW lidar, when the low pass filter is used, a dependence on the mean wind speed is neglected. Segregating the model for different mean wind speeds will result in reducing the errors.

5.2 Study 2 – Høvsøre, Denmark

5.2.1 Introduction

The objective of this study was to understand the estimated turbulence spectra ($F_{ij}(k_1)$) from the time series of a pulsed lidar, where VAD method was used to post process the lidar data. Modelling of the estimated $F_{ij}(k_1)$ was carried out and comparisons were made with the measurements from a pulsed lidar. Modelled and measured $F_{ij}(k_1)$ were also compared with the same estimated from reference sonics at two heights. For details on the model the reader is referred to [Sathe and Mann, 2012]. Owing to the fact that R_{ij} is simply an integration of

$F_{ij}(k_1)$, this study complimented the study described in section 5.1 by further consolidating the understanding of the estimated R_{ij} from the lidar data using the VAD method.

5.2.2 Measurement details

The description of the site and the instrument details are exactly the same as those described in section 5.1.2 (refer to Figs. 5.1 and 5.2, and table 5.1). In this study only the pulsed lidar (WindCube) was used and investigations were performed at only two heights, i.e. 60 and 100 m. Furthermore the mean wind direction sector is chosen such that it is roughly aligned with nominal E-W beams, i.e. $130° \leq \Theta \leq 140°$. The choice of the mean wind direction sector was driven by the fact that the nominal North beam of the lidar was 45° with respect to the true North. The u and w component measurements are then deduced from the nominal E-W beams and the v component is deduced from the nominal N-S beams.

The other criteria for the selection of the data are neutral atmospheric stability and a mean wind speed of 9 m/s. This wind speed was chosen because the Mann [1994] model parameters were available at 9 m/s. Practically the selection of the data is carried out with a mean wind speed in the interval 8-10 m/s, which resulted in 79 and 58 10-min time series of the sonics and the lidar at 60 and 100 m, respectively. Atmospheric stability is characterized using Obukhov length L (see Eq. 1.11) where the sonic measurements at 20 m were used to estimate L.

5.2.3 Mean wind speed comparisons

Since the period of measurement and the instruments used are the same as that stated in section 5.1.2, Fig. 5.3b is also representative for this study. Since only the mean wind speeds between 8 and 10 m/s are considered in this study, the reader should zoom in the respective wind speed interval to check the comparisons in Fig. 5.3b. Considering that the systematic error and the uncertainty in the mean wind speed estimation within the chosen interval is similar to that for the whole range of wind speeds, it gives enough confidence to proceed with the turbulence analysis.

5.2.4 Turbulence measurements

The high frequency lidar data of v_r are post processed using the VAD method (see section 3.1) to deduce the wind vector components. The turbulence spectrum for each component is estimated using standard Fourier transformations [Pope, 2000]. Simultaneously the same are also estimated using the sonic measurements. The corresponding modelled estimations are carried out as described in Sathe and Mann [2012]. In the subsequent figures the spectra of the respective wind vector components are denoted as $F_u(k_1)$ for the u $(i = 1,\ j = 1)$ component, $F_v(k_1)$ for the v $(i = 2,\ j = 2)$ component, and $F_w(k_1)$ for the w $(i = 3,\ j = 3)$ component.

Fig. 5.7 shows the comparison of the estimated u spectra from the pulsed lidar (black) and reference sonics (gray) at 60 and 100 m. The measurements indicate that the spectrum measured by the lidar deviates significantly from the standard surface-layer spectrum as the turbulence scales decrease approximately from $k_1 > 0.005$ m^{-1}. Approximately in the inertial sub-range, where the sonic spectra scales with $k_1^{-5/3}$, there is an almost complete attenuation of the turbulence signal, and hence a rapid decrease in the spectral energy. This observation has a striking resemblance with that of Canadillas et al. [2010], where an independent measurement under neutral conditions in the German North Sea showed an increase in the spectral energy above $k_1 > 0.005$ m^{-1} and subsequent rapid attenuation. One of the reasons for this redistribution of the spectral energy is the contribution of the two-point correlations

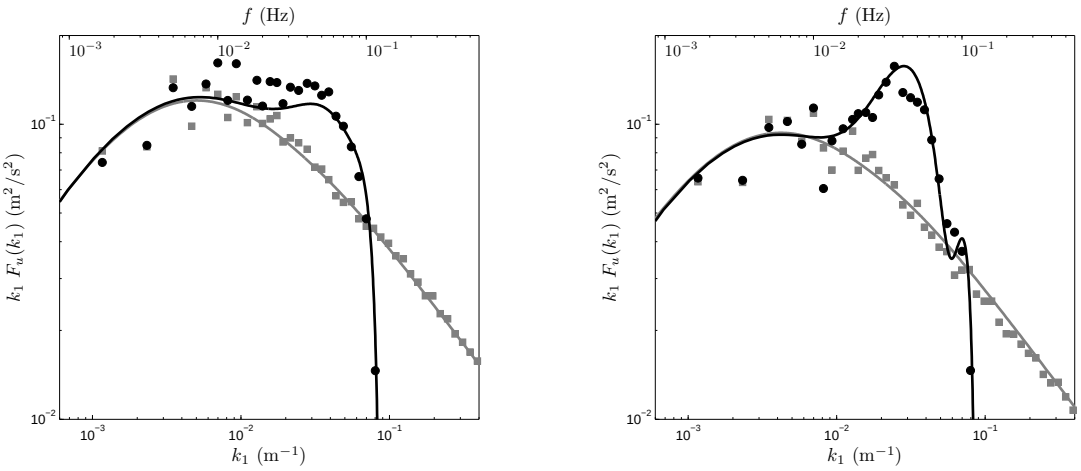

(a) 60 m (b) 100 m

Figure 5.7: Comparison of the estimated u spectrum from the pulsed lidar (black) and reference sonics (gray) at 60 m and 100 m. The markers indicate measurements and the continuous line indicates the model.

between different components of the velocity field. At very low wavenumbers ($< 0.005\ \mathrm{m}^{-1}$), the spectral energy measured by the lidar is approximately the same as that measured by the sonics. This is because very large turbulence eddies are associated with very low wavenumbers that cause the volume measurement from the lidar to behave essentially like a point measurement.

At both heights, the model agrees very well with the measurements at almost all wavenumbers. The point-like behavior of the lidar at very low wavenumbers, and redistribution of the spectral energy beyond $k_1 > 0.005\ \mathrm{m}^{-1}$, is captured fairly well. However, there are stark differences in the distribution of the spectral energy at 60 and 100 m. This is because of the beam interference phenomenon that occurs for certain separation distances at 100 m and is related to the assumption of Taylor's hypothesis [Sathe and Mann, 2012].

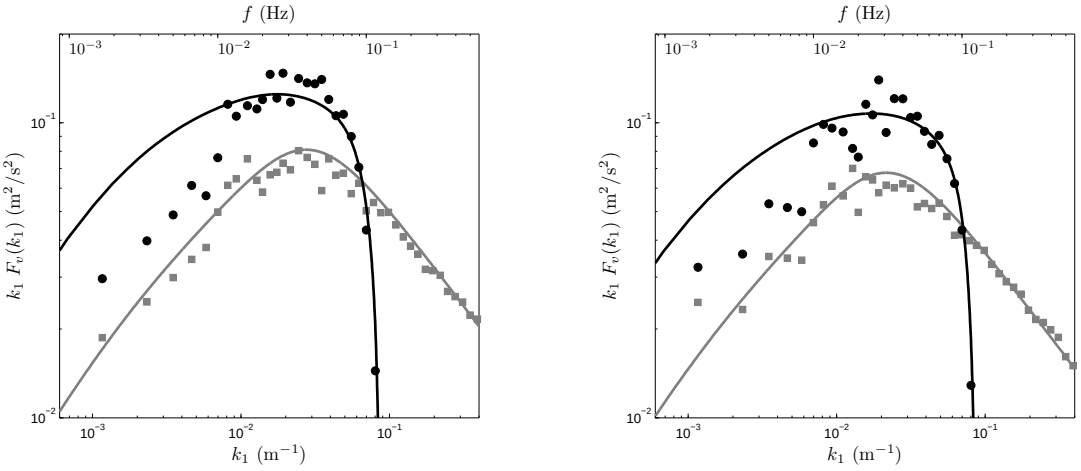

(a) 60 m (b) 100 m

Figure 5.8: Same as Fig. 5.7 but for the v component

Fig. 5.7 shows the comparison of the estimated v spectra from the pulsed lidar (black) and

reference sonics (gray) at 60 and 100 m. As observed for the u component, the v spectrum measured by the lidar deviates significantly from that of the refrence sonic spectrum. However, at very low wavenumbers, there is an offset in the spectral energy between the lidar and the sonic. The behavior in the inertial sub-range is the same as that for the u component, where a rapid attenuation in the spectral energy is observed. The model agrees fairly well with the measurements at 60 and 100 m, except at very low wavenumbers (< 0.005 m^{-1}), where the model over estimates the spectral energy. One striking feature of this comparison is that as opposed to the u component, no beam interference phenomenon at 100 m is observed. This is because only those beams that are perpendicular to the mean wind direction (i.e. N-S beams) are used to deduce the v component. Thus, even though Taylor's hypothesis is assumed, the beams never interfere with each other at any separation distance. Sathe and Mann [2012] provides a detailed explanation for the over estimation of the spectral energy at very low wavenumbers.

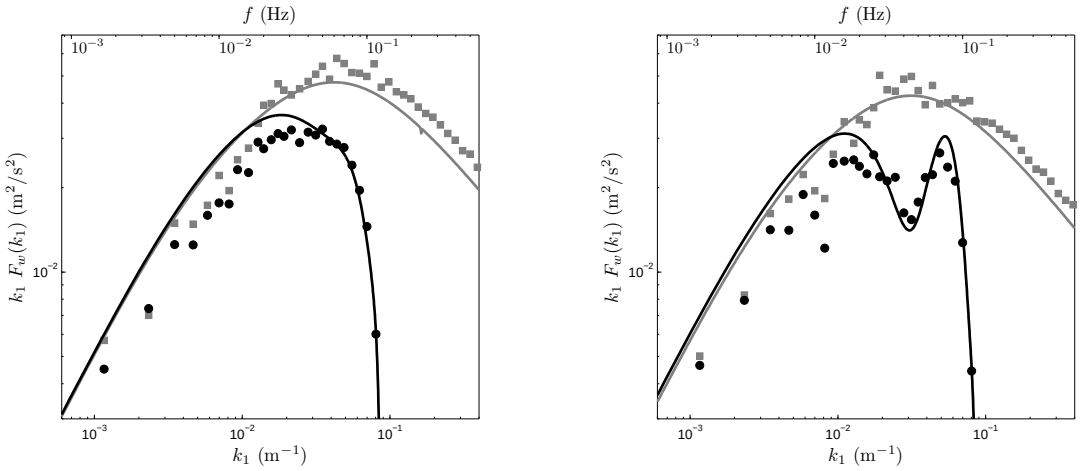

(a) 60 m (b) 100 m

Figure 5.9: Same as Fig. 5.7 but for the w component

Fig. 5.7 shows the comparison of the estimated w spectra from the pulsed lidar (black) and reference sonics (gray) at 60 and 100 m. Similar to the u spectra, beam interference at 100 m is observed because of the assumption of Taylor's hypothesis, and because the same beams are used to estimate the w component as those used for the u component. The measured lidar spectrum agrees well with the model at both heights, especially at high wavenumbers. As observed for the u component, at 100 m the effect of unusual covariances on the spectral energies is also noted. At very low wavenumbers, there is a slight offset between the model and measurements. This offset could be because of the slight deviation in the modeled and measured sonic spectrum. The model also shows that at very low wavenumbers, because of very large turbulence eddies, the volume measurement from the lidar behaves similar to a point measurement.

5.3 Study 3 – Høvsøre, Denmark

5.3.1 Introduction

The objective of this study was to demonstrate an alternative scanning method, the so-called six-beam scanning, where the estimation of the components of $\mathbf{R}$ (see Eq. 1.2) is carried out using $\langle v_r'^2 \rangle$ instead of the VAD method of post processing the lidar data. The

motivation behind this study was to reduce the systematic errors that are otherwise observed to a very large extent in the VAD method of post processing the lidar data (see section 3.1.1 for theoretical summary and sections 5.1 and 5.2 for experimental evidence). For details of the six-beam method the reader is referred to [Sathe et al., 2015].

5.3.2 Measurement details

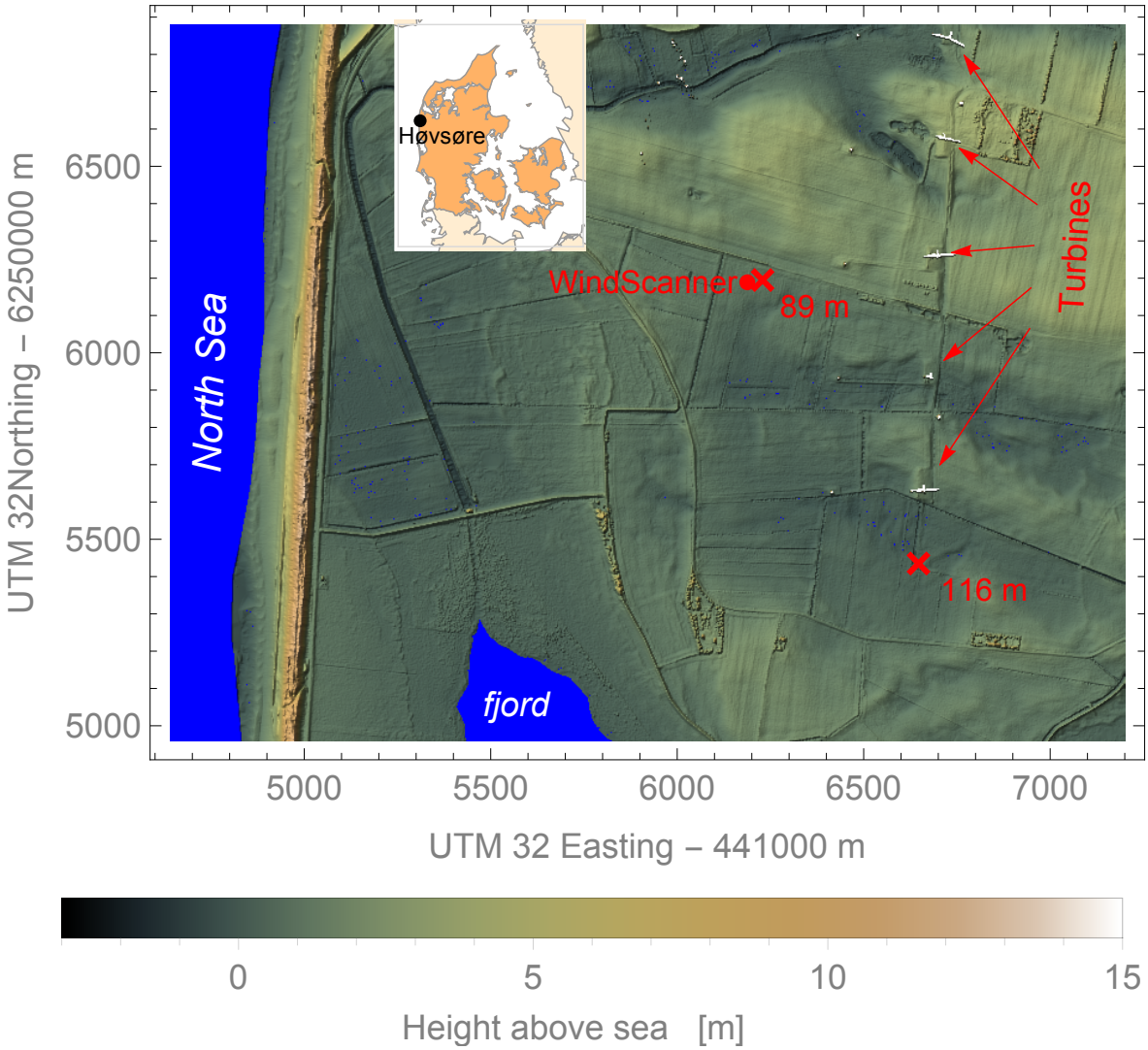

Figure 5.10: Location of the test site at Høvsøre, Denmark

The details of the measurement site are exactly the same as described in section 5.1.2. Because the scanning strategy in this study is different from that used in the commercial WindCube lidar, a modified version of the lidar known as a WindScanner was used that had the same pulsed lidar technology at the base. The WindScanner is based on the pulsed lidar Windcube 200 from Leosphere and has a dual-axis mirror based steerable scanner head designed by DTU Wind Energy and IPU. The WindScanner is intended for radial velocity measurements from the range of distances between 50 and 6000 m. The current maximum measurement rate is 10 Hz. The maximum number of simultaneous radial velocities acquired at any rate along each line-of-sight is 500. The WindScanner can emit either 400 or 200 ns laser pulses, which are streamed with two corresponding pulse repetition frequencies of

10 and 20 kHz respectively. The energy content of 400 ns laser pulses is 100 μJ, while the energy content of the 200 ns laser pulses is half of this value. The scanner head has two rotational degrees of freedom and can rotate around the azimuth and elevation axes, thus it directs the laser pulses into the atmosphere at any combination of azimuth and elevation. The maximum scanner head rotation speed is 50 $^\circ s^{-1}$, while the maximum acceleration is 100 $^\circ s^{-2}$. The scanner head can rotate around both axes from 0 to 360 °, and the rotation can be endless. The pointing accuracy of the WindScanner is 0.05°. The WindScanner is operated via a remote "master computer" through a UDP/IP and TCP/IP network using the remote sensing communication protocol (RSComPro) [Vasiljevic, 2014].

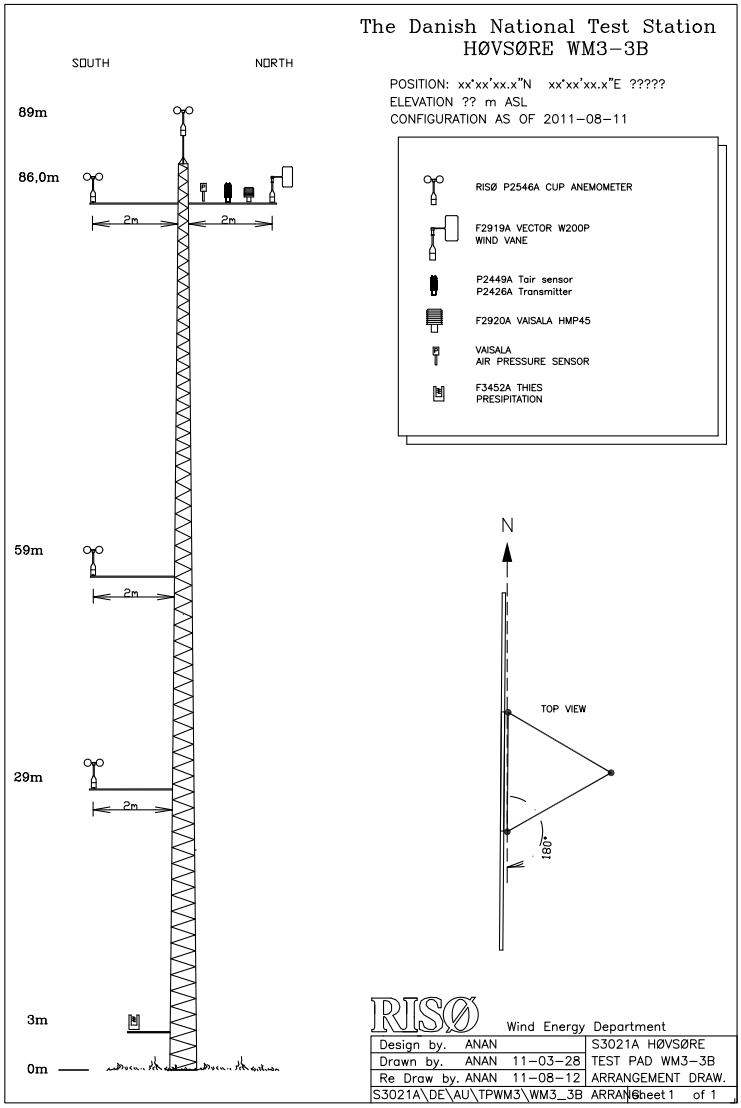

Figure 5.11: Sketch of the instruments on the 89 m met mast at Høvsøre, Denmark

Figure 5.10 shows the location of the WindScanner and the 89 m met mast, which has a cup anemometer at the top and a wind vane at 86 m in the North direction (see Fig. 5.11). Since the wind turbines are to the east of the WindScanner and the met mast, the measurements

only from the western sector (225–315 °) are used. Owing to the sudden change in the surface roughness from sea to land in the western sector, we expect the turbulence structure to be influenced by the development of the internal boundary layer, particularly under different atmospheric stabilities. This presented a challenge in selecting a reference met mast. The two met masts are separated by a distance of about 850 m, which is of the same order as the distance between the WindScanner and the 116.5 m met mast. Initial comparisons of the 30-min mean wind speeds and turbulence statistics between the reference instruments on the two met masts indicated presence of horizontal inhomogeneity. Therefore the 89 m met mast was chosen as the reference, which is separated by a distance of approximately 41 m only from the WindScanner. One of the disadvantages of using a cup anemometer is that the vertical variances cannot be estimated. The u and v component variances were estimated using the time series observations of the horizontal wind speed and the wind direction. Atmospheric stability was however characterized by an 80 m Sonic on the 116.5 m met mast, and it was assumed that L is not significantly influenced by horizontal inhomogeneity.

Table 5.2: Instrument and Measurement Details of Study 3

	Reference Met Mast 1		Reference Met Mast 2	Pulsed Lidar
	Cup Anemometer	Wind Vane	Sonics (only for estimating L)	WindScanner
Location, UTM zone 32V WGS84 datum	447229 m, E and 6256195 m, N		447647 m, E and 6255435 m, N	447188 m, E and 6256189 m, N
Model/Version	Risø P2564A cup	F2919A Vector W200P	Metek USA1 F2901A	Windcube 200
Period of Measurement	July 1 – July 28, 2013			
Sampling rate (Hz)	10	10	20	≈ 0.0667
Averaging Period (min)	30			
Measurement Height (m)	89	86	80	89

Since the diameter of the lidar scanning circle was much smaller than the distance between the met masts, significant influence on the flow homogeneity in the horizontal direction around the scanning circle was also not expected, which is one of the key assumptions of the six-beam method. The measurements were compared to the reference cup anemometer placed at 89 m on the top of a met mast placed near the WindScanner. The duration of the full cycle of the six-beam measurements from the WindScanner was about 15 s. The turbulence statistics were estimated over an averaging period of 30-min in oder to reduce the random errors. After filtering for data availability within each 30-min period, where only those periods were chosen with 95 % data, the number of 30 min periods reduced to 625. Finally filtering for wind directions to avoid wakes from the wind turbines and the met mast rendered 401 30-min periods. Table 5.2 provides details of the instruments used.

5.3.3 Mean wind speed comparisons

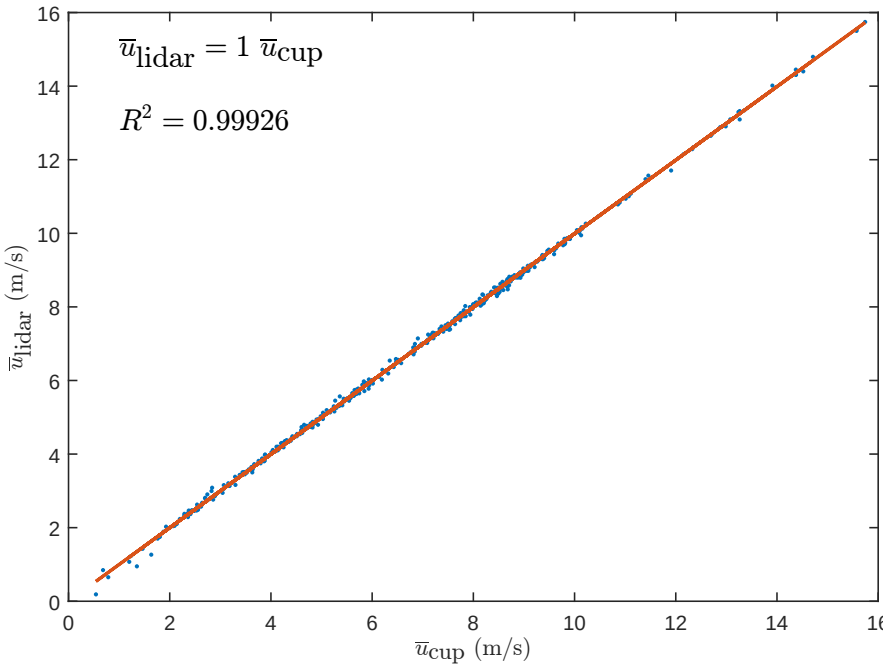

Figure 5.12: Scatter plot of the 30-min mean wind speeds estimated by the WindScanner and the reference cup anemometer at 89 m

Fig. 5.12 shows the comparison of the mean wind speeds estimated the WindScanner and the reference cup anemometer at 89 m. It is observed that the systematic error (characterized by the slope of the linear curve fit), and the uncertainty (characterized by the coefficient of determination R^2) are negligible. The closer the value of the slope to one, the smaller the systematic error, whereas the closer the value of R^2 to one, the smaller the uncertainty. Since the systematic errors and uncertainties with respect to a reference sonic are $\lesssim 0.1\%$ only, it gives enough confidence to proceed with the turbulence analysis.

5.3.4 Turbulence measurements

From section 3.2.2, we understand that the optimum configuration of the six-beam scanning is as given in table 3.1. For each 30-min period $\overline{v_r'^2}$ was estimated using the time series of v_r. Using Eq. 3.17 the components of $\mathbf{R}$ are estimated subsequently. In order to assess the performance of the method, the estimated statistics were compared with those estimated from the VAD method of post processing the lidar data. Finally the estimated $\overline{u'^2}$ and $\overline{v'^2}$ from both methods (six-beam and VAD) were compared with those estimated from the cup anemometer and wind vane data under different atmospheric stabilities (see table 5.2).

Figure 5.13 shows the comparison of the turbulence statistics derived from the WindScanner measurements using the six-beam and the VAD methods and those obtained from the cup anemometer under unstable conditions. It is clear that the six-beam method measures more turbulence, about 19 % for $\overline{u'^2}$ and 3 % for $\overline{v'^2}$ than the VAD method, where the orthogonal least-squares regression is used to fit the cup anemometer measurements. The scatter using both methods is comparable to each other, but there is a slightly more scatter using the six-beam method for $\overline{v'^2}$.

Figure 5.14 shows the same as Fig. 5.13 but under neutral conditions. As for the unstable conditions, the six-beam method measures more turbulence, about 18 % for $\overline{u'^2}$ and 10 % for

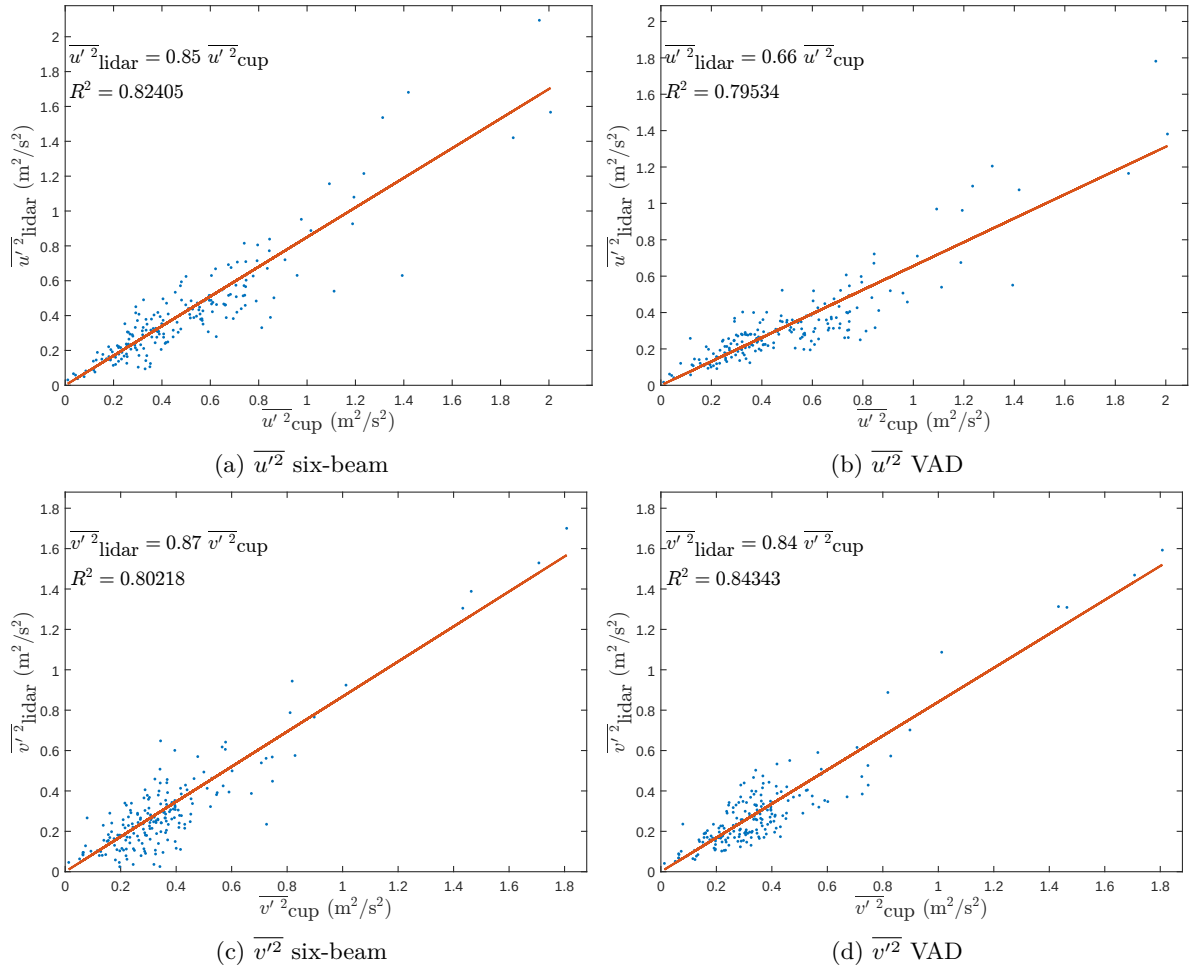

(a) $\overline{u'^2}$ six-beam (b) $\overline{u'^2}$ VAD

(c) $\overline{v'^2}$ six-beam (d) $\overline{v'^2}$ VAD

Figure 5.13: Comparison of the the turbulence statistics under unstable conditions between the WindScanner and the cup anemometer using two methods

$\overline{v'^2}$ than the VAD method. The scatter using both methods is comparable to each other, with the six-beam method giving a slightly reduced scatter than the VAD method.

Figure 5.15 shows the same as Fig. 5.13 but under stable conditions. As for the unstable conditions, the six-beam method measures more turbulence, about 19 % for $\overline{u'^2}$ and 4 % for $\overline{v'^2}$ than the VAD method. The scatter using both methods is comparable to each other, but there is a slightly more scatter using the six-beam method for $\overline{u'^2}$.

Thus under all stabilities the six-beam method is closer to the turbulence measurements carried out using the reference cup anemometer. There is however some probe volume averaging using both methods, but is significantly larger for the VAD method. The probe volume averaging can be observed clearly by comparing the radial velocity spectra, which can be observed in Fig. 6 in Mann et al. [2009], and Fig. 4 in Sjöholm et al. [2009]. From Figs. 5.13–5.15 it is clear that using both methods the WindScanner measures more turbulence under stable conditions than under unstable and neutral conditions. This may be contrary to our intuitive understanding, because usually the turbulence scales are much larger under unstable conditions than under stable conditions [Sathe et al., 2013]. These results are also contrary to what has been observed in study 1 (see Fig. 5.4–5.6) at the same site. However, it is to be noted that in study 1 only those lidar measurements were used when the wind was blowing from the eastern direction, whereas in this study only those measurements were used when the wind was blowing from the western direction (see section 5.3.2). As described in Sect. 5.3.2,

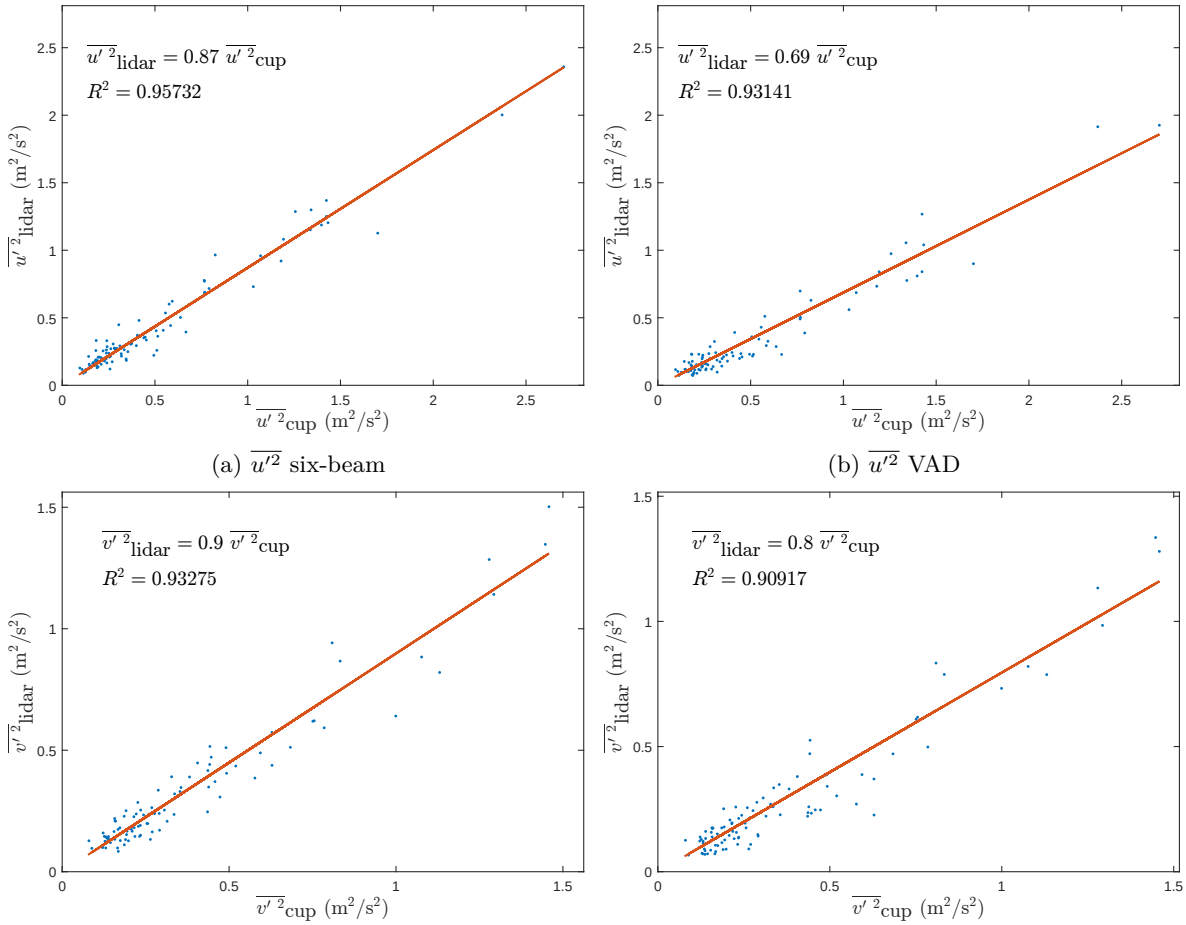

(a) $\overline{u'^2}$ six-beam (b) $\overline{u'^2}$ VAD

(c) $\overline{v'^2}$ six-beam (d) $\overline{v'^2}$ VAD

Figure 5.14: Same as in Fig. 5.13 but under neutral conditions

in the western sector there is a sudden change of roughness due to the transition from sea to land. As a consequence there is a development of the internal boundary layer (IBL). Also the growth of the IBL depends on atmospheric stability, where under unstable conditions the growth will be faster than under stable conditions. Panofsky and Dutton [1984] state that the growth of the height of the boundary layer is proportional to the drag coefficient $u_*/\overline{u}$. And it is well known that the drag coefficient is larger for unstable stratification. Consequently the turbulence scales within the IBL will be smaller as compared to those outside of it. It is then interesting to check whether the WindScanner measures more within the IBL under unstable conditions as compared to the stable conditions.

Figure 5.16 shows the u and v spectra derived from high-frequency cup anemometer measurements under different stability conditions. If we define the characteristic length scale $\mathscr{L}$ as the length scale corresponding to the maximum spectral energy, it is then clear that the peak of the v spectra is shifted to the right for unstable conditions as compared to the stable conditions. It is not that clear for the u spectra, however the shift of scales to larger wavenumbers under unstable conditions can still be observed. Thus $\mathscr{L}$ appears smaller under unstable conditions than under stable conditions for the measurements from the western sector used in this work. There is thus more probe volume averaging under unstable conditions than under stable conditions. Hence the WindScanner attenuates the turbulence measurements more under unstable conditions than under stable conditions.

Another interesting observation is that using the VAD method the WindScanner does not

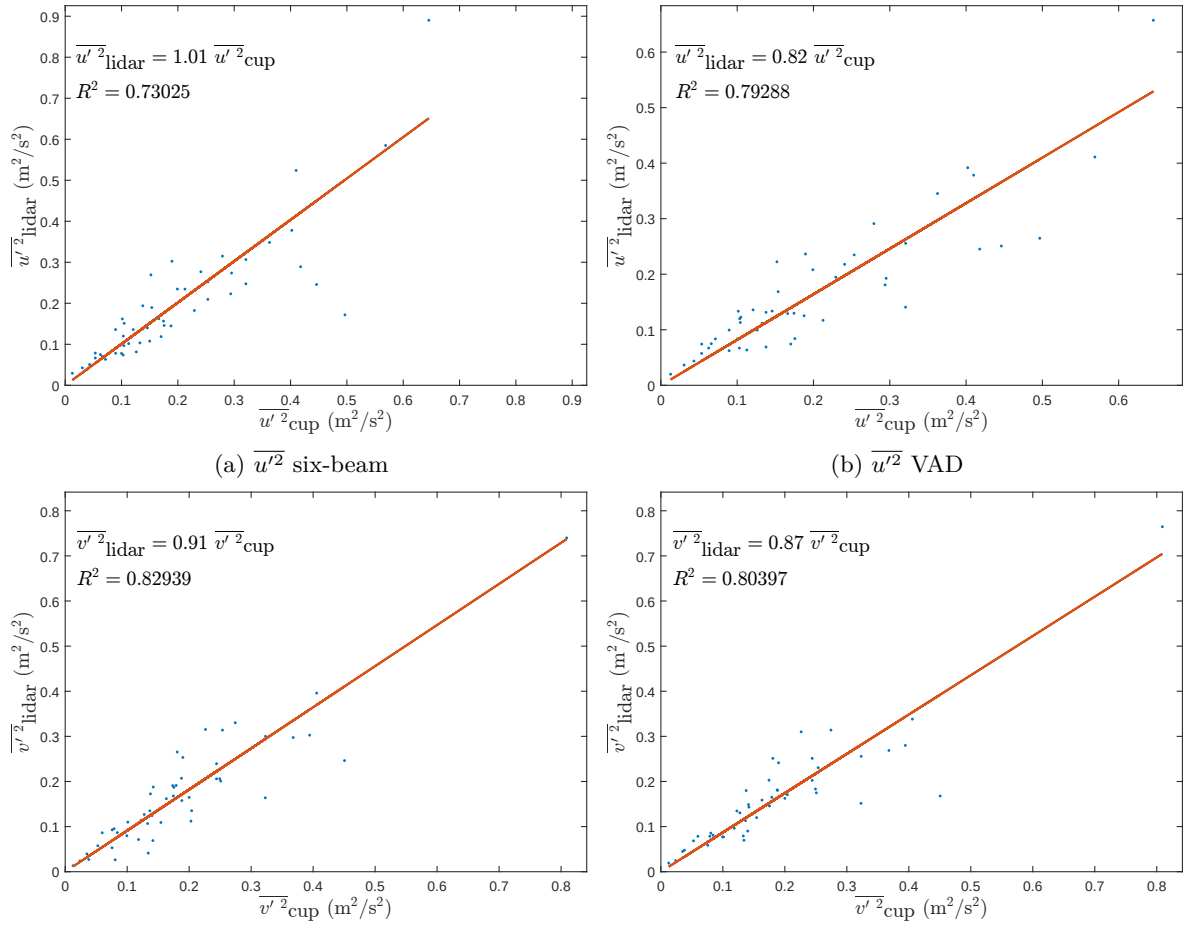

(a) $\overline{u'^2}$ six-beam (b) $\overline{u'^2}$ VAD

(c) $\overline{v'^2}$ six-beam (d) $\overline{v'^2}$ VAD

Figure 5.15: Same as in Fig. 5.13 but under stable conditions

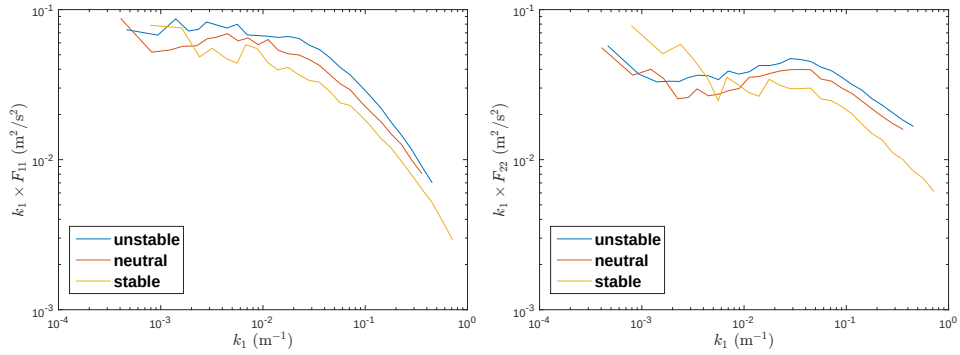

(a) u-spectra (b) v-spectra

Figure 5.16: Comparison of the u- and v-spectra derived from high-frequency cup anemometer and wind vane measurements under different stability conditions

measure more turbulence than the reference cup anemometer under any stability condition. This does not agree with that observed in study 1 (see Figs. 5.4b and 5.5b), even though the same basic pulsed commercial lidar technology was also used in that study. It is likely due to the fact that in study 1 only four beams were used as opposed to six beams in this study, the temporal resolution of the scans was different and ϕ was 30° compared to 45° used in this

work. Therefore the turbulence statistics are not directly comparable with those obtained in study 1 even though the same basic commercial lidar was used. Due to the application of the least squares technique on the v_r measurements in this work, there is significant volume averaging around the scanning circle, which is also observed in study 1 for a continuous-wave lidar (see Fig. 5.4a, 5.5a and 5.6a).

5.4 Study 4 – Kassel, Germany

5.4.1 Introduction

This case study compares turbulence measurements of the horizontal wind speed cup anemometry to turbulence measurements by a pulsed DBS lidar in complex terrain. It aims to provide the practical user with a showcase of how turbulence estimations from a commonly used profiling lidar can deviate from traditional cup anemometry in complex forested terrain.

5.4.2 Measurement details

The measurements were performed at the complex terrain test site at Rödeser Berg Berg about 30 km north-west of Kassel in central Germany. The lidar was placed within a distance of 5 m to the 200 m tall reference mast located on a small clearing on the ridge of a Hill (see Fig. 5.17a). The wider surroundings of the test site are characterized by a hilly landscape with agricultural land use, patches of forests and small towns. For more details on the measurement site the reader is referred to Klaas et al. [2015]. The mast is equipped with opposing boom pairs with a length of 5.40 m (diameter 50 mm). The effects due to flow distortion on the mean wind speed are approximately 0.5% according to IEC [2005b] for the anemometer being directly upwind of the mast. For all other wind directions in the 180° upwind sector the influence of the mast on the mean wind speed can be assumed to be smaller. The turbulence comparison was performed using cup anemometer data from the 180° upstream sectors of the two opposite booms. Although these numbers only apply for the mean horizontal wind speed, they indicate that great care was taken to reduce any effects on the measurements due to the mounting of the cup anemometers.

Details of the lidar and the reference sensors used in the comparisons can be found in Table 5.3. All statistics are computed for 10-min periods. Wind speeds below 4 m/s are excluded from the analysis as they are usually below a typical turbine cut-in speed and thus are of less importance for the operation of wind turbines. Moreover, the reference cup anemometers are only calibrated for wind speeds above 4 m/s. The statistics of the lidar measurements were taken as provided by the internal processing software of the lidar.

5.4.3 Mean wind speed comparisons

In general, the agreement in the measured horizontal wind speed measured by the cup anemometer and the lidar are very good (see Fig. 5.18). Due to the orographic complexity of the surrounding terrain a directional dependent bias in the horizontal wind speed can be expected [Klaas et al., 2015]. However, the most frequent sectors during the measurement campaign were not strongly affected by the terrain effects. Also, some of the directional effects probably cancel out.

5.4.4 Turbulence measurements

Figure 5.19 shows the ratio of $\langle u'^2 \rangle$ estimated from the lidar and the cup anemometer measurements at different heights. There is a clear deviation between the lidar and the reference

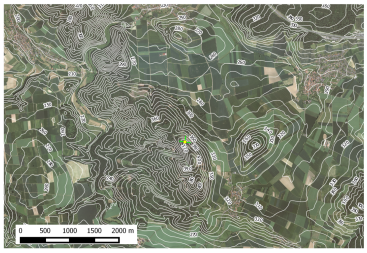

(a)

(b)

Figure 5.17: 5.17a Satellite image and orography of the measurement site at RÃűdeser Berg; the yellow dot indicates the location of the measurement mast and the LiDARs. 5.17b photography of the measurement mast at RÃűdeser Berg.

instrument at all investigated heights. At all heights, ratio of greater than one is observed, which indicates an overestimation of $\langle u'^2 \rangle$ by the lidar measurements as compared to the reference instruments. Even the lower quartile lies significantly above the reference. Notably, at Rödeser Berg there is no clear pattern with height as e.g. in Høvsøre, Denmark (see section 5.1). The ratio $\langle u'^2 \rangle_{\text{lidar}} / \langle u'^2 \rangle_{\text{cup}}$ is lowest at the 120 m measurement height, whereas similar levels can be observed at 60 m and at the top of the mast. This result also suggests that the increase of the turbulence scales (compare section 5.1) cannot fully explain measurement behaviour of the lidar. An explanation could potentially lie in the complex (forest, clearing and orography) surroundings of the terrain at Rödeser Berg which will probably have a stronger influence on the turbulence structure at lower heights. It is also interesting to note that the interquartile range of the ratio of $\langle u'^2 \rangle_{\text{lidar}} / \langle u'^2 \rangle_{\text{cup}}$ increases with height.

Table 5.3: Details of the instrumentation at Rödeser Berg, study 4

	Mast	Lidar
Evaluated measurement heights	60 m, 120 m, 191 m, 200 m	
Location, UTM zone 32U WGS84 datum	513595 m, E and 5690187 m, N	within 5 m from the mast
Instrumentation at 60 m	Thies first class advanced cup anemometer, Fully heated Vaisala cup anemometer	
Instrumentation at 120 m	Thies first class advanced cup anemometer	
Instrumentation at 191 m	Thies first class advanced cup anemometer	
Instrumentation at 200 m	Thies first class advanced cup anemometer	
Period of Measurement	September 17 – October 30, 2013	
Sampling rate (Hz)	≈ 1	1
Time per scan cycle (s)		5
Averaging Period (min)	10	

In an applied wind energy context it is probably very interesting to estimate turbulence intensity I, as it is widely used in certification and site assessment. Following the definition of I in Eq. 1.3 and from Fig. 5.18, it is clear that the major source of variation in I arises due to the estimated standard deviation σ_u. From fig. 5.20 it is clear that the lidar measurement at Rödeser Berg provides a (very) conservative estimate of the average I for the measurement campaign. To put this into context of the current normative framework for the design and certification of wind turbines [IEC, 2005a], a comparison with the turbulence classes for the certification of wind turbines is useful. The mean relative deviation between the lidar and the reference at Rödeser Berg is larger than the difference between e.g. I_{ref} in turbulence class A and B (or B and C). However, it should be kept in mind that in a suitability analysis I should be evaluated in dependence of wind speed. Also, the wind speed dependent standard deviation of I will be important for the calculation of the representative or characteristic turbulence intensity. However, the data set is too small to provide the results of a full suitability analysis. The results in this comparison provide a useful tendency on how a lidar of this specific type can be expected to perform in a complex forested site. However, these results should not be generalized to other sites or types of lidars.

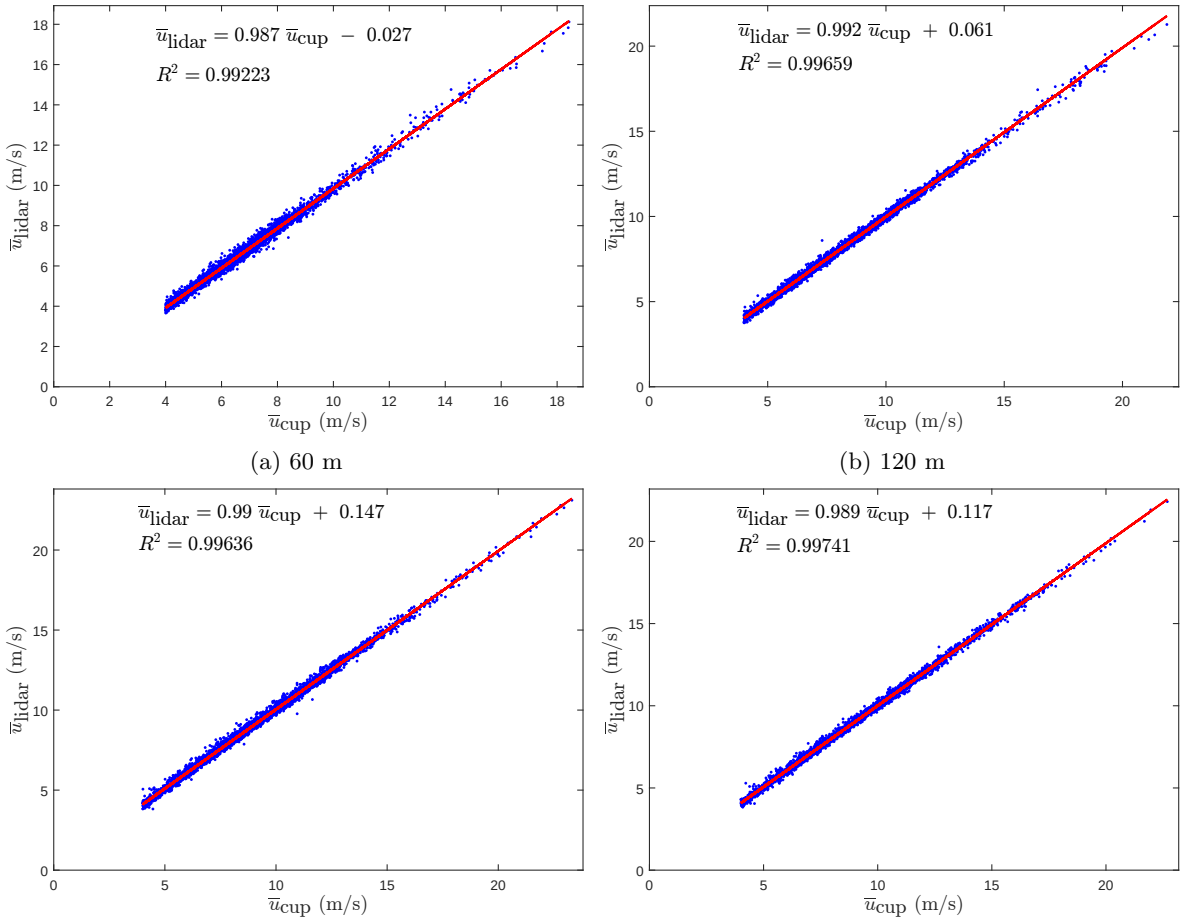

(a) 60 m (b) 120 m

(c) 191 m (d) 200 m

Figure 5.18: Scatter plot of the 10-min mean wind speeds estimated by the lidar and the reference cup anemometer measurements at different heights. The solid line indicates the ordinary linear regression. R^2 denotes the coefficient of determination.

5.5 Study 5 – Norway

5.5.1 Introduction

The reported study was part of a larger test campaign, with the purpose of assessing the uncertainty of lidars in complex terrain. A WindCube V1 was used to measure wind speed and turbulence against a reference 50 m mast on a complex site. This campaign itself was designed to assess the uncertainty of lidars in complex terrain, in order to evaluate its feasibility, including their operational performance under harsh conditions. For more details and other results, see Vogstad et al. [2013].

5.5.2 Measurement details

Figure 5.21 shows the measurement site and table 5.4 provides the details of the measuring instruments used. The campaign lasted for approximately two months. Methods for correcting for flow inhomogeneity using VAD scans have been described in Pitter et al. [2012]. Using WindSim software, a CFD flow model was constructed to describe the flow field in the testing area. The terrain model was based on 5 meter contour lines and the roughness model was created using land use dataset from the Norwegian Mapping Authority. The site is not

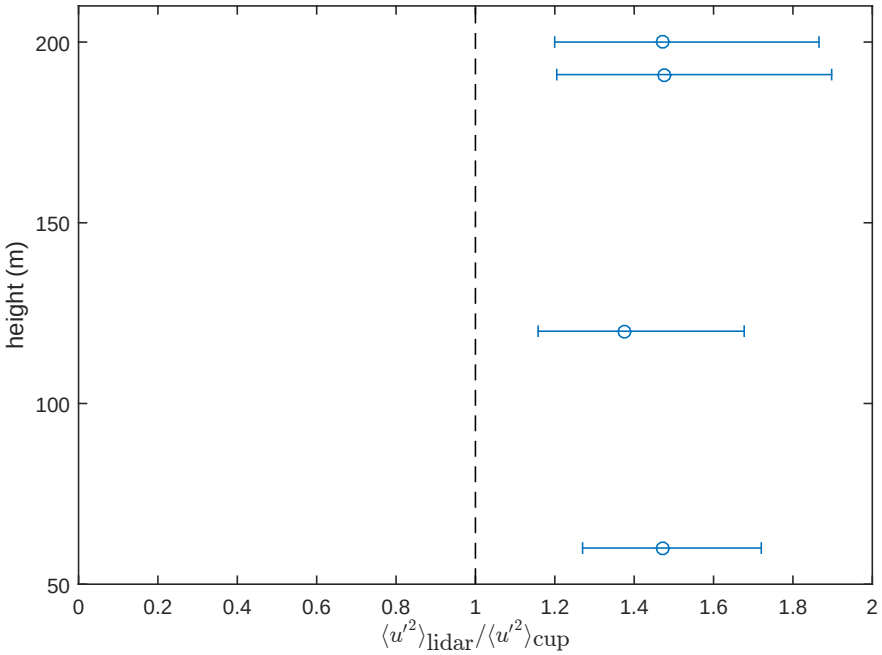

Figure 5.19: Ratio of $\langle u'^2 \rangle$ estimated from the lidar and the cup anemometer measurements at different heights. Circles indicate median ratios. The error bars denote the interquartile range.

Table 5.4: Details of the instrumentation, study 5

	Mast	Lidar
Evaluated measurement heights	50 m	
Location, UTM zone 32V WGS84 datum	325048 m, E and 6502682 m, N	next to the mast
Instrumentation	Thies first class advanced cup anemometer	WindCube v1
Period of Measurement	December 02, 2011 – January 16, 2012	
Uncertainty	2.5%	-
Averaging Period (min)	10	
Filtering	$>$ 4 m/s	availability $\geq$ 80%, $>$ 4 m/s, outliers

forested. Neutral flow stratification was assumed for all wind directions. For more details on the flow model, see Vogstad et al. [2013].

Figure5.22 shows the resulting CFD correction factors applied onto the WindCube time series. Although the site is highly complex, the correction factors at the measured location were on average 1-3% during the measurement period. The sectors are divided into 10° bins, and different lines represent the correction factors from no smoothing at all up to a smoothing of four neighbouring sectors (red line). The correction factors are only developed for the 10-min mean wind speed and not for turbulence statistics.

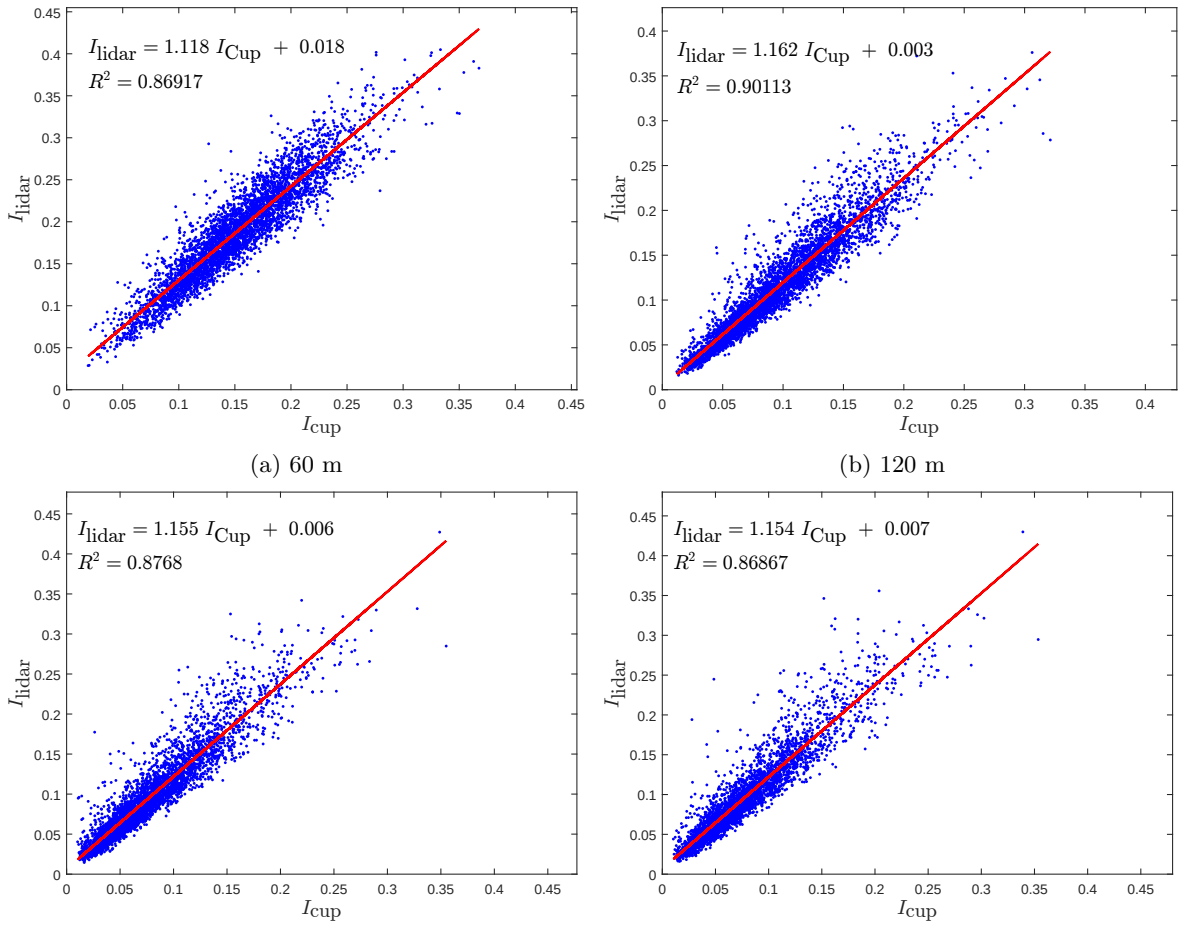

Figure 5.20: Scatter plot of the 10-min turbulent intensity of the wind speeds estimated by the lidar and the reference cup anemometer measurements at different heights. The solid line indicates the ordinary linear regression. R^2 denotes the coefficient of determination.

5.5.3 Mean wind speed comparisons

The comparison of mast measurements versus lidar measurements in Fig. 5.23 shows good correspondence with mast data. The availability during the test was was about 90%. The availability does not include downtime due to power supply problems or other non-related lidar problems. It is rather the availability from useful measurements, when the lidar is in operation. While Fig. 5.23a shows the regression plot, Fig. 5.23b shows the bin-wise correspondence of lidar and wind speed data by 1 m/s intervals. The horisontal lines show the 2.5% standard uncertainty of the anemometers. The solid and dotted lines show deviations with and without the CFD correction. For the CFD corrected lidar data, all measurements are within the standard uncertainty of the mast measurements. From the same measurement period, we will measure turbulence in the following section.

5.5.4 Turbulence measurements

Figure 5.24 compares the estimated turbulence intensity from the WindCube and the reference cup anemometer measurements. The correspondence is not as good as with wind speeds, but is good enough to be considered useful. The mean error (bias) of the turbulence measurement was 8.6%.

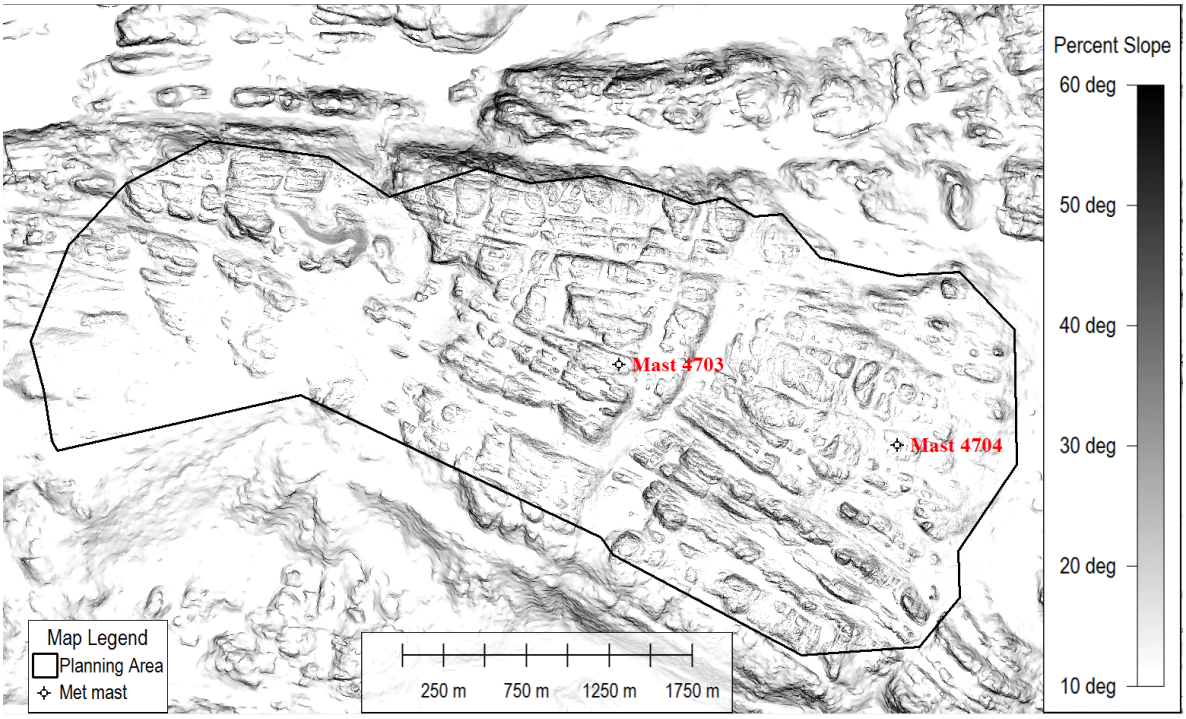

Figure 5.21: Site overview, test campaign in complex terrain

Table 5.5: Summary results Lidars test measurement campaign, study 5

Against a reference cup anemometer at 50 m				
	Slope	Offset	R^2	Mean Error
Mean Wind Speed (not CFD corrected)	0.98	0.15	0.99	-0.74
Mean Wind Speed (CFD corrected)	0.99	0.25	0.99	1.47
Mean Wind Direction	1.02	-3.88	1.00	
Turbulence Intensity (I)	1.005	0.008	0.93	

Table 5.5 summarizes the comparison of the WindCube lidar against the reference cup anemometer on the 50 m mast. This field measurement showed that a lidar can give useful turbulence measurement results. Compared against masts, where the horizontal wind components are measured fairly accurately, the turbulence measurements of vertical components has been shown to be less accurate [Sathe et al., 2011b].

While lidars do not have the precision of cup and sonic anemometry, they may still provide a good alternative for wind resource assessment in the field. It is however to be noted that in order to make a concrete statement as regards lidar uncertainty, it is essential to know beforehand the same in reference instruments. On many occasions (especially for sonic anemometers), such information is not available. For wind resource assessment, masts are located up to 2 km from potential turbine positions. There is currently no good method for modeling turbulence in complex terrain. There are mainly three ways of assessing turbulence

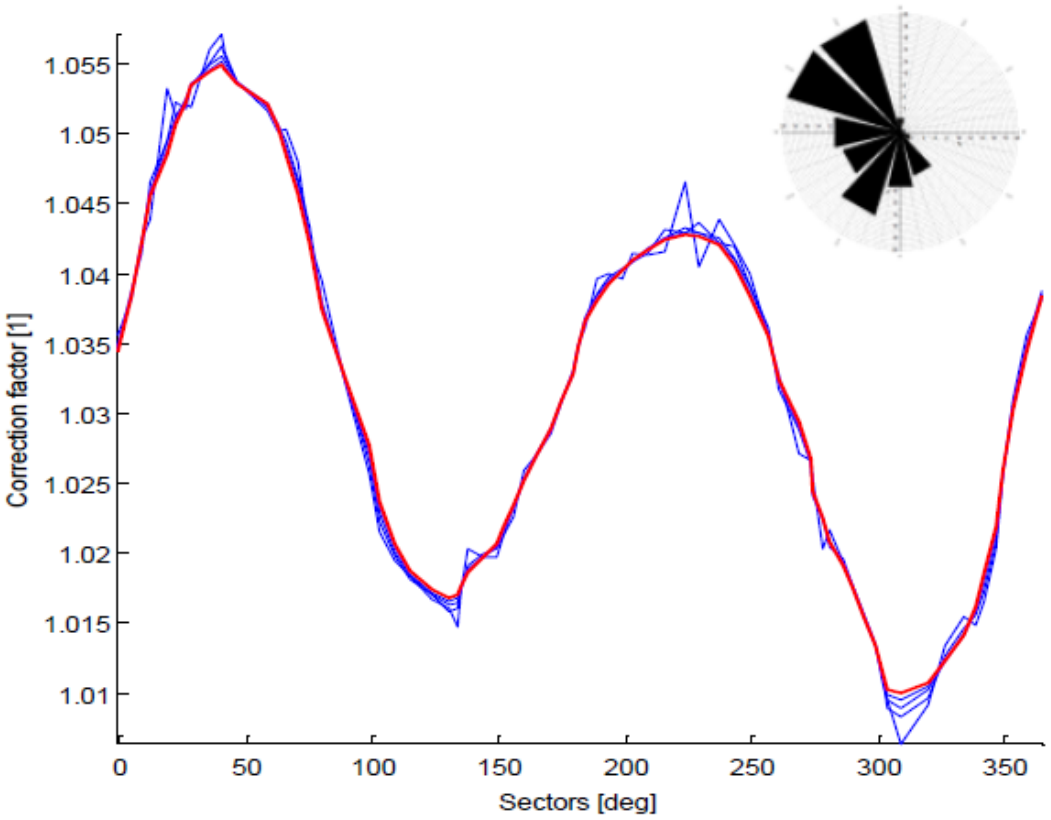

Figure 5.22: Correction factors applied to the Lidar measurements to correct for flow inhomogeneity

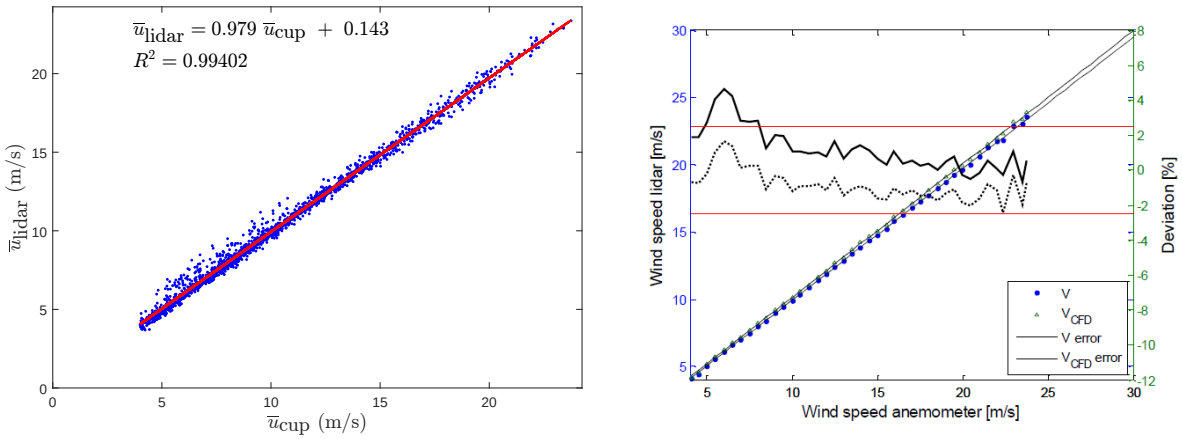

(a) (b)

Figure 5.23: Scatter plot of the 10-min mean wind speeds estimated by the lidar and the reference cup anemometer measurements at 50 m. The solid line indicates the ordinary linear regression. R^2 denotes the coefficient of determination.

in practical wind resource assessments.

- Turbulence is extrapolated in the horizontal up to 2 km from mast to potential turbine locations by scaling with the modelled wind speed. This approach is clearly highly uncertain.

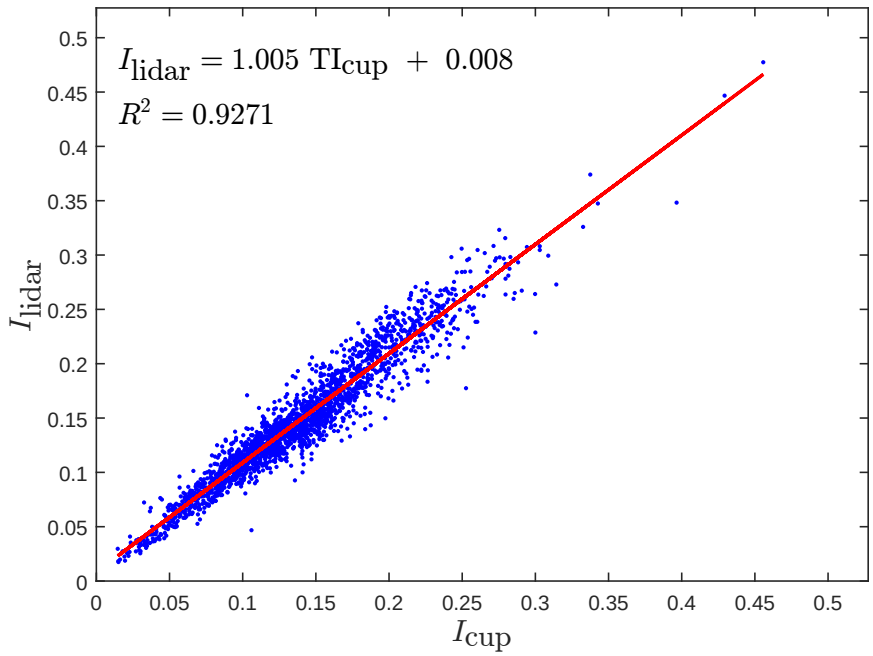

Figure 5.24: Comparing the estimated turbulence intensity from the WindCube and the reference cup anemometer measurements.

- Turbulence models such as the implementation of the Mann [1994] model in Wasp Engineering are used in semi-complex terrain, but are not valid for complex terrain.
- Turbulence estimates from CFD models can be used, but the Bolund experiment showed that the model errors of turbulence estimates were on average 35% [Bechmann et al., 2011].

Currently there are no good or satisfactory methods of estimating turbulence for practical wind resource assessment in complex terrain. The relevant uncertainties are currently in the range of 35%, while lidars can due to their mobility be positioned to measure turbulence closer to relevant turbine positions. In our test, the uncertainty (mean error) was estimated to 8.6%, while Baker [2012] shows similar results of uncertainty (15%) for turbulence measurements.

5.6 Study 6 – Høvsøre, Denmark

5.6.1 Introduction

The goal of this study was to demonstrate the spatial averaging effects on the estimated turbulence statistics using CW coherent lidar measurements. For more details and other results, see Sjöholm et al. [2009].

5.6.2 Measurement details

The description of the site and the instrument details on the meteorological mast are exactly the same as those described in section 5.1.2 (refer to Figs. 5.1 and 5.2, and table 5.1). In this study only the CW lidar (ZephIR) was used, and investigation was performed at 80 m height. Although the exact duration of the experiment is unknown, the results presented are between 6$^{\text{th}}$ and 8$^{\text{th}}$ December 2007. The lidar was mounted on a fixture that manually

could be rotated and tilted, and was given an elevation of 34° and a direction of 26° East of North, allowing the beam to be focused at a distance of 138 m in the vicinity of the sonic anemometer. After the alignment the lidar was fixed in its given position for the whole measurement campaign. The clocks for the data collecting computers were synchronized and all the times in this study are local times at the measurement site (Central European Time).

5.6.3 Mean wind speed comparisons

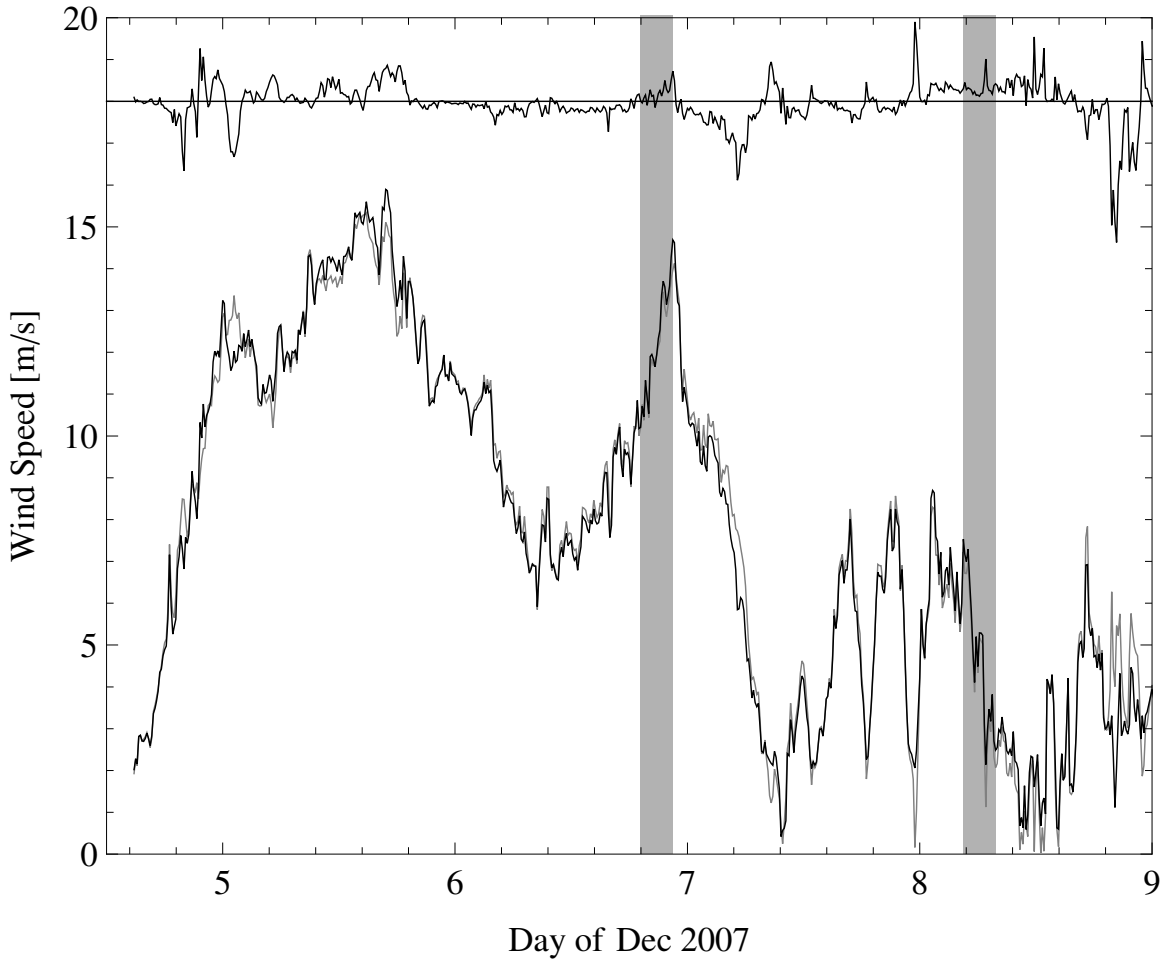

Figure 5.25: Comparison of the 10-min mean time series of the radial velocity measured by the lidar and the projected sonic wind velocity. The upper plot shows the difference between the lidar and sonic radial velocities with a shifted zero offset for clarity.

Figure 5.25 shows the time series of the estimated 10-min mean radial velocities from lidar and sonic measurements. The upper plot in Fig. 5.25 shows the difference between the lidar and sonic radial velocities, but with the zero offset shifted for more clarity. The gray patches in the figure denote the period for which the turbulence statistics are estimated. It is clear that the deviations of the estimated 10-min mean speed between the lidar and the sonic are quite small. Therefore it gives enough confidence to proceed with the turbulence analysis.

5.6.4 Turbulence measurements

Figure 5.26 compares a 60 s time series sampled at 20 Hz by a CW lidar and a sonic anemometer on the morning of 8^{th} December 2007. It is interesting to note that despite the same

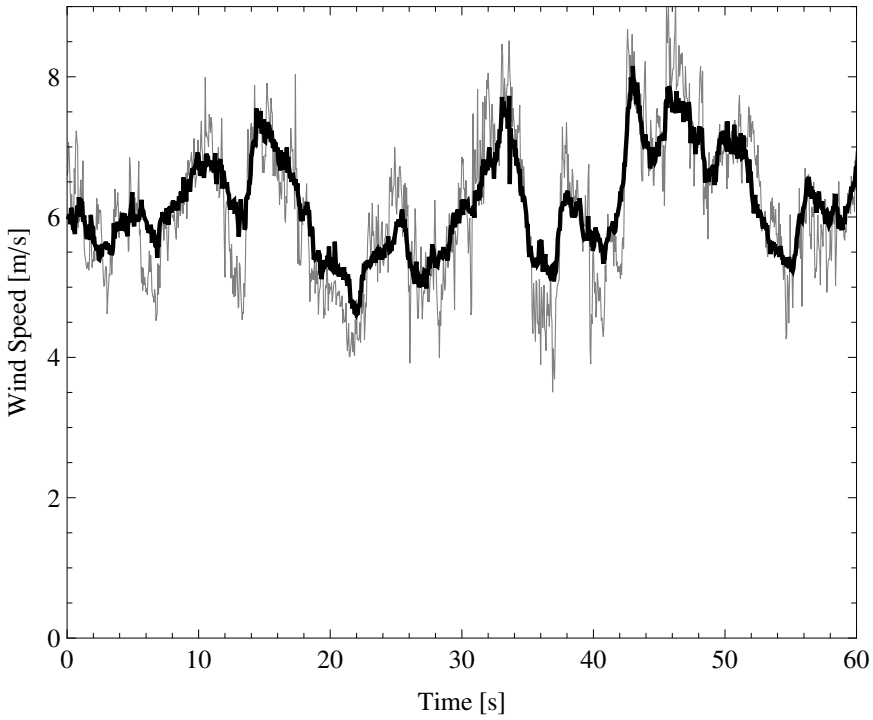

Figure 5.26: Comparing the 60 s time series sampled at 20 Hz by a CW lidar and a sonic anemometer

sampling frequencies of the two instruments, the lidar filters out smaller turbulence scales due to its large probe volume, whereas the sonic captures the variation at small scales fairly well. Such small-scale filtering effect is clearly evident in the radial velocity spectra plots.

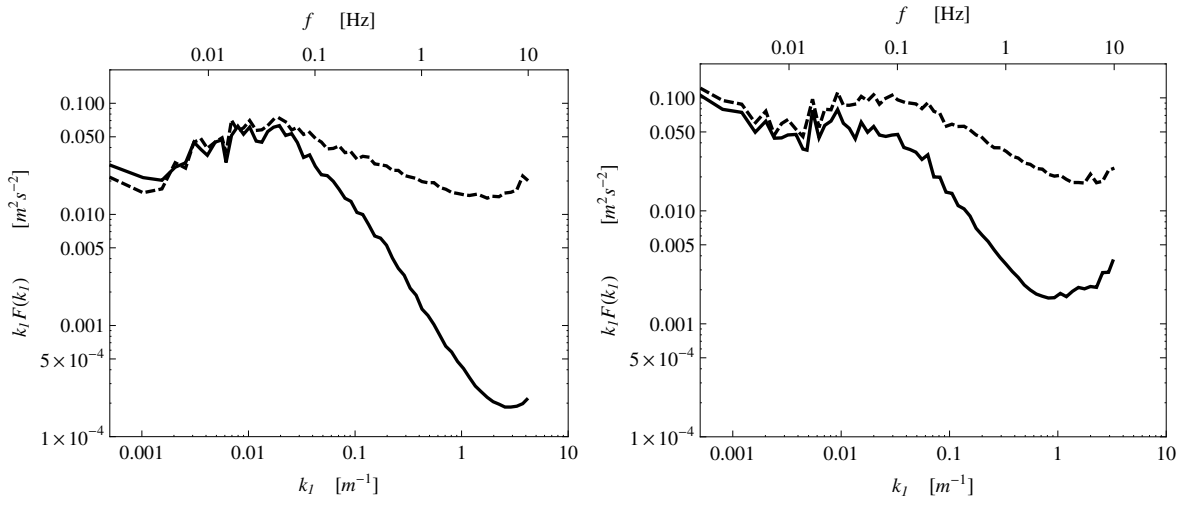

Figure 5.27: Comparison of the estimated radial velocity spectra from the lidar and sonic measurements for two different periods. The solid line denotes lidar, whereas the dotted line denotes sonic measurements.

Figure 5.27 shows the comparison of the estimated radial velocity spectra from 3.5 hours of lidar and sonic measurements for two different periods. For both periods, the filtering

effect of the small-scale turbulence is clearly evident, where there is a significant drop in the spectral energy beyond a certain wavenumber for the spectrum estimated from the lidar measurements.

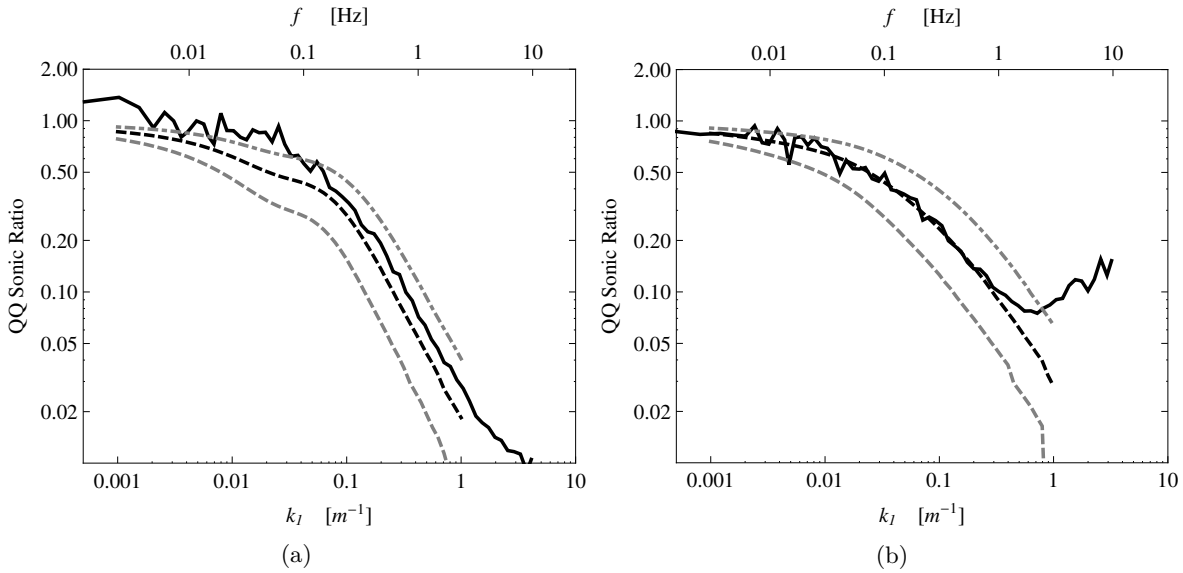

Figure 5.28: Ratio of the estimated radial velocity spectrum from the lidar and sonic measurements. The dotted lines denote model calculations.

In order to theoretically understand the spatial averaging effects, the radial velocity spectrum for the lidar was estimated theoretically using Eq. (3.10). The filter function $\varphi(s)$ was assumed to be Lorentzian [Sonnenschein and Horrigan, 1971], and the calculation of $F_{\mathbf{v}}(k_1)$ was carried out using the Mann [1994] model. The model parameters $\alpha\varepsilon^{2/3}$, $\mathscr{L}$, and an anisotropic parameter necessary to calculate $F_{\mathbf{v}}(k_1)$ were estimated using the high frequency sonic anemometer measurements for the two different periods. In order to emphasize the importance of the filter length scale of the lidar, model calculations were also performed using half (gray dash-dotted line) and twice the length scale (gray dashed line) for both periods. It is clear from the figures that when an appropriate filter length scale is chosen, the model calculations agree very well with those estimated from the measurements, thus giving a good confidence in our understanding of the spatial averaging effects.

5.7 Study 7 – Høvsøre, Denmark

5.7.1 Introduction

The goal of this study was to understand the spatial averaging effects on the estimated turbulence statistics using pulsed lidar measurements. For more details and other results, see Mann et al. [2009]. This objective of this study is very similar to that in study 6, where instead of a pulsed lidar, a CW lidar is used.

5.7.2 Measurement details

The description of the site and the instrument details on the meteorological mast are exactly the same as those described in section 5.1.2 (refer to Figs. 5.1 and 5.2, and table 5.1). In this study three pulsed lidars (WindCube) were used, and investigation was performed at 80 m height. The first lidar was pointing vertically and the other two lidars were at a zenith angle

$\phi = 56°$ from the vertical. The duration of the experiment was about one week in December 2007, where five different periods were analyzed. In this report, results from only one such period are provided.

5.7.3 Mean wind speed comparisons

No comparisons of the mean wind speed were carried out in this study.

5.7.4 Turbulence measurements

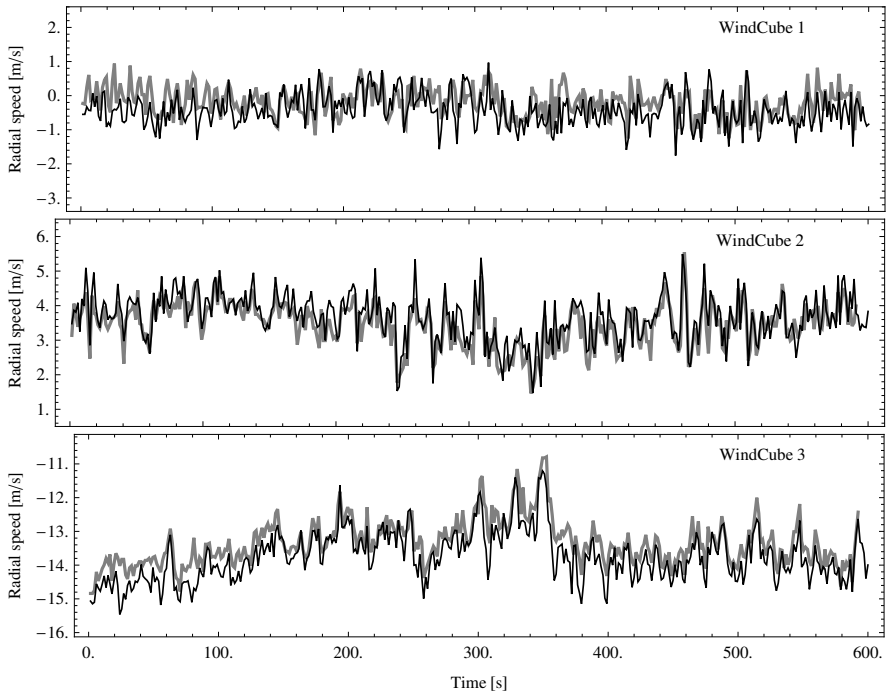

Figure 5.29: Comparing the 10-min time series of the radial velocities sampled at 1.5 Hz by three pulsed lidars and a sonic anemometer. The thin black color denotes sonic measurements, whereas the thick gray lines are lidar measurements.

Figure 5.29 compares a 10-min time series of the radial velocities sampled at 1.5 Hz by three pulsed lidars and a sonic anemometer. The measurements from the three axes of the sonic anemometer are projected on to the respective beam coordinate system of the lidars. The 20 Hz sonic time series is also block averaged to 1.5 Hz that approximately resembles the sampling frequency of the three lidars. For all lidars the radial speeds follow the projected sonic radial speeds quite well. Although not as evident as for a CW lidar (see Fig. 5.26), the filtering of smaller turbulence scales can also be seen for lidar measurements.

In order to understand the spatial averaging effects, the radial velocity spectra for all three lidars were calculated theoretically using Eq. (3.10). The filter function $\varphi(s)$ was assumed to be triangular, and the calculation of $F_{\mathbf{v}}(k_1)$ was carried out using the Mann [1994] model. The model parameters $\alpha\varepsilon^{2/3}$, $\mathscr{L}$, and an anisotropic parameter necessary to calculate $F_{\mathbf{v}}(k_1)$ were estimated using the high frequency sonic anemometer measurements for the measurement period. Figure 5.30 shows the comparison between the model calculations and the measurements. As for the CW lidar there is a clear drop in the spectral energies beyond a certain wavenumber due to the probe volume of the lidars. However the magnitude of av-

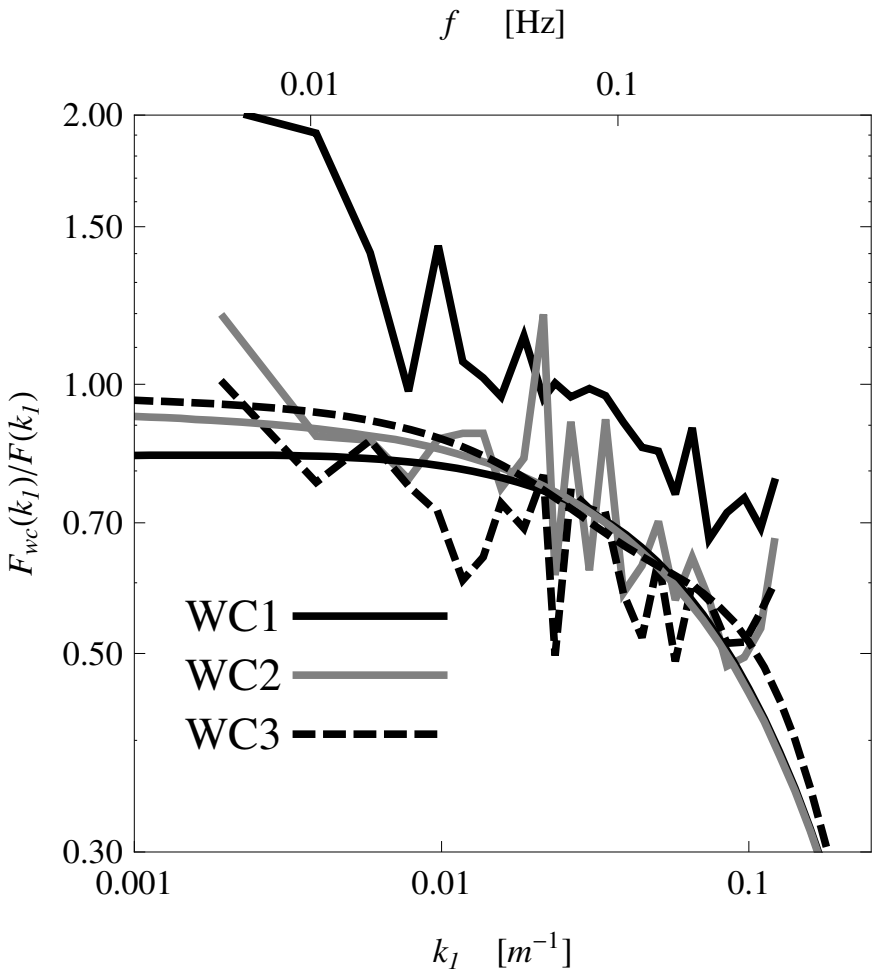

Figure 5.30: Ratio of the estimated radial velocity spectrum from the lidar and sonic measurements. The dotted lines denote model calculations.

eraging is not as significant as for the CW lidar (see Fig. 5.28a). This depends on the height of measurement and the turbulence structure in the atmosphere (see study 1).

It is also interesting to note in Fig. 5.30 that the ratio of the estimated radial velocity spectrum is larger than one for WindCube 1, especially at low frequencies. At first it was thought that this could be a result of poor pointing accuracy (i.e. the beam not being vertical). However, subsequent checks negated this hypothesis, and an inherent noise source in WindCube 1 is attributed for the spectral ratios greater than one.

5.8 Study 8 – Høvsøre and North Sea, Denmark

5.8.1 Introduction

The goal of this study was to investigate methods to estimate the momentum flux i.e. $\langle u'w' \rangle$ using the measurements from both a CW and a pulsed lidar at two different sites. For a CW lidar, a novel method was developed to recover the probe volume averaging effects of the small-scale turbulence by the use of averaged Doppler spectra. For mathematical details, see Mann et al. [2010].

5.8.2 Measurement details

Experiments were performed at two different sites, one onshore and one offshore.

5.8.2.1 Site 1

The description of the first site and the instrument details on the meteorological mast are exactly the same as those described in section 5.1.2 (refer to Figs. 5.1 and 5.2, and table 5.1). Two lidars, a CW and a pulsed were used in the experiment. For the pulsed lidars, comparisons of the estimated statistics are also made with a sonic anemometer on a light tower at 160 m height. Table 5.6 provides details of the lidars and the light tower.

Table 5.6: Instrument and Measurement Details of Lidars at Site 1, Study 8

	Light Tower	CW Lidar	Pulsed Lidar
Location, UTM zone 32V WGS84 datum	447698 m, E and 6255830 m, N	≈ 20 m North of the 116.5 m met mast	
Model/Version	Metek	ZephIR, v1	WindCube, v1
Period of Measurement	December 2006 – February 2007		
Sampling rate (Hz)	≈ 1	≈ 1.5	
Averaging Period (min)	30		
Measurement Heights (m)	160	40, 80, 100	40, 60, 160

The statistics are estimated when no rain fell. The chosen wind direction for the analysis was between 200° and 330°. Furthermore the pulsed lidar data was filtered according to the carrier-to-noise (CNR) ratio, such that for heights below 100m only the data with CNR>-10 dB were chosen, whereas for the 160 m height only the data with CNR>-15 dB were chosen.

5.8.2.2 Site 2

The experiment at site 2 was performed at an offshore wind farm in the North Sea, known as the Horns Rev. Figure 5.31 shows the location of the site. A CW lidar (ZephIR) was installed on the platform of the wind farm at about 20 m above mean sea level (amsl). The platform is located in the North Sea at approximately 12 km from the west coast of Denmark. Table 5.7 gives details of the experiment and the instruments.

Table 5.7: Instrument and Measurement Details of Site 2, Study 8

	Reference Met Mast, M2 (Cups)	CW Lidar, ZephIR
Location, UTM zone 32V WGS84 datum	423444 m, E and 6153203 m, N	≈ 5 km east of met mast
Model/Version	Risø	v1
Period of Measurement	Corresponding to the respective lidar	May–October 2006
Sampling rate (Hz)	–	≈ 1
Averaging Period (min)	30	
Measurement Heights (m)	15, 62 amsl	63, 91 amsl

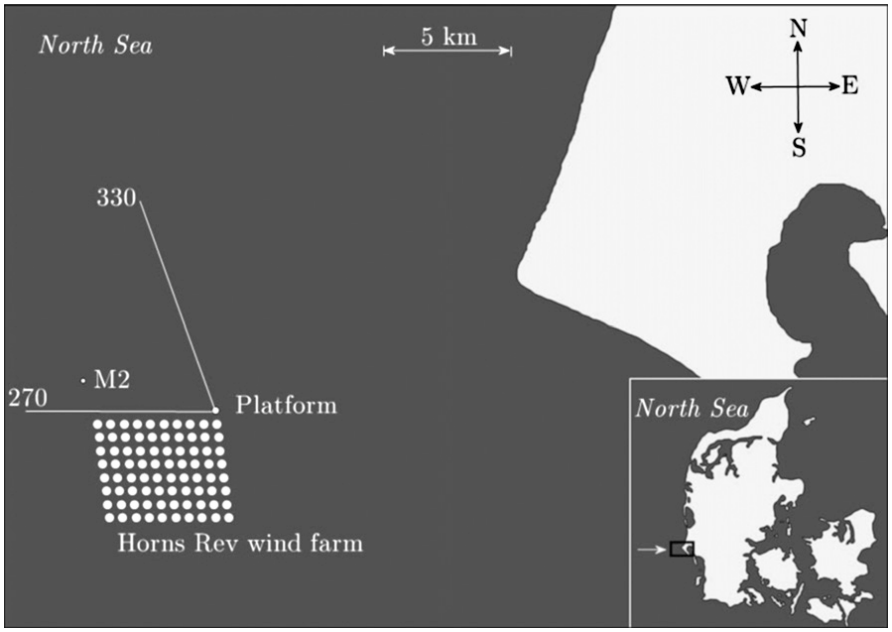

Figure 5.31: Horns Rev wind farm in the North Sea, Denmark. The positions of the meteorological mast M2, the platform and the wind turbines are indicated. At the bottom right corner, the location of the wind farm in Denmark is shown.

In order to avoid the wake effects from the wind farm, only the winds coming from the North west ($270° - 330°$) were analyzed.

5.8.3 Mean wind speed comparisons

It is to be noted that the notation used for the mean wind speed in this study is U instead of $\overline{u}$ used in other studies.

5.8.3.1 Site 1

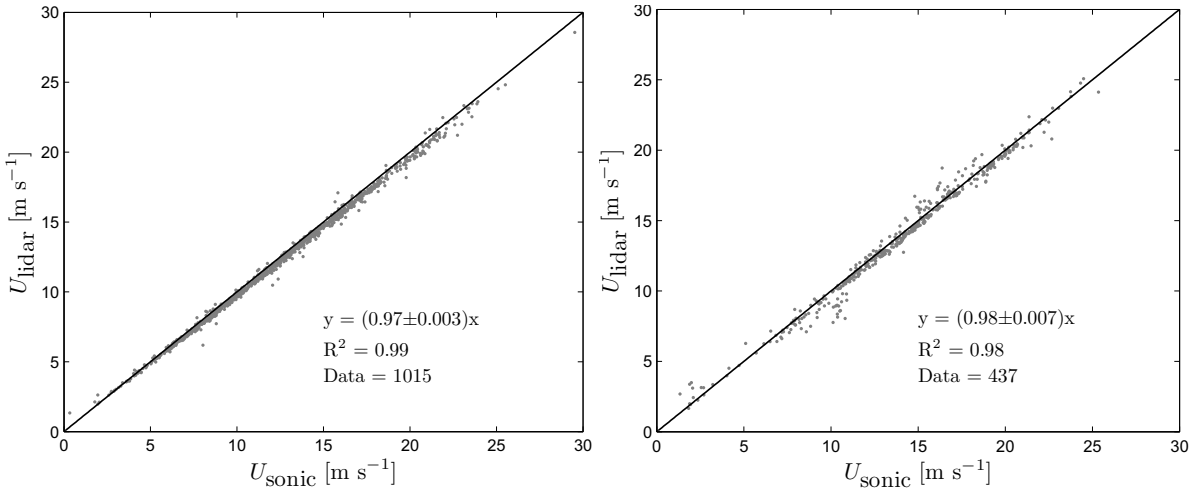

(a) 40 m (b) 100 m

Figure 5.32: Comparison of the estimated 30-min mean horizontal wind speeds from a CW lidar and sonic anemometer measurements at two different heights.

Figure 5.32 shows the scatter plot of the estimated 30-min mean horizontal wind speeds from a CW lidar and sonic anemometer measurements at two different heights. At both heights the systematic error (denoted by the slope) is of the order of 2-3 %, which is considered small. The uncertainty (denoted by the coefficient of determination R^2) is also quite small. There is thus enough confidence to proceed with the analysis of the momentum flux using the CW lidar.

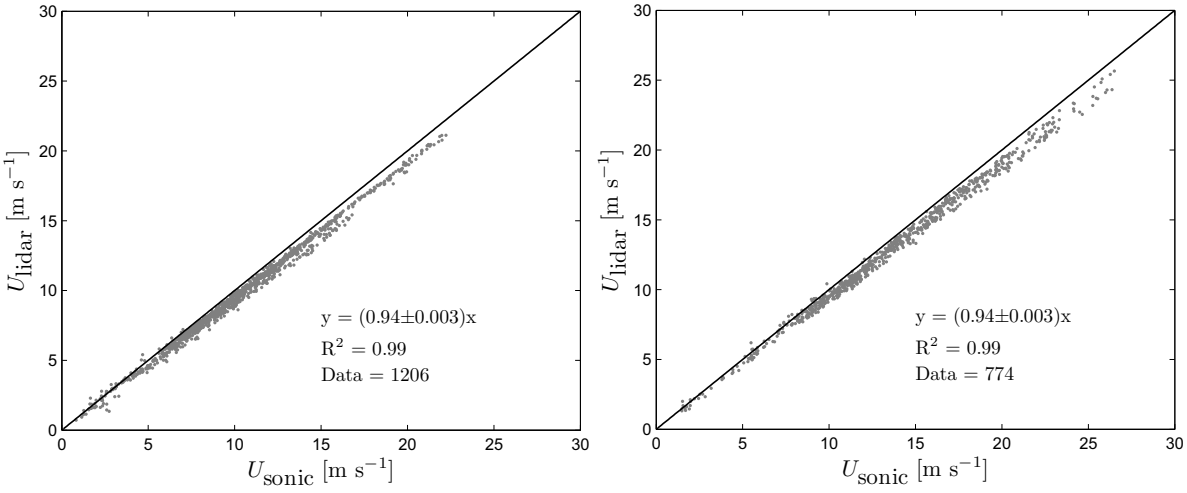

(a) 40 m (b) 100 m

Figure 5.33: Comparison of the estimated 30-min mean horizontal wind speeds from a pulsed lidar and sonic anemometer measurements at two different heights.

Figure 5.33 shows the scatter plot of the estimated 30-min mean horizontal wind speeds from a pulsed lidar and sonic anemometer measurements at two different heights. At both heights the systematic error (denoted by the slope) is of the order of 6 %, which is quite significant as compared to the same for other studies (see e.g. Fig. 5.12), where the same lidar technology is used. Therefore one must take a note of this while comparing the momentum fluxes, since the quality of the estimated second-order statistics become suspect. The uncertainty (denoted by the coefficient of determination R^2) is however quite small (of the order of $< 1\%$).

5.8.3.2 Site 2

Figure 5.34 shows the scatter plot of the estimated 30-min mean horizontal wind speeds from a CW lidar and a cup anemometer. It is to be noted that despite a horizontal separation of about 5 km, the systematic error is quite small (comparable to that at site 1). The uncertainty however is slightly larger (of the order of 2%), which is expected considering large horizontal separation between the platform and the reference met mast. There is thus enough confidence to proceed with the analysis of the momentum flux.

5.8.4 Turbulence measurements

The momentum flux $\langle u'w' \rangle$ is estimated using the variances of the radial velocities $\langle v_r'^2 \rangle$ (see Eq. 3.16) from the measurements of only two lidar beams. In Eq. (3.16), when $\theta = 0$ and $\theta = \pi$ then $\langle u'w' \rangle$ becomes a function of only the upstream and downstream radial velocity variance (see Mann et al. [2010] for more details).

At site 1, comparison of the estimated $\langle u'w' \rangle$ from the lidar measurements is carried out with that estimated from the reference sonic anemometer measurements at different heights.

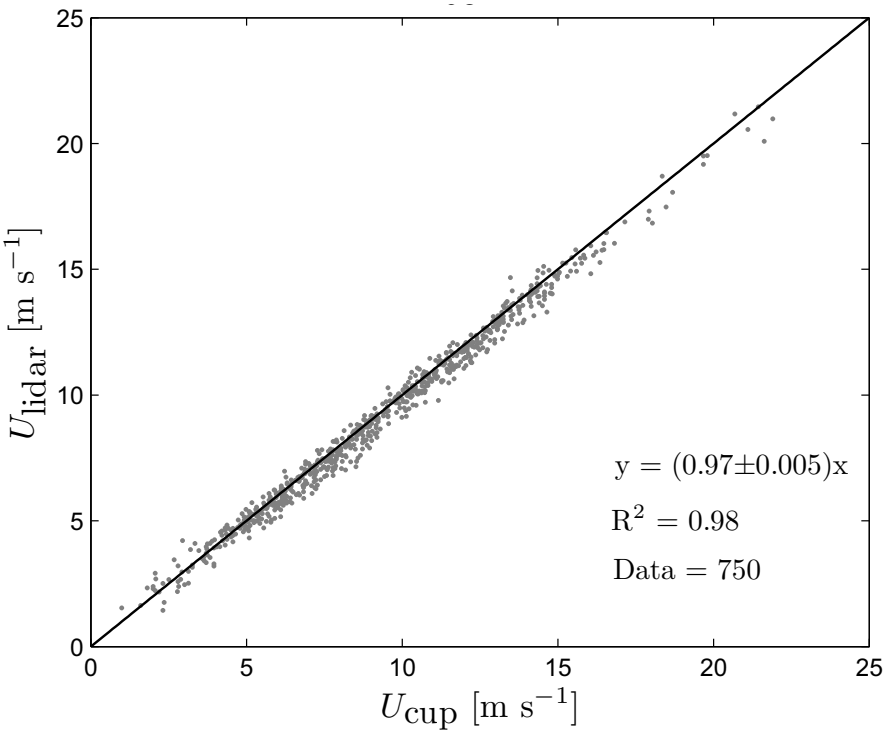

Figure 5.34: Comparison of the estimated 30-min mean horizontal wind speeds from a CW lidar and cup anemometer measurements at 63 m

At site 2, the reference $\langle u'w' \rangle$ was estimated using the Charnock's profile-derived (c-p-d) friction velocity u_* (see Mann et al. [2010] for mathematical details). From Eq. (1.12) by neglecting $\langle v'w' \rangle$ the momentum flux can be calculated. Peña et al. [2008] demonstrated that the friction velocity, derived from the combination of the sea roughness length model from Charnock [1955], the logarithmic wind profile, and the wind speed measurement at 15 m amsl is a good estimate of the momentum flux for the open sea sector at Horns Rev when compared to the sonic anemometer measurements.

5.8.4.1 Site 1

5.8.4.1.1 CW lidar

Figure 5.35 shows the comparison of the estimated filtered and unfiltered momentum flux using a CW lidar and sonic anemometer measurements at three heights. For the filtered statistics the systematic error (denoted by the slope) increases with height, i.e. the CW lidar filters more turbulence scales at higher heights than at lower heights. This is because the probe volume for a CW lidar increases quadratically with height. The filtering effect is in agreement with that observed for the variances of the wind vector components in study 1 (see e.g. Fig. 5.4a). The uncertainty (denoted by R^2) is slightly larger at 100 m than at 40 and 80 m, but there is no clear trend with height. For the unfiltered statistics, the systematic error is reduced significantly, where by the using the method described in Mann et al. [2010] the filtered turbulence scales are recovered at all heights. At 40 and 100 m there is an overestimation of the estimated momentum flux using lidar measurements, likely due to the method used to estimate the wind speed gradient that is an input variable in the Mann et al. [2010] method to recover filtered statistics. The uncertainty is also increased at all heights compared to the filtered statistics, which is a drawback of this method.

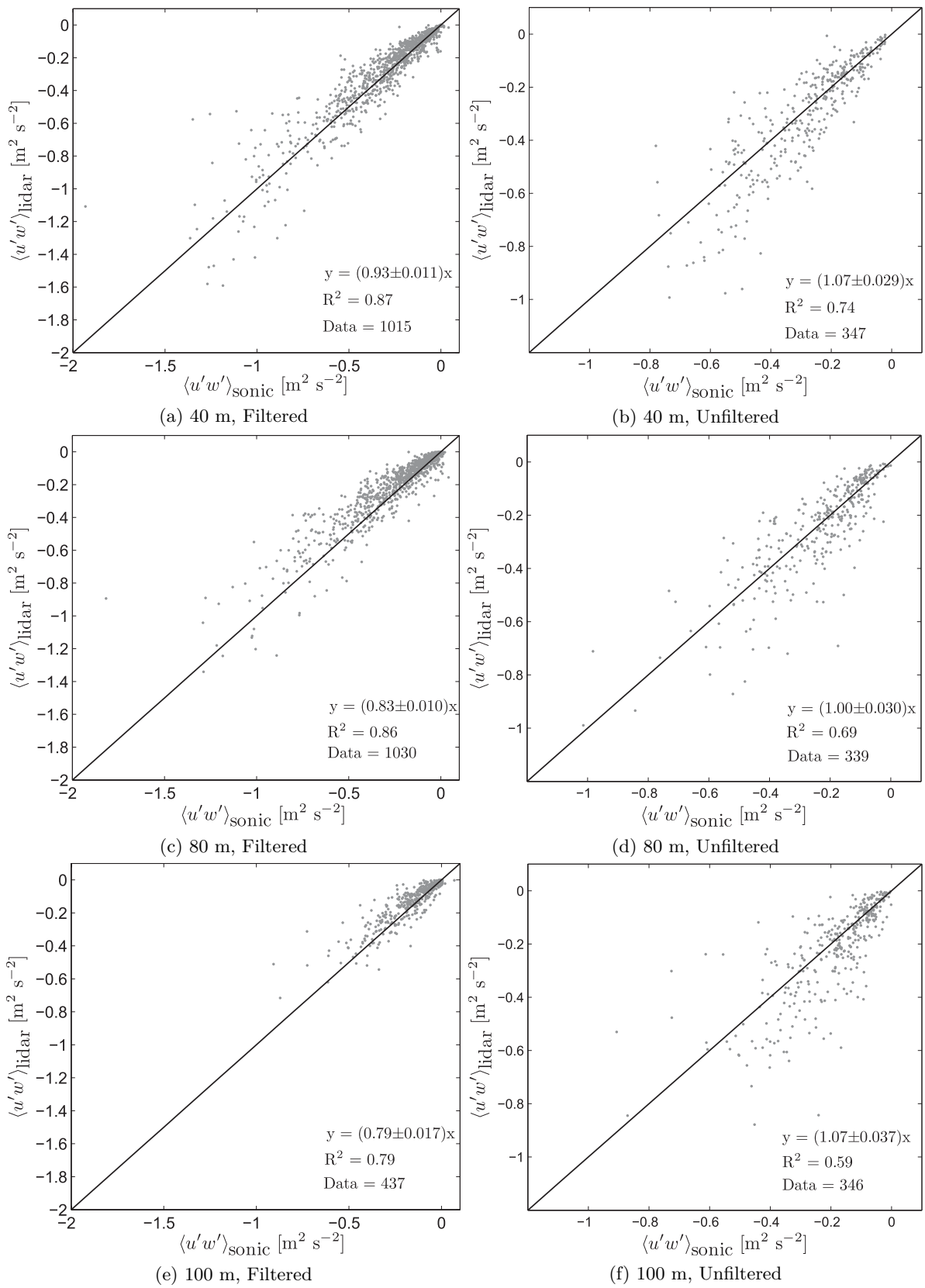

(a) 40 m, Filtered

(b) 40 m, Unfiltered

(c) 80 m, Filtered

(d) 80 m, Unfiltered

(e) 100 m, Filtered

(f) 100 m, Unfiltered

Figure 5.35: Comparison of the estimated filtered and unfiltered momentum flux using a CW lidar and sonic anemometer measurements.

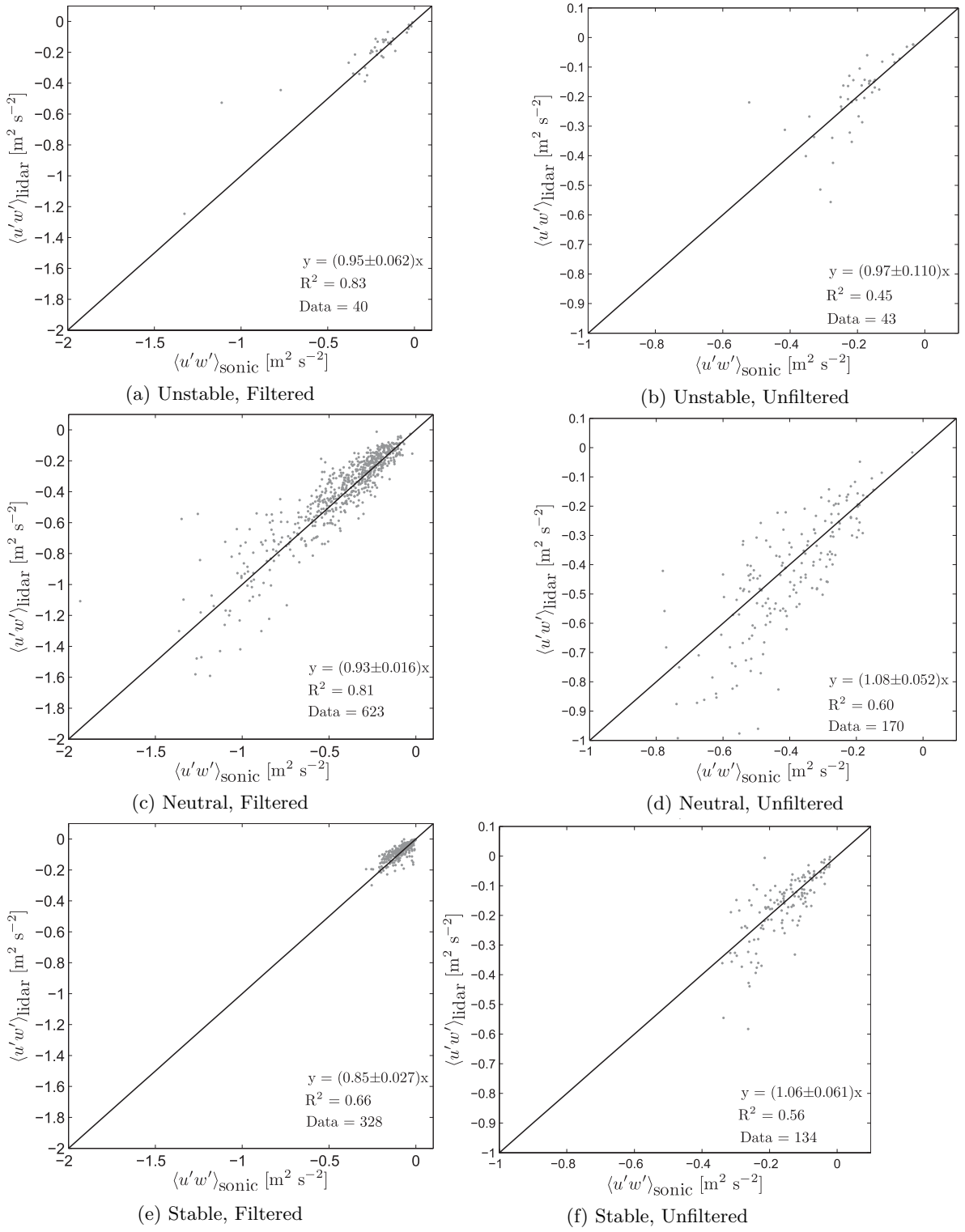

(a) Unstable, Filtered

(b) Unstable, Unfiltered

(c) Neutral, Filtered

(d) Neutral, Unfiltered

(e) Stable, Filtered

(f) Stable, Unfiltered

Figure 5.36: Comparison of the estimated filtered and unfiltered momentum flux using a CW lidar and sonic anemometer measurements under different stabilities at 40 m.

Figure 5.36 shows the comparison of the estimated filtered and unfiltered momentum flux using a CW lidar and sonic anemometer measurements under different atmospheric stabilities at 40 m. For the filtered statistics the systematic error (denoted by the slope) decreases from unstable to stable conditions, i.e. the CW lidar filters more turbulence scales under stable

conditions than under stable conditions. This is mainly due to the small turbulence scales under stable conditions than under unstable conditions. The filtering effect is in agreement with that observed for the variances of the wind vector components in study 1 (see e.g. Fig. 5.4a). The uncertainty (denoted by R^2) is significantly larger under stable conditions than under unstable conditions. For the unfiltered statistics, the systematic error is reduced significantly by using the method described in Mann et al. [2010], where the filtered turbulence scales are recovered at all heights. Under neutral and stable conditions there is an overestimation of the estimated momentum flux using lidar measurements, likely due to the large wind shears under these conditions as compared to the unstable conditions. In other words, because the wind shear is proportional to the momentum flux, the larger the wind shear the larger the momentum flux. As for different heights, the uncertainty is increased significantly under all stabilities compared to the filtered statistics, which is a drawback of this method.

5.8.4.1.2 Pulsed lidar

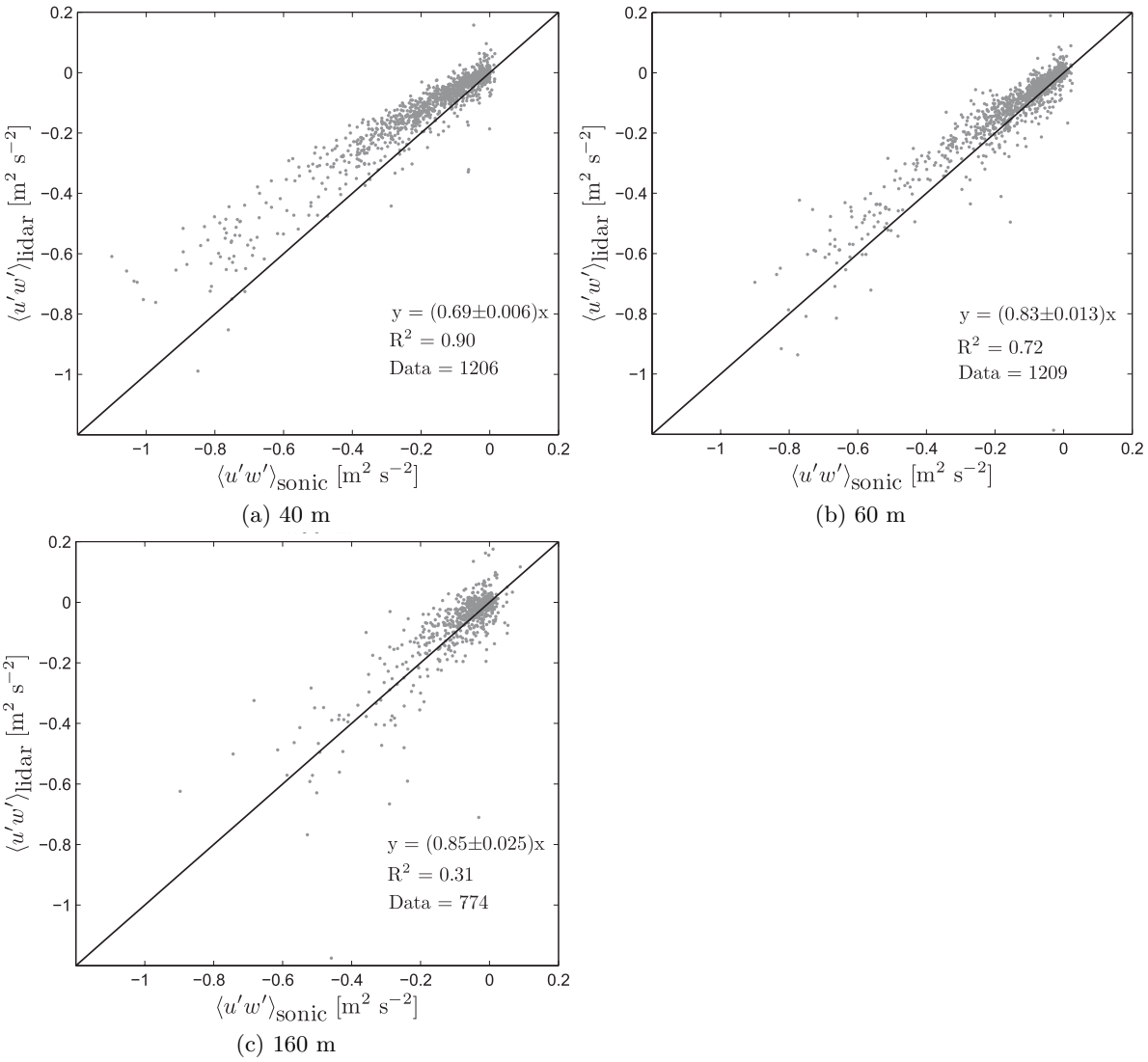

(a) 40 m

(b) 60 m

(c) 160 m

Figure 5.37: Comparison of the estimated momentum flux using a pulsed lidar and sonic anemometer measurements.

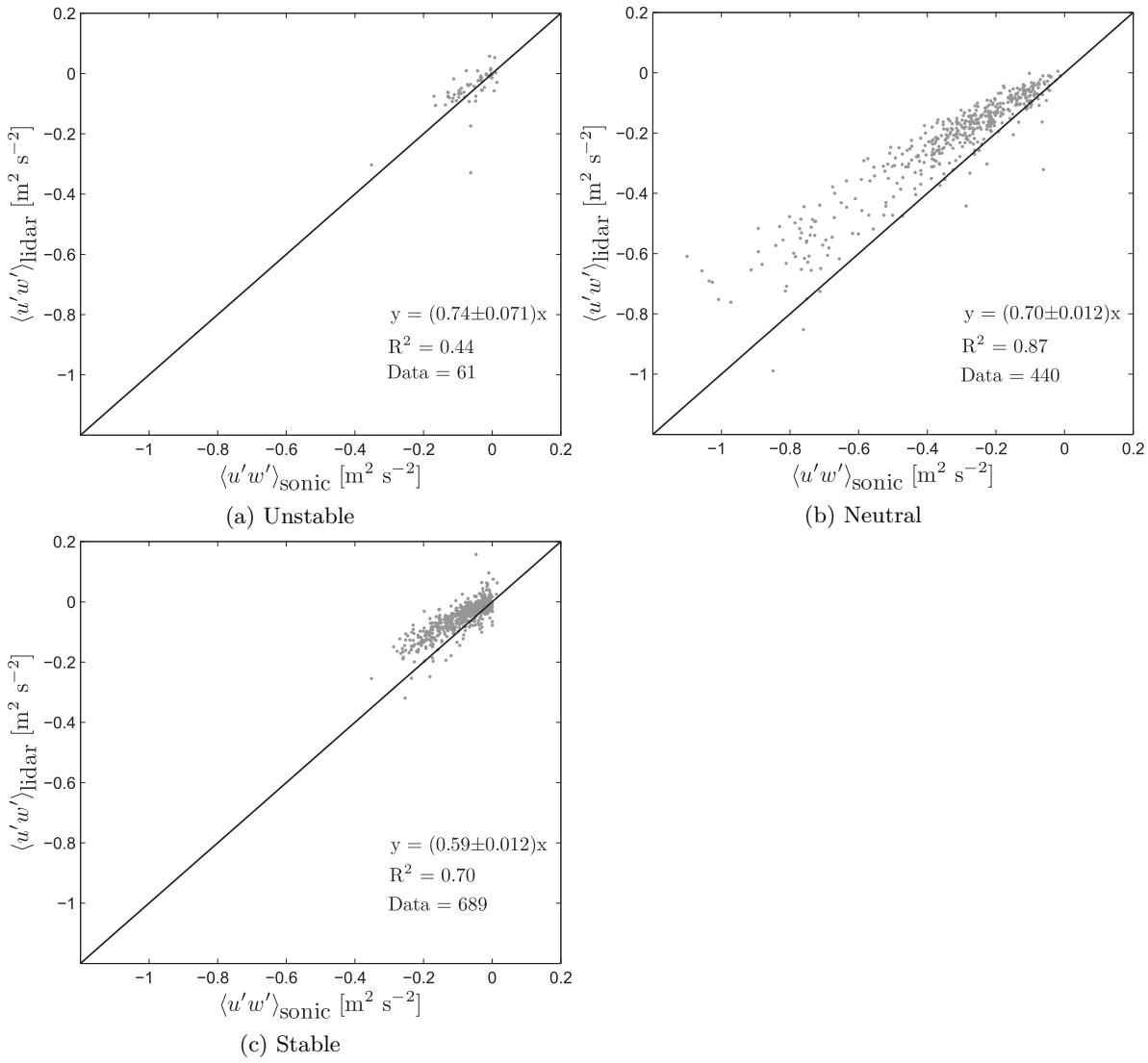

(a) Unstable (b) Neutral

(c) Stable

Figure 5.38: Comparison of the estimated momentum flux using a pulsed lidar and sonic anemometer measurements under different stabilities at 40 m.

Figure 5.37 shows the comparison of the estimated (filtered) momentum flux using a pulsed lidar and sonic anemometer measurements at three heights. The systematic error (denoted by the slope) decreases with height, i.e. the pulsed lidar filters more turbulence scales at lower heights than at lower heights. This is in contrast to that observed for the CW lidar, mainly because the probe volume of the pulsed lidar is constant, whereas that of a CW lidar increases quadratically with height. The filtering effect is in agreement with that observed for the variances of the wind vector components in study 1 (see e.g. Fig. 5.4b). As for the CW lidar, the uncertainty (denoted by R^2) increases with height and is significantly larger at 160 m than at 40 and 60 m.

Figure 5.38 shows the comparison of the estimated momentum flux using a pulsed lidar and sonic anemometer measurements under different stabilities at 40 m. As for the CW lidar the systematic error (denoted by the slope) increases from unstable to stable conditions, i.e. the pulsed lidar filters more turbulence scales under stable conditions than under unstable and neutral conditions. The filtering effect is in agreement with that observed for the variances of the wind vector components in study 1 (see e.g. Fig. 5.4b). However unlike the CW lidar, the

uncertainty (denoted by R^2) has no clear trend, where it is largest under unstable conditions. It is likely due to the small number of data points available under unstable conditions.

5.8.4.2 Site 2

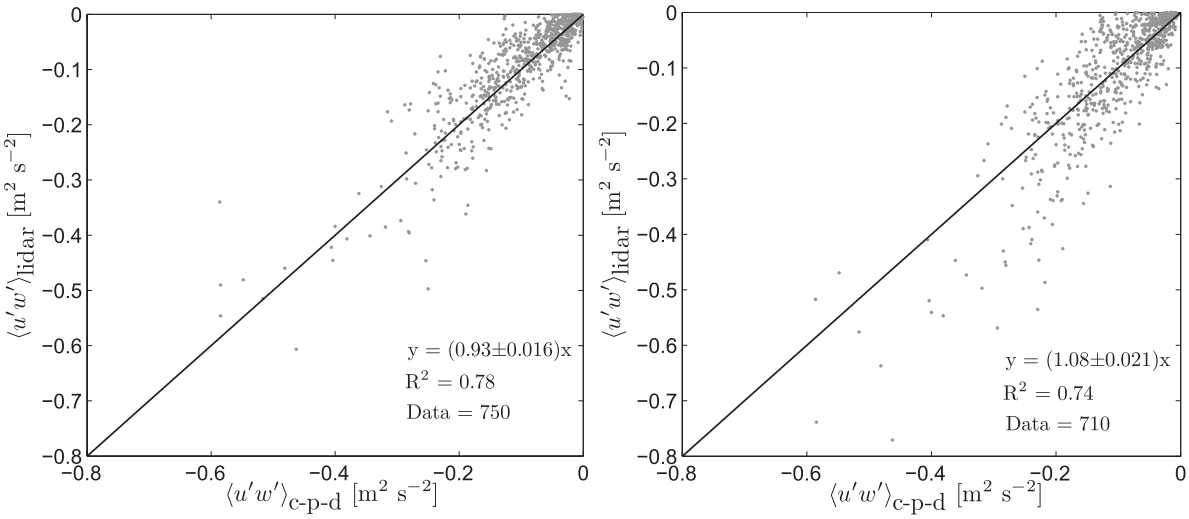

(a) Filtered (b) Unfiltered

Figure 5.39: Comparison of the estimated filtered and unfiltered momentum flux using a CW lidar and sonic anemometer measurements. The subscript c-p-d denotes Charnock profile derived momentum flux.

Figure 5.39 shows the comparison of the estimated filtered and unfiltered momentum flux using a CW lidar and sonic anemometer measurements at 63 m. For the filtered statistics the systematic error (denoted by the slope) compares surprisingly well, despite the large distance between the platform and met mast M2, where the reference momentum flux is estimated using the Charnock profiles (see Mann et al. [2010] for more details). This might be because of the relatively constant momentum flux within the marine surface layer in neutral conditions and that the flow is very homogeneous within the open sea sector. The filtering effect is also similar to that observed at 40 m for the onshore site 1. For the unfiltered statistics, there is an overestimation of about 8 %, likely due to the uncertainties in the estimation of the wind speed gradient that is used in the Mann et al. [2010] method to recover the filtered statistics. The magnitude of overestimation is similar to that observed at 40 m for the onshore site 1.

5.9 Study 9 – Roskilde, Denmark

5.9.1 Introduction

The goal of this study was to investigate the spatial averaging effects within the probe volume of a CW lidar placed on a nacelle of a wind turbine, and to test two equivalent methods of estimating the spectral transfer function $|\tilde{\varphi}(s)|^2$. In method 1, $|\tilde{\varphi}(s)|^2$ is estimated simply by taking the ratio of the estimated spectrum using lidar measurements to that estimated using the sonic anemometer measurements. In method 2, $|\tilde{\varphi}(s)|^2$ is estimated by squaring the ratio of the estimated cross spectra using the lidar and sonic time series to the auto-spectrum estimated using the sonic anemometer measurements. For more details see Angelou et al. [2012].

5.9.2 Measurement details

(a) Site Location

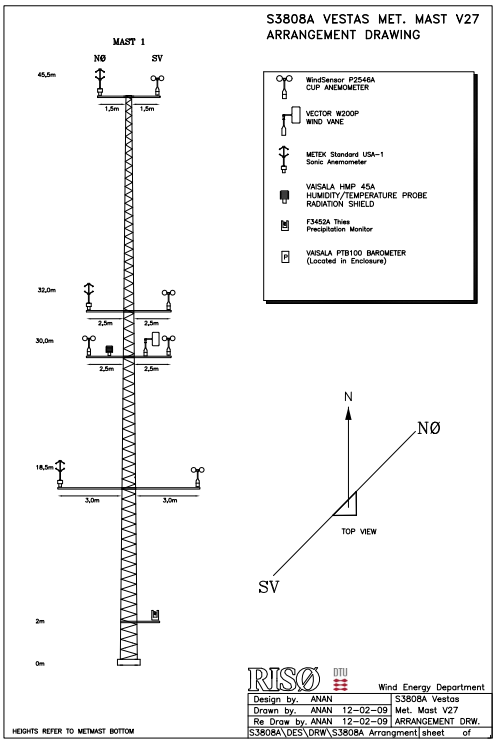

(b) Reference Met Mast

Figure 5.40: Satellite picture of the experimental site with the location of the reference met mast and the Vestas V27 turbine (Goggle Earth ©), and a sketch of the reference met mast.

Figure 5.40a shows the location of the experimental site, where the reference met mast and the Vestas V27 turbine is marked. The CW lidar is placed on the nacelle of the V27 wind turbine. In the adjacent area three other wind turbines can be seen. Two of them are in the direction 195° South-South West from the V27 turbine, whereas the third turbine is 15° North. To the west of the met mast lies Roskilde Fjord, whereas to the east is the mainland. The terrain is covered with low vegetation and can be assumed to horizontally homogeneous. Figure 5.40b shows the sketch of the reference met mast used in this study. Measurements from a reference sonic anemometer oriented in the North-East direction are used to compare with the estimated statistics from the lidar.

Table 5.8 provides the details of the instruments used in this study. The reference met mast is oriented 283° from the geographic North. The prototype CW lidar was used in a staring mode such that it pointed in the vicinity of the reference sonic anemometer. Although the experiment was carried out for a period of about three months, the analysis is restricted to wind directions that directly coincided with the lidar beam that corresponded to the an eight hour period between 12:00–20:00 CET on May 5, 2009. Throughout this period the wind turbine was not operating, and therefore the lidar measurements were free of any blade passing event. Also there was no mast wake effect on the sonic anemometer measurements, as well as no wake effects from the neighbouring wind turbines.

Table 5.8: Instrument and Measurement Details of Study 9

	Sonic	CW Lidar, ZephIR
Location, UTM zone 33U WGS84 datum	317452 m, E and 6174906 m, N	≈ 67.5 m east of the met mast
Model/Version	Metek 3D, P2546A	v1
Period of Measurement	April–June 2009	
Sampling rate (Hz)	10	
Averaging Period (min)	10	
Measurement Heights (m)	32	33.5

5.9.3 Mean wind speed comparisons

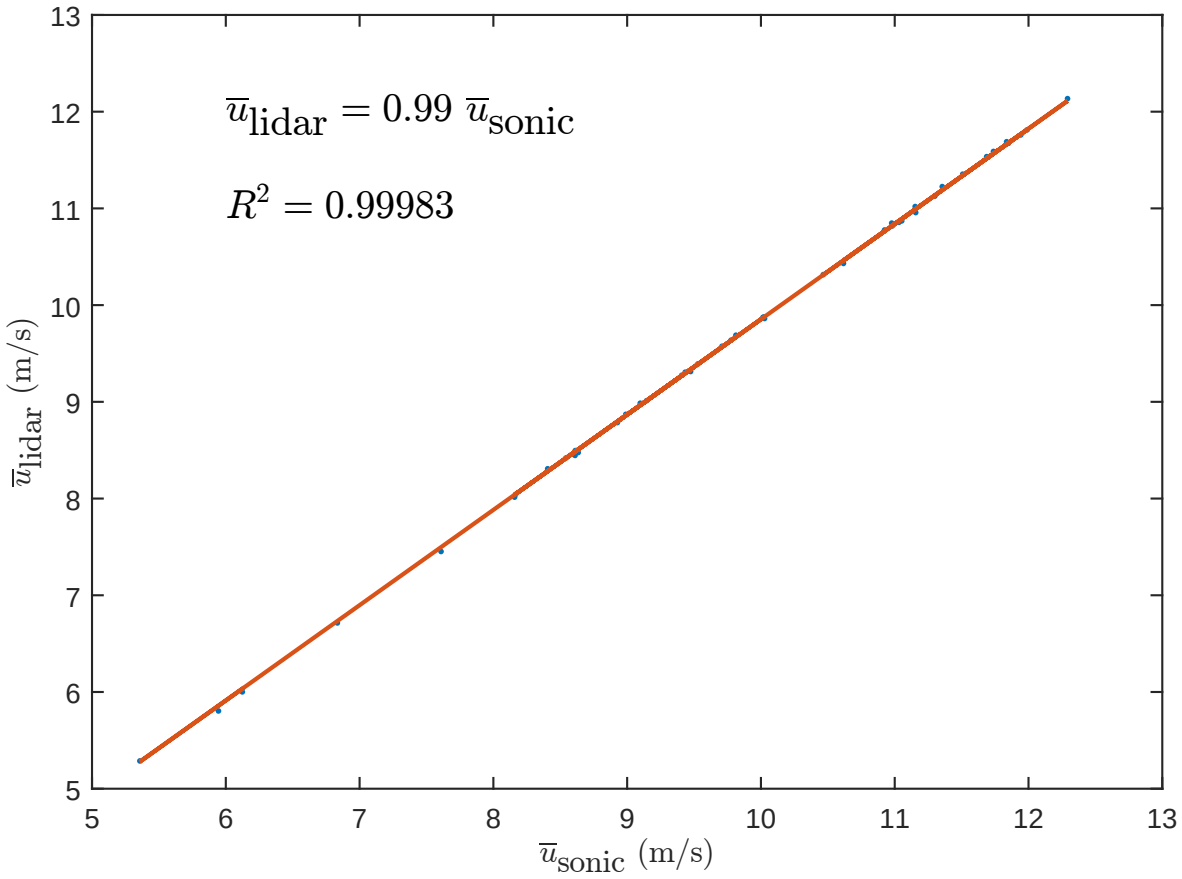

Figure 5.41: Comparison of the estimated 10-min mean wind speeds from the CW lidar and the sonic anemometer measurements at 32 m.

Figure 5.41 shows the scatter plot of the estimated 10-min mean u component of the wind vector from the CW lidar and the sonic anemometer measurements. The systematic error (denoted by the slope) and the uncertainty (denoted by R^2) is negligible. Therefore it gives enough confidence to proceed with the turbulence analysis.

5.9.4 Turbulence measurements

Due to the high sampling rate of 10 Hz of both instruments, time series of the u component of the wind vector was available for the chosen analysis period (see table 5.8 and section 5.9.2). Auto-spectra for several 10-min periods were computed from the time series and comparisons were made between the same for the lidar and the sonic.

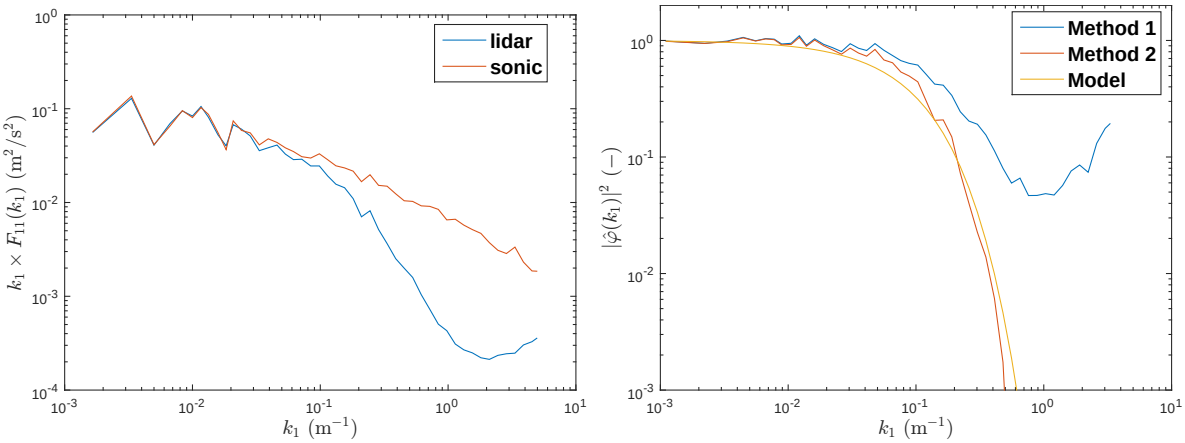

(a) u spectrum

(b) Spectral Transfer Function, $|\hat{\varphi}(k_1)|^2$

Figure 5.42: Comparison of the estimated auto-spectrum of the u component of the wind vector and the spectral transfer function using CW lidar and sonic anemometer measurements.

Figure 5.42a shows the comparison of the estimated auto-spectrum of the u component of the wind vector using CW lidar and sonic anemometer measurements. Six 10-min ensembles of the spectrum within an arbitrary one hour period were averaged to produce an ensemble average spectrum for each instrument. As also observed in independent studies 5 and 6, the filtering of small turbulence scales beyond a certain wavenumber is clearly evident due to the probe volume of the lidar. The large turbulence scales characterized by low wavenumbers are however not affected by the lidar probe volume, where there is a good match between the estimated spectral energies for both instruments.

In order to understand the spectral transfer function better, two different methods (see section 5.9.1) were used to estimate $|\hat{\varphi}(k_1)|^2$ from the lidar and sonic measurements. Simultaneously model calculations of $|\hat{\varphi}(k_1)|^2$ were also carried out and inter-comparisons are shown in Fig. 5.42b. It is interesting to note that although the two methods are in principle equivalent, different values of $|\hat{\varphi}(k_1)|^2$ are obtained at higher wavenumbers. Angelou et al. [2012] attribute the differences to two sources, the first is the misalignment between the lidar beam direction and the mean wind direction, and the second is the Doppler spectra background noise threshold. The model calculations agreed well with the estimations from method 2.

5.10 Study 10 – Roskilde, Denmark

5.10.1 Introduction

The goal of this study was to demonstrate experimentally that by using the time averaged Doppler spectrum recorded by a CW lidar, the smaller turbulence scales that are otherwise filtered out due to the probe volume of a lidar can essentially be recovered completely. A CW lidar mounted on a nacelle of a wind turbine and pointing in the mean wind direction is used. This study is a continuation of the work performed by Mann et al. [2010], where a ground based lidar was used. The implications of this experiment are significant, since

the second-order turbulence statistics can be estimated without the problem of probe volume averaging. The experimental demonstration is carried out in an open field as well as in the wind tunnel. In this report only the open field experiment is described. For more details see Branlard et al. [2013].

5.10.2 Measurement details

The location of the site and the measurement and instrument details are exactly the same as that used in study 9 (see section 5.9.2 for more details).

5.10.3 Mean wind speed comparisons

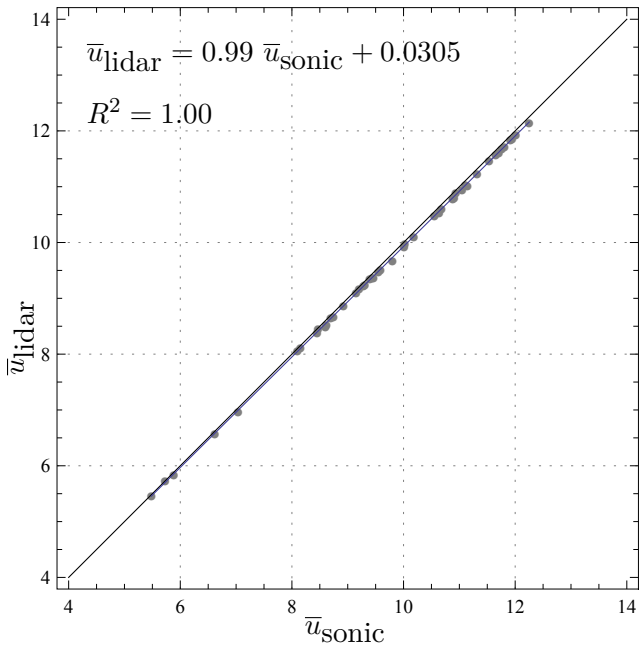

Figure 5.43: Comparison of the estimated 10-min mean wind speeds from the CW lidar and the sonic anemometer measurements

Figure 5.43 shows the scatter plot of the estimated 10-min mean u component of the wind vector from the CW lidar and the sonic anemometer measurements. The systematic error (denoted by the slope) and the uncertainty (denoted by R^2) are negligible. Therefore it gives enough confidence to proceed with the turbulence analysis.

5.10.4 Turbulence measurements

Figure 5.44 shows the filtered and unfiltered time series of the ratio of the estimated 10-min standard deviations of the u component of the wind vector from the sonic anemometer measurements to that estimated using the CW lidar measurements. The filtered ratio is obtained by using the time series of the lidar measurements, whereas the unfiltered ratio is obtained by using the average Doppler spectra. The closer the ratio to one the better the recovery of the filtered turbulence scales. It is clear that by the using the average Doppler spectra, much of the filtered turbulence scales are recovered (ratio close to one), which otherwise cannot be accomplished by simply using the time series of lidar measurements to estimate σ_u.

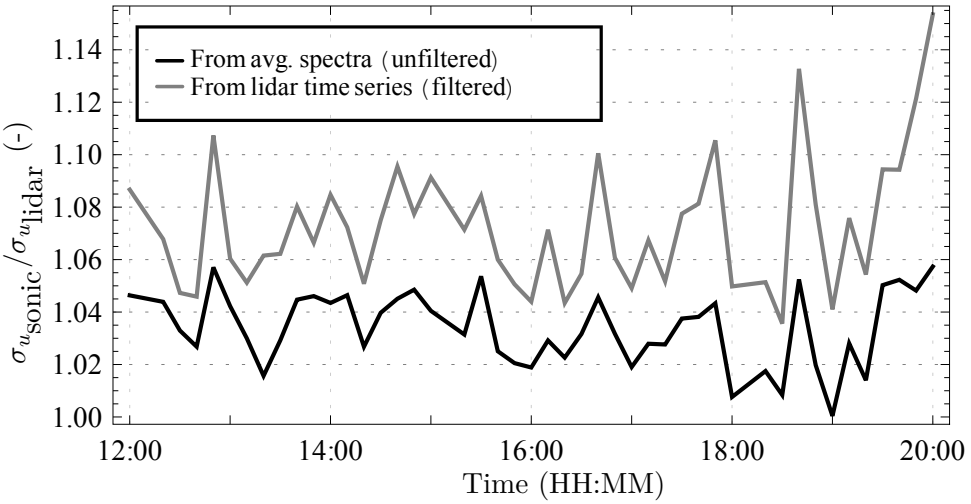

Figure 5.44: Filtered and unfiltered time series of the ratio of the estimated 10-min standard deviations of the u component of the wind vector from the sonic anemometer measurements to that estimated using the CW lidar.

5.11 Study 11 – Roskilde, Denmark

5.11.1 Introduction

The goal of this study was to demonstrate two main differences between the measurement principles of a lidar and sonic as follows.

1. On the one hand a sonic anemometer is able to measure a three-dimensional wind vector, while a lidar system is limited to line-of-sight wind speeds.

2. On the other hand a sonic anemometer is measuring within a small volume, which can be considered as a point measurement, while a lidar system is measuring over a probe volume defined by the laser pulse.

The study is based on Schlipf [2015] and has been partly presented in Rettenmeier et al. [2012].

5.11.2 Measurement details

The location of the experimental site was the same as that for studies 9 and 10, where the University of Stuttgart (SWE) pulsed lidar scanner was installed on the nacelle of the Nordtank wind turbine. Figure 5.45a shows the location of the site in Denmark (red dot), and the close-up view of the site. The details of the site are the same as those explained in study 9 (see section 5.9.2 for more details).

Figure 5.46 shows the sketch of the reference met mast that was used to compare the estimated statistics from the lidar measurements. In this study the SWE scanning lidar system was installed on the nacelle of a stopped turbine pointing towards three sonic anemometers installed on different heights on a nearby meteorological mast. More details of the experimental setup can be found in table 5.9.

Approximately 6 h of high resolution data from 11 a.m. to 5 p.m. on December 27, 2011 is analyzed. This period is chosen, because the wind is blowing almost constantly from the meteorological mast towards the lidar system during the 6 h.

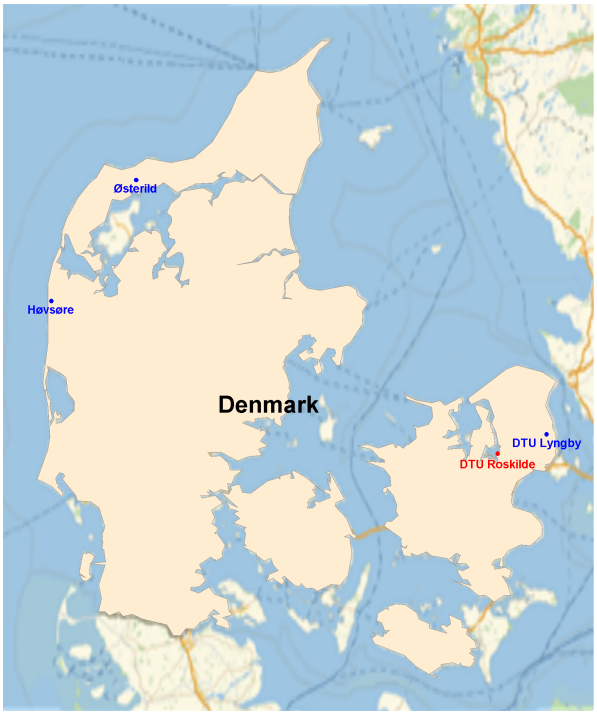

(a) Site Location

(b) Site Details

Figure 5.45: Location of the site at DTU Wind Energy department, Roskilde (red dot) and a detailed view (Goggle Earth ©)

Table 5.9: Instrument and Measurement Details of Study 11

	Sonic	Pulsed Lidar, SWE Scanner
Location, UTM zone 33U WGS84 datum	317452 m, E and 6174890 m, N	≈ 92 m east of the met mast
Model/Version	Metek 3D	–
Period of Measurement	December 27, 2011	
Sampling rate (Hz)	35	0.5
Averaging Period (min)	10	
Measurement Heights (m)	16.5, 34.5, 52.5	

5.11.3 Mean wind speed comparisons

The first part of this study focuses on the comparisons of the projected sonic wind 10-min mean wind speeds with the estimated lidar radial velocities at different heights. The projection of the sonic wind speeds is performed using Eq. (3.1). Figure 5.47 shows an example of the the scatter plot of the 10-min projected sonic wind speeds and lidar radial velocities at 34.5 m. The systematic error (denoted by the slope) and the uncertainty (denoted by R^2) is negligible. Therefore it gives enough confidence to proceed with the turbulence analysis.

5.11.4 Turbulence measurements

The second part of this study focuses on the difference between point and volume measurements. Figure 5.48 shows an excerpt of 10 minutes. Both signals have a similar time pro-

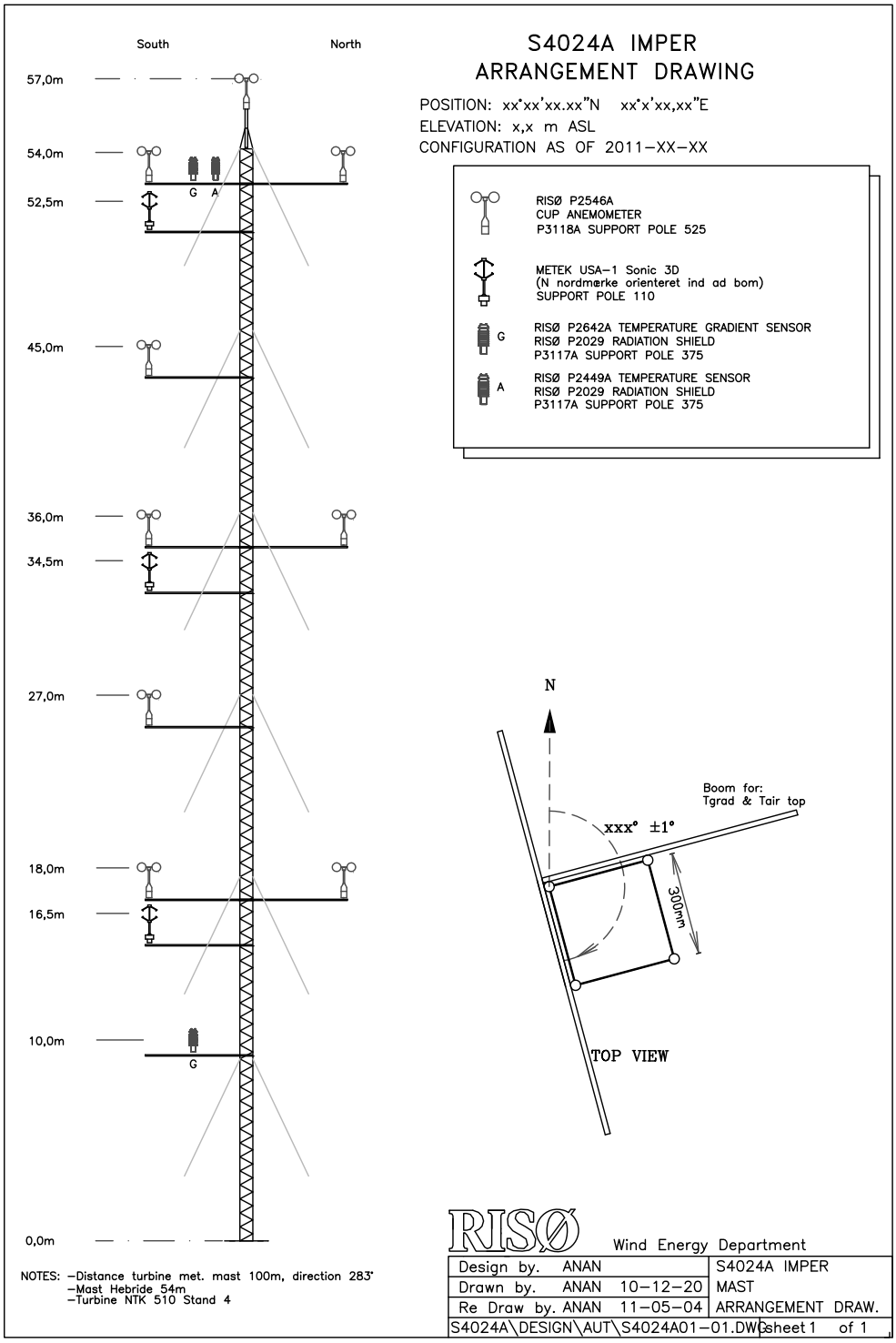

Figure 5.46: Sketch of the reference met mast used in study 11

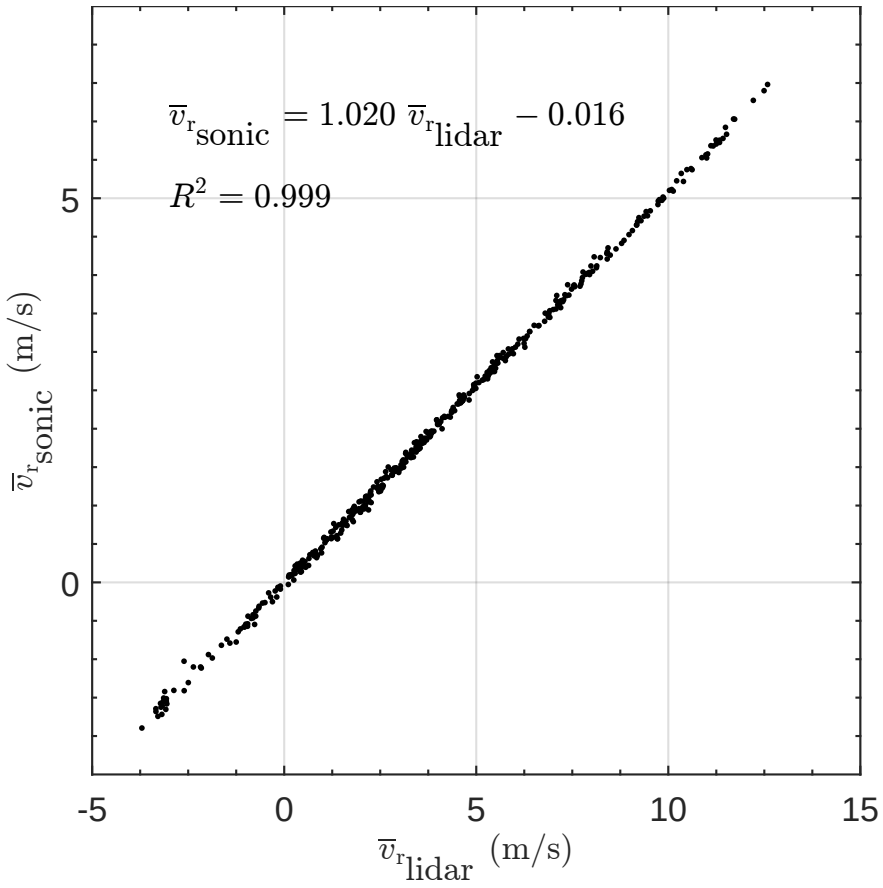

Figure 5.47: Scatter plots of the 10-min projected sonic wind speeds and lidar radial velocities at 34.5

gression. However, the sonic data show more variation at higher frequencies. This becomes more obvious comparing the auto-spectra in Figure 5.49. Subsequently, spectral analysis is performed to understand the spatial averaging effects within the probe volume of the lidar. Figure 5.49 shows the comparison of the estimated radial velocity spectrum from lidar and sonic anemometer measurements at 34.5 m. As also observed for studies 6–9, the filtering of the smaller turbulence scales is clearly evident with the drop in spectral energies beyond a certain wavenumber of the lidar estimated spectrum. In order to theoretically understand the averaging effect, modelling of the filter function of the lidar is carried out. The filtered sonic spectrum using spectral transfer function is also shown in dark gray in Fig. 5.49. For the pulsed lidar system, a normalized Gaussian shape weighting function is assumed following Cariou [2013]. The function depends on the distance to the measurement point and is parameterized by a standard deviation based on the Full Width at Half Maximum (FWHM) of 30 m. The filter function is applied to the estimated spectrum from the sonic anemometer measurements. A similar drop-off at high frequencies is observed compared to the auto-spectrum of the lidar signal in Fig. 5.49.

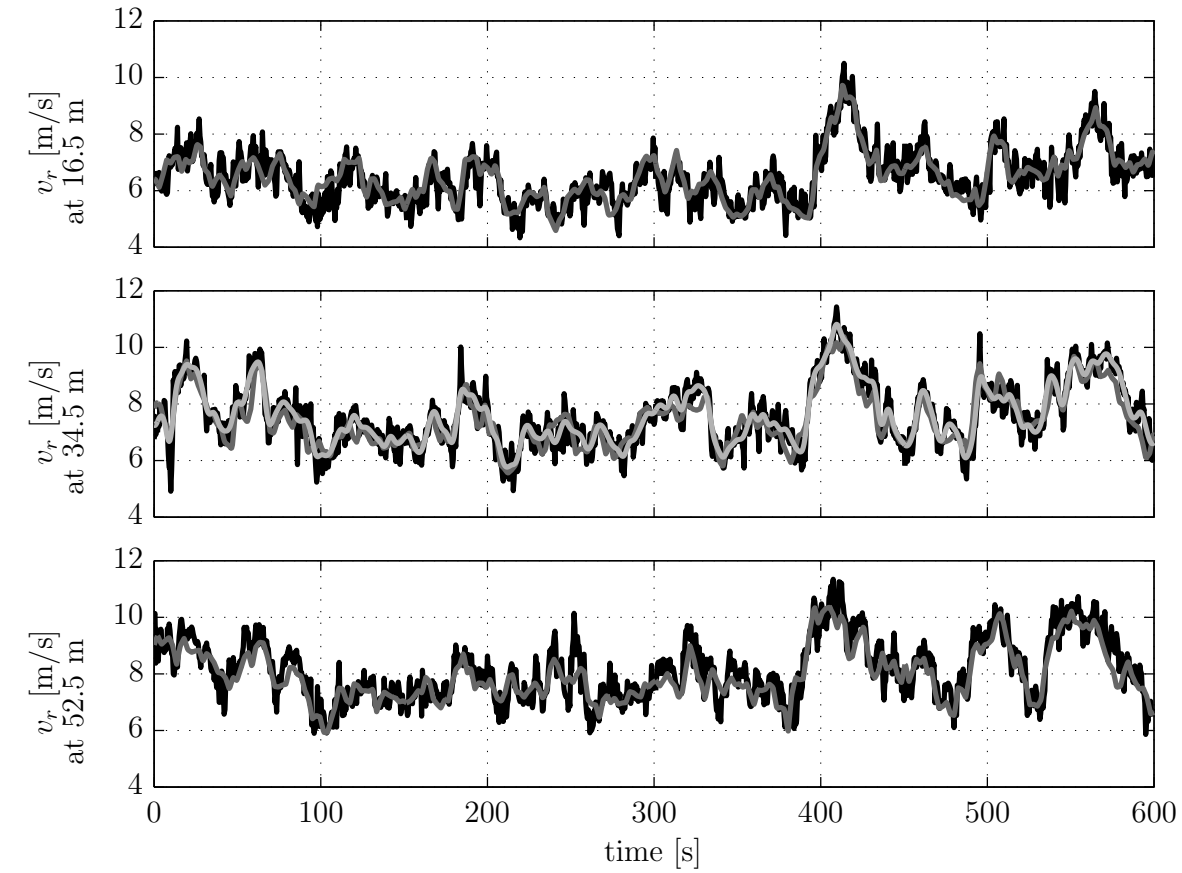

Figure 5.48: Time line of line-of-sight wind speeds. Sonic (black), lidar (dark gray) and filtered sonic (light gray).

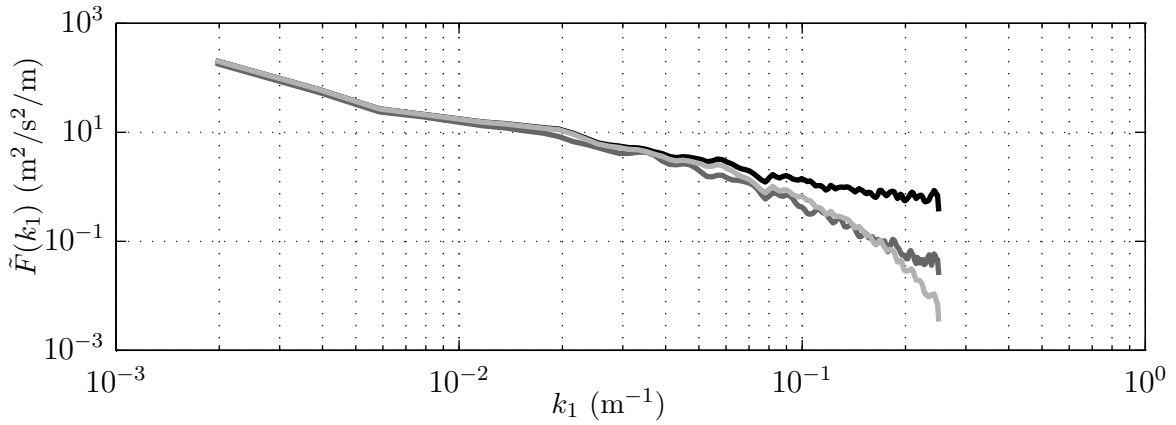

Figure 5.49: Comparison of the estimated radial velocity spectrum from lidar (light gray) and sonic anemometer (black) measurements at 34.5 m. The filtered sonic spectrum using spectral transfer function is also shown in dark gray

5.12 Study 12 – Kansas, USA

5.12.1 Introduction

The goal of this study was to better understand and model the mean and turbulence structure of the nocturnal stable boundary layer (SBL) [Poulos et al., 2002], specifically by

1. evaluating the roles and contributions of turbulence events to intermittent vertical heat, moisture, and momentum fluxes,

2. measuring heat and momentum fluxes and their vertical divergences, to assess the departures from similarity theory,

3. determining the relative importance of surface heterogeneity on nocturnal SBL evolution, and

4. measuring and studying the transition periods (evening and morning) and assessing their roles in initiating the evolution of the subsequent nighttime or daytime boundary layer.

These objectives are not achievable without measurements of turbulence profiles to some accuracy at least through the SBL.

The SBL is poorly understood and poorly modeled, and thus a significant source of error in numerical weather prediction (NWP) model predictions and wind forecasts in general. The accuracy of such forecasts is likely to be important to the success of wind energy in the US. Nocturnal profiles of wind speed and variance have a large effect on wind energy, as wind shear and turbulence associated with the SBL can induce damaging loads on wind turbine blades [Kelley et al., 2004]. A major reason for the lack of knowledge about SBL processes is a lack of accurate measurements through the SBL of mean-wind and turbulence profiles at fine enough resolution in the vertical and in time, which are 10 m or less and a few min or less [Banta et al., 2013].

The goals for the Doppler lidar were to provide those profile measurements of the turbulent velocity variances and associated mean wind speeds and use them to determine the magnitude and structure of the turbulent variance below the low-level jet (LLJ). The profiles were analyzed to better understand the evolution of the LLJ, a normal feature of the nocturnal wind profile, and the associated SBL turbulence structure, and to use the lidar's scanning capability to study flow and turbulence events, such as Kelvin-Helmholtz-type waves or small-scale fronts.

5.12.2 Measurement details

NOAA's High-Resolution Doppler Lidar (HRDL,[Grund et al., 2001]) was used during the month-long Cooperative Atmosphere-Surface Exchange Study of October 1999 (CASES-99). CASES-99 was conducted in the tall grassland of southeastern Kansas, where the terrain was relatively flat but with gullies and occasional trees. The comprehensive instrumentation consisted of a 60 m reference met mast with "a large number of sensors with high sampling rates mounted upon it "[Poulos et al., 2002]. Fig. 5.50 shows the topography of the CASES-99 experiment. The HRDL lidar location at 37.6360° N, 96.7339° W (elevation 429 m)is also marked.

At six levels from 2.5 to 60 m, 10 or 20 Hz sonic or thermosonic anemometers were mounted in roughly 10 m intervals. Between those sensors slow-response sensors provided additional information at 5-m separationâĂę. Additionally microbarographs sampling to 1 Pa at 2 Hz were mounted at 1, 30, and 50 m. 34 thermocouples (E-type, chromel/constantin, 0.0254-mm diameter) capable of 5 Hz absolute temperature measurements were distributed in 1.8-m increments from 2.3 to 58.1 m above the ground, providing unprecedented vertical resolution of temperature changes [Poulos et al., 2002].

The reference met mast also included precision infrared radiometers at 2 and 48 m above ground. A number of 10 m reference met masts and other instrumentation were deployed at various distances from the main site (the site with the 60 m met mast) to sample atmospheric

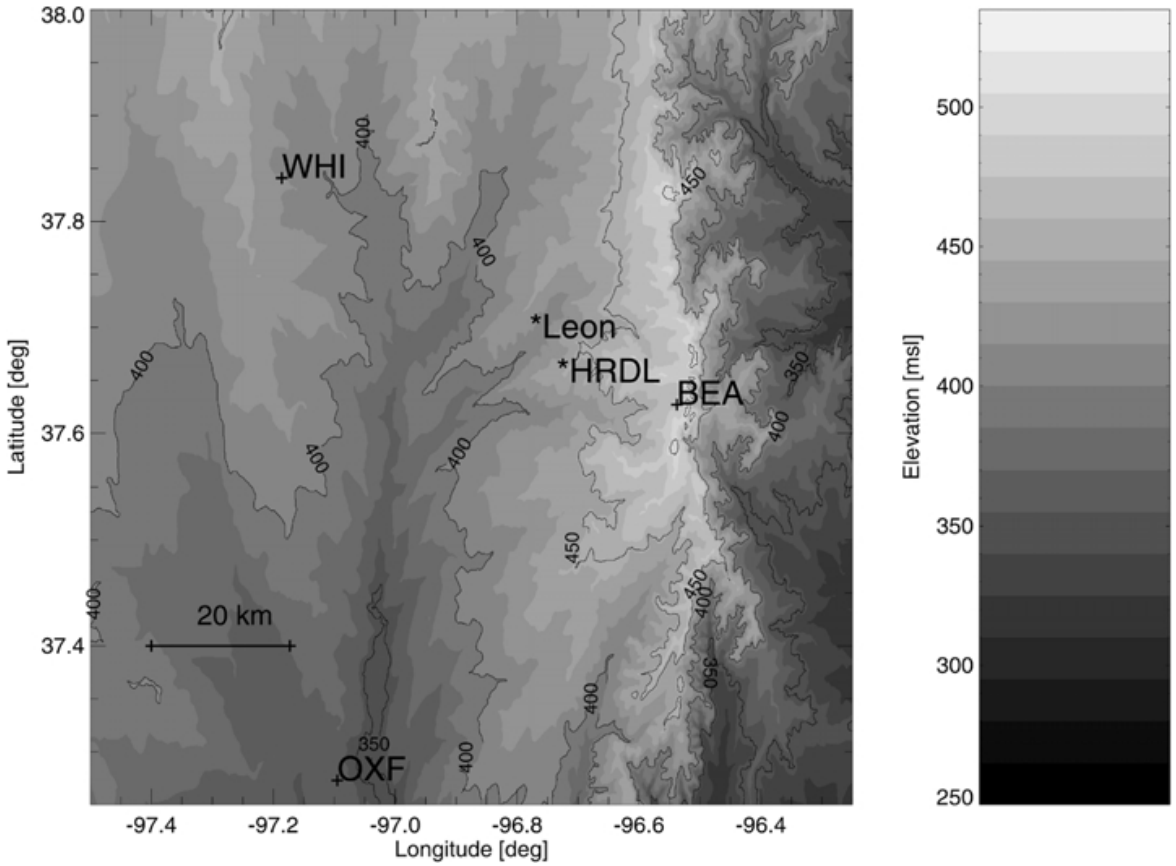

Figure 5.50: Topography of the CASES-99 experimental site and location of the HRDL lidar; reproduced from Banta et al. [2002]

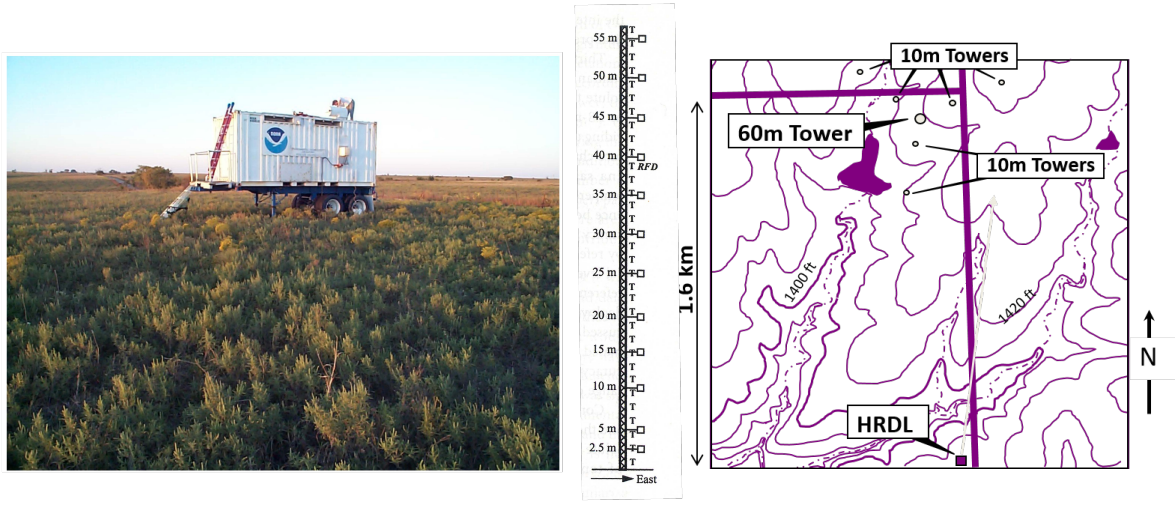

Figure 5.51: (left) HRDL at its CASES-99 site, showing the Kansas terrain. (middle) Sketch of 60-m tower, showing heights of anemometers (squares) and thermocouples (T); reproduced from Poulos et al. [2002]. (right) Topographic map showing location of HRDL relative to 60-m and other 10-m towers and to local terrain features.

features of various horizontal length scales (see Poulos et al. [2002] for additional information). In addition to the met mast, vertical profiling was performed by a kite profiling system,

tethersondes, radars, sodars, and lidars, including HRDL, which was sited 1.5 km to the south of the main (60 m) met mast (see Fig. 5.51, right panel).

Routine scans consisted of the following types:

1. Azimuth or conical scans over a full 360° at fixed elevation angles, ranging from 0.5° to 45° at various times during the project. These scans were used to determine the mean wind speed and direction as a function of height, using a modified VAD processing technique that allowed all scans within a given averaging interval (30 min for many CASES-99 analyses performed) to be included in the calculation [Banta et al., 2002]. These scans, whose *images* give an indication of the horizontal variability of the flow, were used to document the evolution of the mean wind speed and direction profile, to calculate properties of the LLJ and other mean-flow features, and, in real time, to orient the elevation scans (described next) along the mean wind.

2. Elevation, or vertical-slice, sector scans (typically up to 20° or 30° elevation) to compute the vertical structure of the mean flow and turbulent streamwise variance. These scans took 20-30 s to complete. The data within each scan were binned in the vertical, and the mean wind speed and variance were computed within each vertical bin for a specified averaging period to form profiles of these quantities (see Fig. 5.52). Thus, profiles were available for averaging periods as short as the 20 or 30 s it took to complete one scan, although for most published CASES-99 results these data were averaged over 15-min intervals. However, profiles for time intervals as short as 1-3 min were used to form time-height color-coded cross sections illustrating the relationship between LLJ evolution and the development of turbulence below the LLJ.

3. Vertical staring, to obtain time series and statistics of the vertical wind speed w.

The data acquisition procedure consisted of performing repeated elevation (vertical-slice) scans over periods of 15-30 min, typically between elevations from 0° to 20°âĂŤ30°, interspersed with periodic conical scans to calculate the mean wind speed and direction using VAD. The mean wind direction was used to orient the elevation scans parallel to the wind (directional shear was typically small through the SBL). Line-of-sight data from the vertical-slice scans were corrected to find the horizontal component, and these data were divided into vertical bins as shown in Fig. 5.52. Mean wind speeds were calculated from the data points in each bin to form mean-wind profiles ($\overline{u}(z)$), and, after removing the mean vertical shear, variances were calculated for each bin to form streamwise variance profiles ($\overline{u'^2}(z)$).

5.12.3 Mean wind speed comparisons

Comparisons of HRDL-measured mean wind speeds with those measured by the reference sonic anemometers at different heights on the 60-m tower were carried out, showing agreement to within 0.1 m/s (bias corrected because of the spatial separation). For CASES-99, this was regarded as capable of fulfilling project objectives, but these results were not published formally.

5.12.4 Turbulence measurements

HRDL vertical-slice scans were used to estimate the streamwise variance $\langle u'^2 \rangle$ for two strong-LLJ nights from the CASES-99 dataset. Banta et al. [2006]and Banta [2008] used these techniques to study nocturnal wind and $\langle u'^2 \rangle$ profiles. They found that the speed and height of the LLJ maximum were important scaling parameters for the SBL (Fig. 5.53), and quantitative relationships, such as, that the near-surface maximum of σ_u in the σ_u profile had a value of 5%

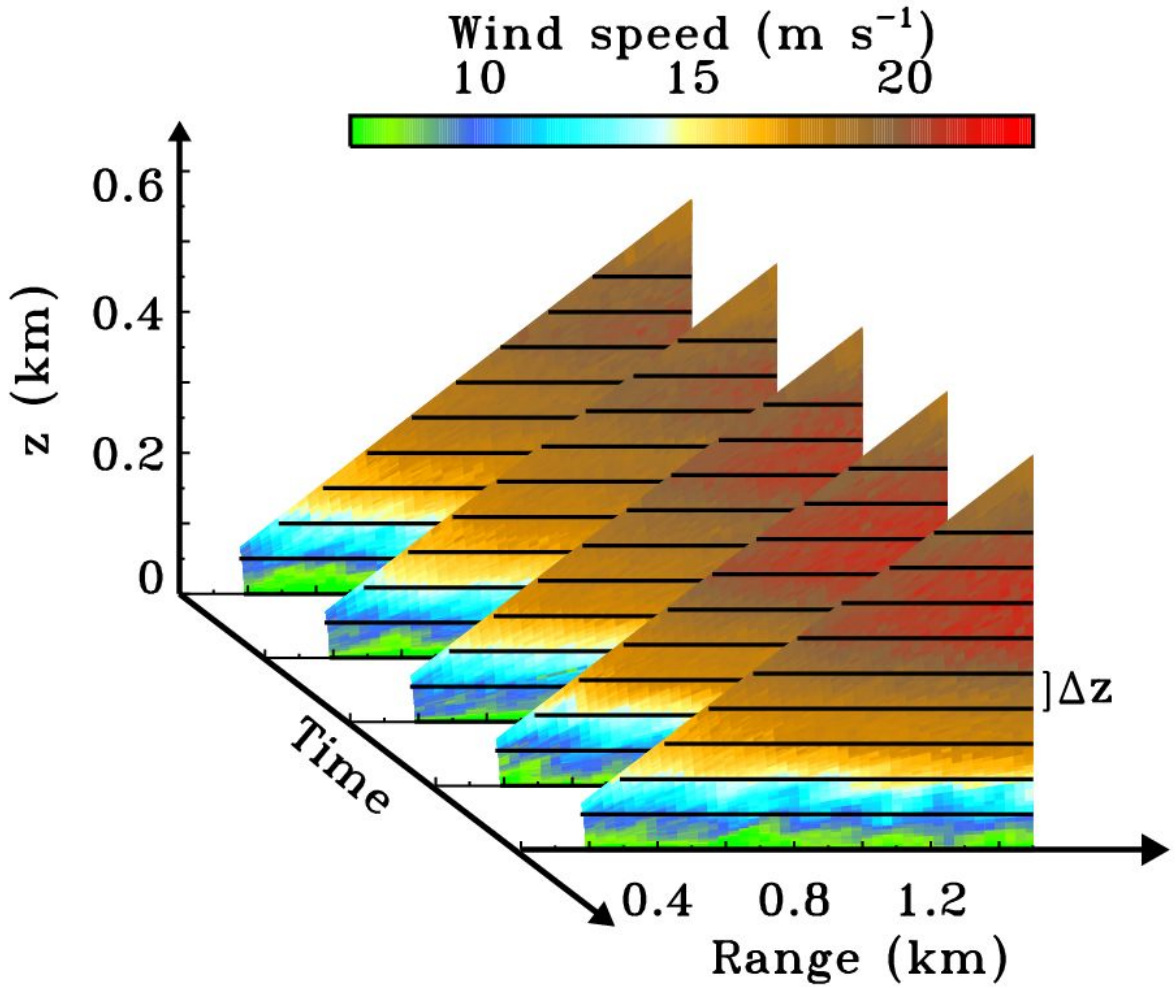

Figure 5.52: Example of vertical slice scans from the HRDL lidar, illustrating the vertical binning procedure [Pichugina and Banta, 2010]. Depth of the bin Δz depicted here is 50 m for illustration, but actual intervals used for computing $\overline{u}$ and σ_u^2 varied from 1 to 10 m. ©American Meteorological Society. Reprinted with permission.

of the peak LLJ speed, i.e. $\sigma_u/\overline{u}_{\mathrm{LLJ}} \approx 0.05$. Three profile shapes were found in the variance profile depending on stability, with the least stable profiles having a 'traditional' structure where the maximum $\langle u'^2 \rangle$ is at the surface (Fig. 5.53), and the most stable exhibiting an 'upside down' structure where the maximum value is aloft, tending to occur at a height near 60 m. The first minimum value of $\langle u'^2 \rangle$ above the surface was often associated with the nose of the LLJ (Fig. 5.53), indicating that the top of the SBL was at the LLJ nose.

In addition to performing statistics on the HRDL dataset, the scan data themselves can be used to obtain quantitative measurements of important aspects of turbulent eddies and other fluctuations in the flow. Individual scan images allow one to visualize the eddy structure, and repeated scans can be animated to give a clear picture of how the eddy structure evolves. Recalling that each pixel in the image represents a number, eddy properties such as amplitudes, length scales, and propagation speeds, as well as the resulting turbulent variance profiles, can be calculated. Newsom and Banta [2003] performed such an analysis on a 20-min period of shear-instability, **K-H-type waves** that were sampled during CASES-99. The analysis showed that the wave properties agreed unexpectedly well with those of linear wave theory, even though visually the measured waves appeared to be starting to overturn. This

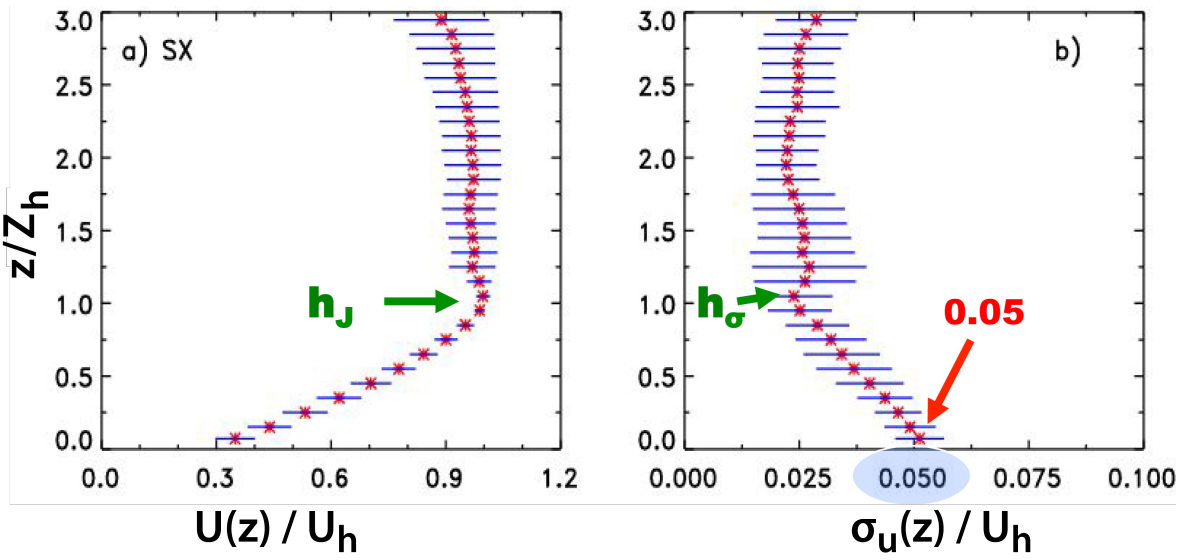

Figure 5.53: Composite vertical profiles of a) the mean wind speed and b) the standard deviation of the u component of the wind field normalized by the wind speed at the LLJ maximum. Mean value for each level is indicated by red $*$, and horizontal error bar indicates ± 1 standard deviation of the statistic [Banta et al., 2006]. ©American Meteorological Society. Reprinted with permission.

kind of image data of waves and other turbulence structures confirm that the large eddies are being well sampled by the lidar, and thus are included in the calculations of the variance profiles.

5.13 Study 13 – Colorado, USA

5.13.1 Introduction

The goal of this study was similar to that of study 12, where special emphasis is on the nighttime stable boundary layer (SBL) and its relationship to the low-level jet (LLJ). The LLJ is a recurrent nocturnal maximum in the mean wind profile that is an important resource for wind energy. Of prime importance for studies of the ABL is how turbulence and turbulent fluxes depend on mean quantities and mean gradients, which are generally strongest in the vertical.

Doppler lidar objectives were to provide these kinds of profile measurements and apply them to better understand SBL and LLJ dynamics and their connections. Another important goal was to determine the top of the SBL, which was defined by the first near-zero minimum above the surface in the magnitude of turbulence variables. The top of the SBL determines the SBL depth, which is a very important quantity for understanding and critical to NWP modeling of the SBL. To accomplish these science goals, it is important to verify the Doppler lidar measurement techniques against reference set of tower sonic anemometers. This verification was another objective of this project.

5.13.2 Measurement details

NOAA's High-Resolution Doppler Lidar (HRDL, [Grund et al., 2001]) provided mean wind and turbulent velocity-variance profiles for the 2003 Lamar Low-Level Jet Project (LLLJP-03), also in the US Great Plains. The LLLJP-03 was located on a local plateau about 30 km

Study13MetTower.png

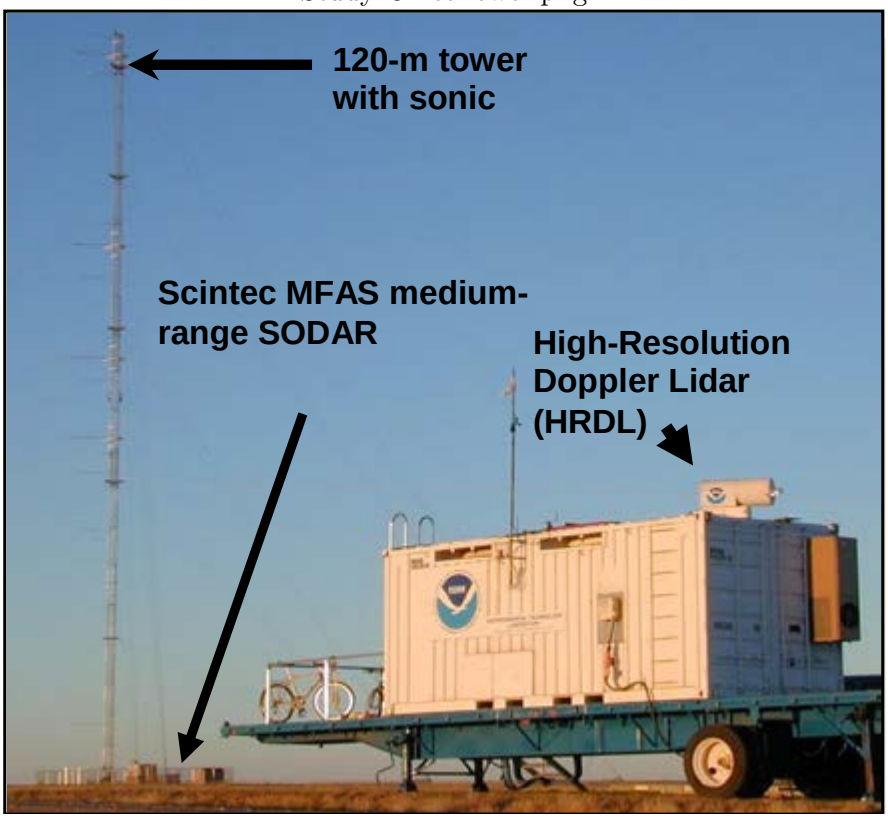

Figure 5.54: Photograph of HRDL lidar at the LLLJP-03 site, with 120-m tower and sodar also indicated (courtesy Scott Sandberg).

south of the town of Lamar, Colorado, USA [Kelley et al., 2004, Pichugina et al., 2008]. The relatively flat terrain consists of rolling grass-covered hills, and in the years since the project, a wind farm of more than 100 turbines has been built at this site. Instrumentation consisted of a 120 m tower and a Doppler sodar, which were in place for 1.5 years prior to the project, and HRDL, which joined the experiment during September 2003 (Fig. 5.54).

On the 120 m meteorological tower (located at 37.6657° N, 102.6657° W, elevation 1362 m), 3-axis sonic anemometers (Applied Technologies, Model SAT/3K) mounted at heights of 54, 67, 85, and 116 m provided 3-component wind and virtual temperature data (see Fig. 5.55) at 20 Hz during the hours of 16:00-08:00 mountain standard time (23:00-15:00 UTC). Means and variances were calculated over intervals of 1, 5, and 10 min. The sodar, a Scintec Model MFAS, measured the along-beam wind component at several azimuths. These components were used to calculate mean wind speed and direction at 10 m vertical resolution every 10 min over a nominal height range of 40 to 500 m. Figure 5.56 shows the tower-sodar layout and the direction of the lidar from the tower for the project (left panel), and the geometry of the radial-velocity intercomparisons with the tower (right panel).

Exactly as was the case for study 12, the data acquisition procedure consisted of performing repeated elevation (vertical-slice) scans over periods of 15-30 min, typically between elevations of 0° and 20° or 30°, interspersed with periodic conical scans to calculate the mean wind speed and direction using VAD. The mean wind direction was used to orient the elevation scans parallel to the wind (directional shear was typically small through the SBL). For Lamar the 10-min profiles from the sodar were also used to track and adjust the wind direction. Line-of-sight data from the vertical-slice scans were corrected to find the horizontal component, and these data were divided into vertical bins illustrated in Fig. 5.52 for CASES-99. Mean wind

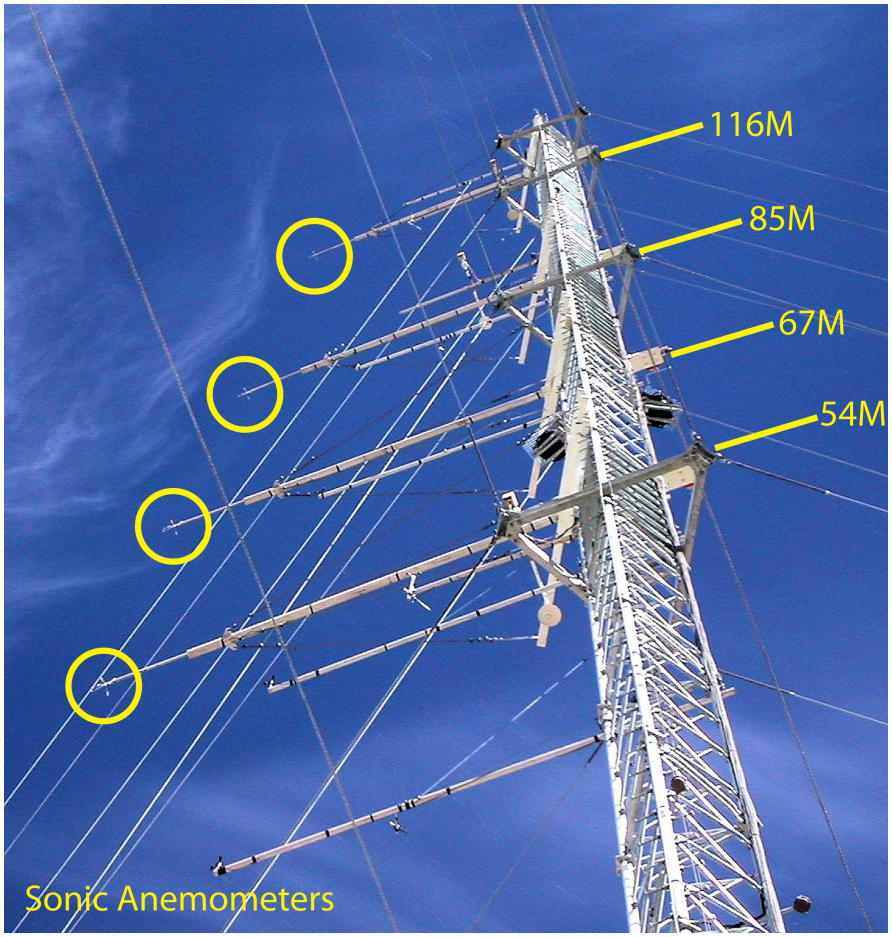

Figure 5.55: Photograph of the LLLJP-03 120-m met tower, showing heights of the four sonic anemometers (from Kelley et al. [2004])

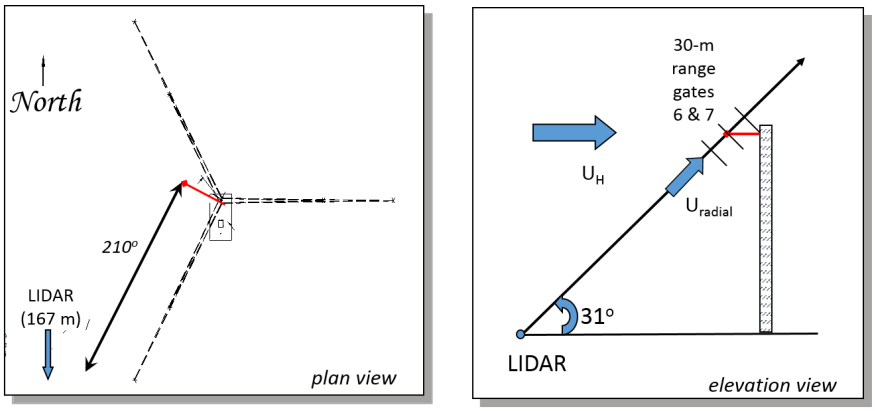

Figure 5.56: (Left) the tower-sodar layout and the direction of the lidar from the tower for the project, and (right) the geometry of the radial-velocity intercomparisons with the tower (from Kelley et al. [2004]).

speeds were calculated from the data points in each bin to form mean-wind profiles, and, after removing the mean vertical shear, variances were calculated for each bin to form streamwise variance profiles $\langle u'^2 \rangle(z)$.

5.13.3 Mean wind speed comparisons

Mean wind speeds calculated from HRDL vertical-slice scan data represent a horizontal and temporal average along each horizontally-oriented bin (Fig. 5.52) over the period of averaging, which was 1, 5, or 10 min. Wind speeds from the sonics were averaged over the corresponding time interval for comparison. The distance between the lidar-scan baseline and the tower varied for different mean wind directions, since the lidar scan was aimed along this direction. Pichugina et al. [2008] found that, 'the agreement between lidar and sonic anemometer varied significantly between nights'. On strong-wind nights correlations were high: on the two nights when the LLJ speed was strongest, the correlation coefficients were 0.95, and on the five nights when the LLJ speed u_{LLJ} exceeded 15 m/s, correlation coefficients were greater than 0.9. On the low wind speed nights ($u_{\mathrm{LLJ}} < 7 - 8$ m/s) correlation coefficients values were as low as 0.7. Pichugina et al. [2008] attributed this to, 'greater influence of horizontal variability, including terrain effects, and flow nonstationarity, which were observed in the lidar scans at the lower wind speeds' due to the spatial separation and sampling differences between the two procedures. Other lower-wind-speed issues noted were larger changes in wind direction during an averaging interval, 'difficulties in estimation of prevalent wind direction, existence of directional shear in the vertical (not observed at the higher wind speeds), and positioning the lidar beam precisely along the mainstream wind'.

Much work on uncertainty due to spatial variability needs to be done. Perhaps one of the most revealing aspects of this study is that the high-wind nights reliably show high correlation coefficients, indicating that the strong winds, shear, and turbulence effectively smear out the horizontal variations in the flow, and thus also providing confidence in the measurement techniques. At lower wind speeds, the effects of horizontal variability and nonstationarity can express themselves and produce greater differences in the mean wind values derived by the different measurement techniques.

These results highlight the important issues related to spatial vs. point sampling. For wind-energy applications, two opposing points of view could be stated: the HRDL-measured mean values, representing an area average across the lidar scan, is more representative of the area mean (needed by wind energy) than the point measurement of the tower; or, alternatively, the 'footprint' of the tower-sonic measurement is in fact representative of a larger area and the differences are due to lidar sampling and processing issues. The truth, of course, is most likely somewhere in between these two points of view, and this is where work is needed.

5.13.4 Turbulence measurements

HRDL vertical-slice scans were used to estimate the streamwise variance $\langle u'^2 \rangle$ for each vertical bin to form a profile. Values for height bins that overlapped with each tower-measurement height were compared with the appropriate sonic anemometer data. It was well understood that there were many reasons to expect poor agreement between these two estimates, such as those related to non-stationarity of stable flows, horizontal flow variability, differences in sampling geometry and processing procedures, and others [Pichugina et al., 2008]. The purpose of the Pichugina et al. [2008] intercomparison study was to see whether useful correlations between turbulent variances could be obtained under some conditions. One unexpected finding was that in the stable conditions of this study, $\langle u'^2 \rangle$ was proportional to e with a proportionality constant of near 1.0; in other words, the magnitude of $\langle u'^2 \rangle$ was approximately equal to the magnitude of the TKE. Although surprising, Banta et al. [2006] showed that this result is consistent with other available SBL measurements, and Pichugina et al. [2008] (their Fig. 3) demonstrate this equivalence by virtue of high correlations of streamwise variance vs. TKE when both are measured by sonic anemometers, at multiple tower levels.

HRDL $\langle u'^2 \rangle$ values were estimated for several vertical intervals (1, 5, 10 m) and several time

intervals (1, 5, 10 min). The appropriate averaging time interval for stationary turbulence can be expressed in terms of an Eulerian integral time scale τ [Lenschow et al., 1994], which is the time equivalent of the integral length scale ℓ_{ij} (see Eq. 1.4). Problems for stable conditions are, first τ is a very difficult and unstable statistic to calculate in the atmosphere even under relatively favorable conditions, and second the atmosphere is nonstationary, especially under stable conditions. Pichugina et al. [2008] estimated τ from sonic data using three different techniques for all nights of LLLJP-03, and, as expected, the time series jumped around and values varied widely. If a typical value were to be assigned, it would probably be 3-10 s.

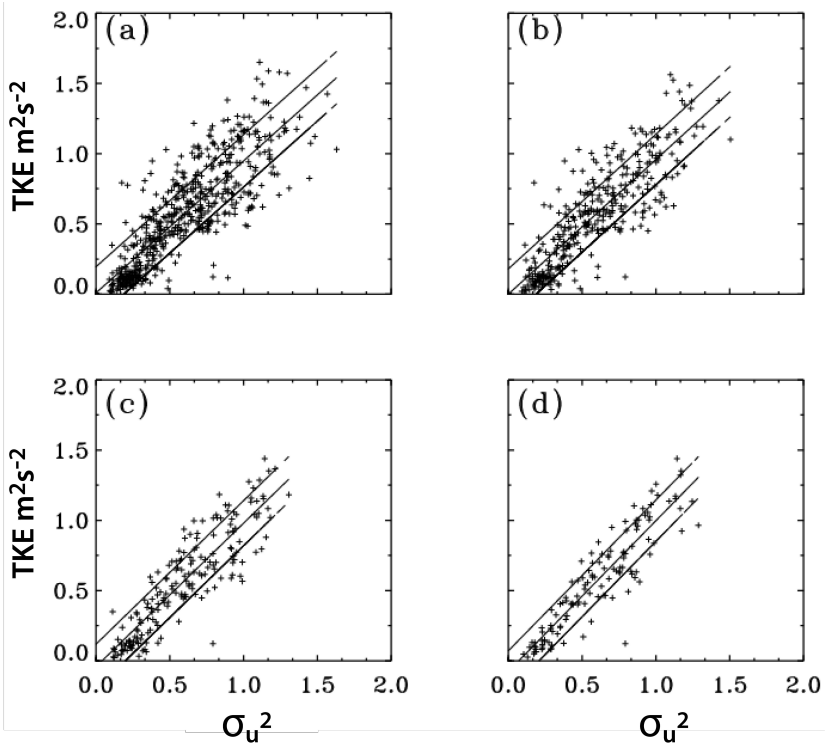

Figure 5.57: Scatter plot of the turbulent kinetic energy e estimated from the HRDL lidar and sonic anemometer measurements at one height, but for different averaging periods, (a) 2, (b) 5, (c) 10, and (d) 15 min. [Pichugina et al., 2008] ©American Meteorological Society. Reprinted with permission.

Using 5 s as a representative τ value, the Lenschow et al. [1994] procedure requires an averaging period of $\approx$ 20 min for a 10% standard error of the variance estimate. Such periods of steady τ were rare in the dataset. An analysis of one such period is given. The results were about the same as those presented for periods when τ behavior was more erratic. Thus, little advantage was evident to restricting the analysis to 'well behaved' periods. Alternative approaches for analysis of time series have been developed by Vickers and Mahrt [2003, 2006]. They developed a method for averaging over shorter intervals of variable width based on the multiresolution heat-flux cospectrum. They further average these short interval values over a 1-hour period, to reduce random flux sampling errors. Fluxes calculated in this way were well behaved. The SBL in the present study more resembles the Mahrt-Vickers conditions. Therefore, one of our approaches was to calculate the variances over a smaller interval of 1 min, then further average over longer intervals of 3-15 min [Pichugina et al., 2008](p. 1310).

Results for a representative night indicate correlation coefficients of $\sim$ 0.75 for 1-min averaging, increasing, as expected for 5-min averaging to values of $\sim$ 0.85 because of the larger sample size. For 10-min intervals, the correlations decreased slightly, possibly as a

result of nonstationary effects. For this night, the results were relatively insensitive to the vertical binning interval, but for another night the results were different for different vertical binning, indicating that the magnitudes of the variances can be sensitive to the bin depths chosen. To investigate the effects of nonstationarity, Pichugina et al. [2008] averaged together consecutive 1-min means for 3-, 5-, 10-, and 15-min periods for both instruments to roughly emulate the Vickers-Mahrt approach. The results show that this procedure produced the best fit of all, with correlation coefficients of 0.90 for averaging 10 or 15 successive 1-min means. This improvement in correlation is an indication that nonstationary effects contributed to the variance magnitude in the previous examples. An example is shown in Fig. 5.57. The favorable correlation statistics and RMS errors of 0.2 m^2/s^2 show that the HRDL $\langle u'^2 \rangle$ values measured in this way should be useful for investigating atmospheric turbulence dynamics and the structure of turbulence profiles.

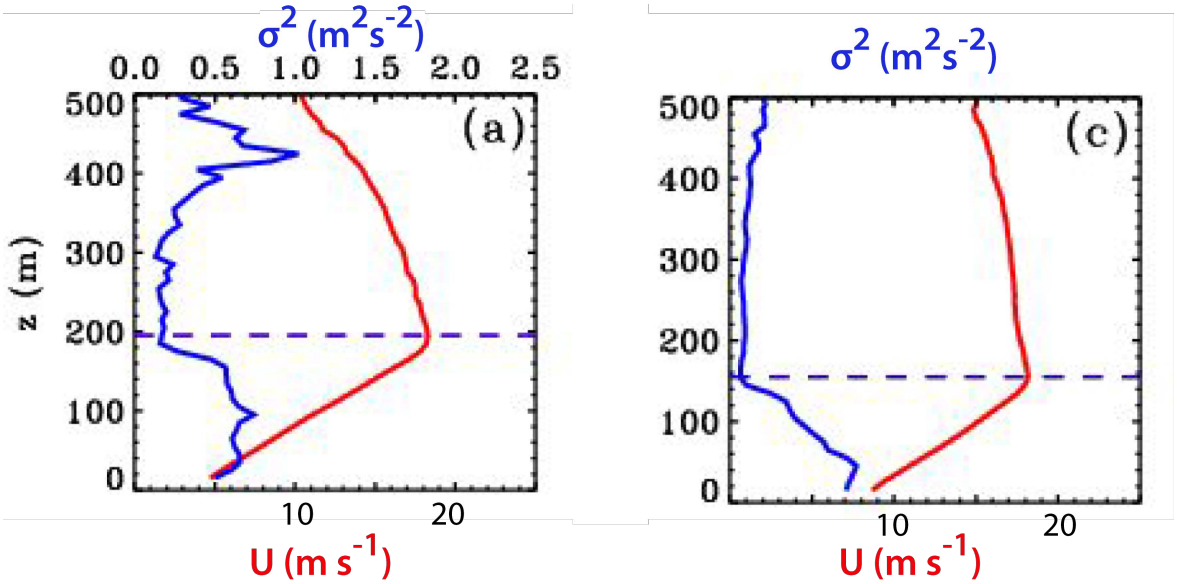

Figure 5.58: Profile of the mean wind (red) and streamwise variance (blue). [Pichugina and Banta, 2010] ©American Meteorological Society. Reprinted with permission.

The SBL top, and therefore its depth, is a critical basic quantity for modeling and understanding SBL structure, but it has proven to be very difficult to measure, as mentioned previously. Pichugina and Banta [2010] further investigated this quantity by finding the height of the $\langle u'^2 \rangle$ minimum (Fig. 5.58), in accordance with the fundamental definition of boundary layer, which is, the atmospheric turbulent layer adjacent to the surface. Relating this height to features of the mean wind profile, such as the LLJ nose or the layer of strong shear, they were able to show that SBL depth could be determined from HRDL mean-wind profile data to less than 5% under conditions that are identifiable *a priori*.

Chapter 6

Conclusions and Future Perspectives

6.1 Conclusions

At the outset it is to be noted that this report concerns characterization of atmospheric turbulence only on micro scales, and not on meso or synoptic scales. Following chapter 1, it is clear that usually, for meteorological or wind energy purposes, characterization of turbulence often requires estimating one or more turbulence quantities defined in Eqs. (1.1)–(1.12) at approximately a point. From Eq. (3.2) it is clear that the raw lidar measurements are never obtained at one single point, but over a certain probe volume. Thus unless the commercial lidars are used in a non-routine manner (see section 3.1.2), or novel techniques are used (see section 3.2), the smaller scales of turbulence, many of which are also relevant for wind turbines would always be filtered out, resulting in underestimation of a turbulence quantity in comparison to a reference instrument. It is also to be noted that the temporal resolution of lidar measurements is usually much lower than that of the reference instrument. While this will also result in filtering of smaller turbulence scales, its effect is not comparable unless the cycle time of one measurement is of the order of 30 s.

In the past decade, several commercial lidars, both CW and pulsed have sprung up, where the most common scanning strategy is placing the lidar on the ground and making conical scans (see section 3.1). In these lidars the routine method is to post-process the data using either the VAD or the DBS method to obtain the wind vector components. From chapter 3, we also understand that apart from the aforementioned smaller scales averaging effect, this also results in contamination of the turbulence statistics due to the two-point correlations of different wind vector components. As a consequence on some occasions we might obtain the 'right results for the wrong reasons' (see studies 1–5). For example, in Fig. 5.4b, at 100 m, the ratio of $\langle u'^2 \rangle$ estimated from the lidar measurements to that obtained from the reference sonic measurements is approximately one, which would erroneously indicate the ability of lidars to correctly quantify turbulence. However, as can be observed at other heights and atmospheric stabilities, the conflicting effects of the systematic errors, i.e. underestimation due to the probe-volume averaging, and overestimation due to the cross-contamination do not cancel each other. Therefore the ratio is other than one on most occasions. It is therefore recommended to not use the VAD or DBS method in estimating turbulence statistics.

Fortunately, as seen in chapter 4, significant research has been carried out in either post-processing the data better or in scanning configurations, so much so that even with a commercial lidar, ε could be estimated as described in section 3.1.2. The problem of contamination by cross-correlations can be reduced significantly by using the six-beam method with one lidar

(see sections 3.2.2 and 5.3), or by using a three lidar system (see section 3.2.5). The biggest challenge then is to recover the filtered smaller scales of turbulence, which could be carried out either by conically scanning lidars (see section 3.1.2) or by simply staring a lidar at one distance (see section 3.2.1). In principle one could then combine the retrieved large and small scale turbulence to characterize micro-scale turbulence. As seen in studies 8 and 10, a new method developed by Mann et al. [2010] demonstrates a great potential for recovering the filtered turbulence scales, by simply using the average Doppler spectra.

A possibly important aspect of turbulence measurements using lidars that has not been considered in this report is the instrumental error, which is generally assumed to be uncorrelated [Frehlich et al., 1998, Lenschow et al., 2000]. Fortunately for modern commercial lidar systems, the magnitude of the instrumental error is not significant, and can be safely neglected [Mann et al., 2009]. However, for those lidar instruments that have significant instrumental error and therefore could potentially bias turbulence measurements, the techniques suggested by Frehlich et al. [1998], Drobinski et al. [2000] and Lenschow et al. [2000] can be used to perform corrections.

Finally it is encouraging to understand that the lidars themselves (commercial or research grade) do not exhibit any significant limitation in the technology. The routine methods of characterizing turbulence are however not recommended. Some additional tricks (as described in chapter 3) in either post-processing or scanning configurations are therefore required to obtain meaningful turbulence quantities. It is also recommended to perform as fast scans as possible in order to avoid filtering of smaller turbulence scales due to coarse temporal resolution.

6.2 Future Perspectives

Having seen in chapter 4 that a significant amount of research has been carried out to characterize atmospheric turbulence in a meaningful manner, an obvious question thus arises; is there anything new to be discovered with regards to processing raw lidar data, scanning configurations, or the technology itself that can provide more reliable turbulence measurements using lidars? The future perspectives are thus outlined:

1. Raw lidar data processing – up until now, the processing algorithms that have been developed have shown that by combining an isotropic turbulence model with lidar measurements, we are able to estimate ε, $\langle v_r'^2 \rangle$ and $\mathscr{L}$ (see Table 4.1). However, turbulence is not isotropic in all range of scales. Anisotropy is particularly observed on longer length scales, and thus it is more desirable to estimate $\langle v_r'^2 \rangle$ and $\mathscr{L}$ by combining an anisotropic turbulence model [Kristensen et al., 1989, Mann, 1994] with the lidar measurements. This recommendation was also made by Frehlich et al. [2006] and Frehlich and Kelley [2008]. There is, however, a need for developing algorithms that make as little use of models as possible in combination with the measurements. Even an anisotropic turbulence model such as that created by Mann [1994] is based on a set of assumptions, e.g. neutral atmospheric conditions, applicability in the surface layer, validity of Taylor's hypothesis, and it does not apply to complex terrain. If we then combine such a model with lidar measurements, and estimate turbulence parameters, then additional uncertainties may be introduced. In order to avoid such situations, further development of algorithms should also focus on making use of only raw lidar data to extract turbulence parameters, e.g., as shown in Mann et al. [2010].

2. Improvement in lidar technology – New, cheaper solid-state lasers for coherent detection lidars with integrated optical amplification are being developed and tested [Hansen

and Pedersen, 2008, Rodrigo and Pedersen, 2008]. These may greatly expand the use of lidars for wind measurements, but they are not specifically tailored for turbulence measurements. Preliminary tests of these lidars have been carried out by Rodrigo and Pedersen [2012], and show good comparison with a sonic anemometer. The solid-state lasers with integrated amplification may in the near future compete with the more expensive lasers used in C-W Doppler lidars. Direct detection is still on an experimental level [McKay, 1998] and has only been used in the atmosphere sporadically [Dors et al., 2011, Xia et al., 2007]. The simple design of these instruments may eventually lead to cheaper lidar systems. Non-coherent detection may also provide possible new ways to estimate atmospheric turbulence [Mayor et al., 2012, Sela and Tsadka, 2011], but to our knowledge it does not, so far, challenge the capabilities of the coherent Doppler lidars.

Completely new principles could also drastically improve the turbulence-measuring capabilities of lidars. One suggestion is to exploit the translation of the speckle pattern in the image plane of the lidar telescope. In this way, not only the line-of-sight velocity could be estimated, but also the two transverse velocity components. All components would be measured in the same volume, reducing the problem of cross-contamination. In the laboratory, this method has been successfully tested on translating hard targets [Iversen et al., 2011, Jakobsen et al., 2011], but it is much harder to get the method to work with backscatter from atmospheric aerosols. Firstly, the return from the aerosols is much weaker and, secondly, the turbulence may reduce the correlation time of the speckle pattern, which could adversely affect the transverse velocity determination.

Bibliography

M. Abramowitz and I A. Stegun, editors. *Handbook of Mathematical Functions*. Dover Publications, INC., New York, 9^{th} edition, 1965. ISBN 0-486-61272-4.

N. Angelou, J. Mann, M. Sjöholm, and M. Courtney. Direct measurement of the spectral transfer function of a laser based anemometer. *Review of Scientific Instruments*, 83(3): 033111, 7 pp., 2012. doi: 10.1063/1.3697728.

W. Baker. Can lidars measure turbulence? comparison between zephir 300 and an iec compliant anemometer mast. In *Proceedings EWEA*, Copenhagen, Denmark, 2012. ZephIR Ltd., EWEA.

V A. Banakh and I N. Smalikho. Determination of the turbulent energy dissipation rate from lidar sensing data. *Atmospheric and Oceanic Optics*, 10(4–5):295–302, 1997a.

V A. Banakh and I N. Smalikho. Estimation of the turbulence energy dissipation rate from the pulsed Doppler lidar data. *Atmospheric and Oceanic Optics*, 10(12):957–965, 1997b.

V A. Banakh and C. Werner. Computer simulation of coherent Doppler lidar measurement of wind velocity and retrieval of turbulent wind statistics. *Optical Engineering*, 44(7):071205, 19 pages, 2005. doi: 10.1117/1.1955167.

V A. Banakh, I N. Smalikho, F. Köpp, and C. Werner. Representativeness of wind measurements with a CW Doppler lidar in the atmospheric boundary layer. *Applied optics*, 34(12): 2055–2067, 1995a. doi: 10.1364/AO.34.002055.

V A. Banakh, C. Werner, N N. Kerkis, F. Köpp, and I N. Smalikho. Turbulence measurements with a CW Doppler lidar in the atmospheric boundary layer. *Atmospheric and Oceanic Optics*, 8(12):955–959, 1995b.

V A. Banakh, C. Werner, F. Köpp, and I N. Smalikho. Measurement of turbulent energy dissipation rate with a scanning Doppler lidar. *Atmospheric and Oceanic Optics*, 9(10): 849–853, 1996.

V A. Banakh, C. Werner, F. Köpp, and I N. Smalikho. Fluctuation spectra of wind velocity measured with a Doppler lidar. *Atmospheric and Oceanic Optics*, 10(3):202–208, 1997.

V A. Banakh, I N. Smalikho, F. Köpp, and C. Werner. Measurements of turbulent energy dissipation rate with a CW Doppler lidar in the atmospheric boundary layer. *Journal of Atmospheric and Oceanic Technology*, 16(8):1044–1061, 1999. doi: 10.1175/1520-0426(1999)016<1044:MOTEDR>2.0.CO;2.

V A. Banakh, I N. Smalikho, Y L. Pichugina, and W A. Brewer. Representativeness of measurements of the dissipation rate of turbulence energy by scanning Doppler lidar. *Atmospheric and Oceanic Optics*, 23(1):48–54, 2010. doi: 10.1134/S1024856010010100.

R M. Banta. Stable-Boundary-Layer regimes from the perspective of the low-level jet. *Acta Geophysica*, 56(1):58–87, 2008. doi: 10.2478/s11600-007-0049-8.

R M. Banta, L D. Olivier, E T. Holloway, R A. Kropfli, B W. Bartram, R E. Cupp, and M J. Post. Smoke-Column Observations from Two Forest Fires Using Doppler Lidar and Doppler Radar. *Journal of Applied Meteorology*, 31(11):1328–1349, 1992. doi: 10.1175/1520-0450(1992)031<1328:SCOFTF>2.0.CO;2.

R M. Banta, L D. Olivier, and D H. Levinson. Evolution of the Monterey Bay Sea-Breeze Layer As Observed by Pulsed Doppler Lidar. *Journal of the Atmospheric Sciences*, 50(24): 3959–3982, 1993. doi: 10.1175/1520-0469(1993)050<3959:EOTMBS>2.0.CO;2.

R M. Banta, L S. Darby, P. Kaufmann, D H. Levinson, and C-J. Zhu. Wind-Flow Patterns in the Grand Canyon as Revealed by Doppler Lidar. *Journal of Applied Meteorology*, 38 (8):1069–1083, 1999. doi: 10.1175/1520-0450(1999)038<1069:WFPITG>2.0.CO;2.

R M. Banta, R K. Newsom, J K. Lundquist, Y L. Pichugina, R L. Coulter, and L. Mahrt. Nocturnal low-level jet characteristics over Kansas during CASES-99. *Boundary-Layer Meteorology*, 105(2):221–252, 2002. doi: 10.1023/A:1019992330866.

R M. Banta, Y L. Pichugina, and W A. Brewer. Turbulent velocity-variance profiles in the stable boundary layer generated by a nocturnal low-level jet. *Journal of Atmospheric Sciences*, 63(11):2700–2719, 2006. doi: 10.1175/JAS3776.1.

R M. Banta, Y L. Pichugina, N D. Kelly, R M. Hardesty, and W A. Brewer. Wind Energy Meteorology: Insight into wind properties in the turbine-rotor layer of the atmosphere from high-resolution Doppler lidar. *Bulletin of American Meteorological Society*, 94(6):883–902, 2013. doi: 10.1175/BAMS-D-11-00057.1.

A. Bechmann, N N. Sørensen, J. Berg, J. Mann, and P.-E. P-E. Rèthorè. The bolund experiment, part ii: Blind comparison of microscale flow models. *Boundary-Layer Meteorology*, 141(2):245–271, 2011. doi: 10.1007/s10546-011-9637-x.

E. Branlard, A T. Pedersen, J. Mann, N. Angelou, A. Fischer, T. Mikkelsen, M. Harris, C. Slinger, and B F. Montes. Retrieving wind statistics from average spectrum of continuous-wave lidar. *Atmospheric Measurement Techniques*, 6(7):1673–1683, 2013. doi: 10.5194/amt-6-1673-2013.

T. Burton, D. Sharpe, N. Jenkins, and E. Bossanyi. *Wind Energy Handbook*. John Wiley and Sons, LTD, 2001.

B. Canadillas, A. Bégué, and T. Neumann. Comparison of turbulence spectra derived from LiDAR and sonic measurements at the offshore platform FINO1. In *DEWEK 2010,* 10^{th} *German Wind Energy Conference*, Bremen, Germany, 2010.

Jean-Pierre Cariou. Pulsed lidars. In *Remote Sensing for Wind Energy, DTU Wind Energy-E-Report-0029(EN)*, chapter 5, pages 104–121. June 2013.

P W. Chan. Generation of an eddy dissipation rate map at the Hong Kong international airport based on Doppler lidar data. *Journal of Atmospheric and Oceanic Technology*, 28 (1):37–49, 2011. doi: 10.1175/2010JTECHA1458.1.

H. Charnock. Wind stress over a water surface. *Quarterly Journal of Royal Meteorological Society*, 81(350):639–640, 1955.

S A. Cohn, S D. Mayor, C J. Grund, T M. Weckwerth, and C. Senff. The lidars in flat terrain (LIFT) experiment. *Bulletin of the American Meteorological Society*, 79(7):1329–1343, 1998. doi: 10.1175/1520-0477(1998)079<1329:TLIFTL>2.0.CO;2.

C G. Collier, F. Davies, K E. Bozier, A R. Holt, D R. Middleton, G N. Pearson, S. Siemen, D V. Willetts, G J G. Upton, and R I. Young. Dual-Doppler lidar measurements for improving dispersion models. *Bulletin of American Meteorological Society*, 86(6):825–838, 2005. doi: 10.1175/BAMS-86-6-825.

L S. Darby, W D. Neff, and R M. Banta. Multiscale Analysis of a Meso-β Frontal Passage in the Complex Terrain of the Colorado Front Range. *Monthly Weather Review*, 127(9): 2062–2082, 1999. doi: 10.1175/1520-0493(1999)127<2062:MAOAMF>2.0.CO;2.

L S. Darby, K J. Allwine, and R M. Banta. Nocturnal Low-Level Jet in a Mountain Basin Complex. Part II: Transport and Diffusion of Tracer under Stable Conditions. *Journal of Applied Meteorology and Climatology*, 45(5):740–753, 2006. doi: 10.1175/JAM2367.1.

F. Davies, C G. Collier, K E. Bozier, and G N. Pearson. On the accuracy of retrieved wind information from Doppler lidar observation. *Quarterly Journal of the Royal Meteorological Society*, 129(587):321–334, 2003. doi: 10.1256/qj.01.126.

F. Davies, C G. Collier, G N. Pearson, and K E. Bozier. Doppler lidar measurements of turbulent structure function over an urban area. *Journal of Atmospheric and Oceanic Technology*, 21(5):753–761, 2004. doi: 10.1175/1520-0426(2004)021<0753:DLMOTS>2.0.CO;2.

F. Davies, C G. Collier, and K E. Bozier. Errors associated with dual-Doppler-lidar turbulence measurements. *Journal of Optics A: Pure and Applied Optics*, 7(6):S280–S289, 2005. doi: 10.1088/1464-4258/7/6/005.

G N. Davies and C G. Collier. A pulsed coherent CO_2 lidar boundary layer meteorology. *Quarterly Journal of the Royal Meteorological Society*, 125(559):2703–2721, 1999. doi: 10.1002/qj.49712555918.

J C. Davis, C G. Collier, F. Davies, and K E. Bozier. Spatial variations of sensible heat flux over an urban area measured using Doppler lidar. *Meteorological Applications*, 15(3): 367–380, 2008. doi: 10.1002/met.79.

I. Dors, J P. McHugh, G Y. Jumper, and J. Roadcap. Velocity spectra and turbulence using direct detection lidar and comparison with thermosonde measurements. *Journal of Geophysical Research*, 116(D1):D01102, 1–12, 2011. doi: 10.1029/2010JD014606.

P. Drobinski, R A. Brown, P H. Flamant, and J. Pelon. Evidence of organized large eddies by ground-based Doppler lidar, sonic anemometer and sodar. *Boundary-Layer Meteorology*, 88 (3):343–361, 1998. doi: 10.1023/A:1001167212584.

P. Drobinski, A M. Dabas, and P H. Flamant. Remote measurement of turbulent wind spectra by heterodyne Doppler lidar technique. *Journal of Applied Meteorology*, 39(12):2434–2451, 2000. doi: 10.1175/1520-0450(2000)039<2434:RMOTWS>2.0.CO;2.

P. Drobinski, P. Carlotti, R K. Newsom, R M. Banta, R C. Foster, and J-L. Redelsperger. The structure of the near-neutral atmospheric surface layer. *Journal of Atmospheric Sciences*, 61(6):699–714, 2004. doi: 10.1175/1520-0469(2004)061<0699:TSOTNA>2.0.CO;2.

W L. Eberhard, R E. Cupp, and K R. Healy. Doppler lidar measurements of profiles of turbulence and momentum flux. *Journal of Atmospheric and Oceanic Technology*, 6(5): 809–819, 1989. doi: 10.1175/1520-0426(1989)006<0809:DLMOPO>2.0.CO;2.

R. Frehlich. Effects of wind turbulence on coherent Doppler lidar performance. *Journal of Atmospheric and Oceanic Technology*, 14(1):54–75, 1997. doi: 10.1175/1520-0426(1997)014<0054:EOWTOC>2.0.CO;2.

R. Frehlich. Estimation of velocity error for doppler lidar measurements. *Journal of Atmospheric and Oceanic Technology*, 18(10):1628–1639, 2001. doi: 10.1175/1520-0426(2001)018<1628:EOVEFD>2.0.CO;2.

R. Frehlich and L. Cornman. Estimating spatial velocity statistics with coherent Doppler lidar. *Journal of Atmospheric and Oceanic Technology*, 19(3):355–366, 2002. doi: 10.1175/1520-0426-19.3.355.

R. Frehlich and N. Kelley. Measurements of wind and turbulence profiles with scanning Doppler lidar for wind energy applications. *IEEE Journal of Selected Topics in Applied Earth Observations and Remote Sensing*, 1(1):42–47, 2008. doi: 10.1109/JSTARS.2008.2001758.

R. Frehlich, S M. Hannon, and S W. Henderson. Performance of a 2-μm coherent Doppler lidar for wind measurements. *Journal of Atmospheric and Oceanic Technology*, 11(6):1517–1528, 1994. doi: 10.1175/1520-0426(1994)011<1517:POACDL>2.0.CO;2.

R. Frehlich, S M. Hannon, and S W. Henderson. Coherent Doppler lidar measurements of wind field statistics. *Boundary-Layer Meteorology*, 86(2):233–256, 1998. doi: 10.1023/A:1000676021745.

R. Frehlich, Y. Meillier, M L. Jensen, B. Balsley, and R. Sharman. Measurements of boundary layer profiles in urban environment. *Journal of Applied Meteorology and Climatology*, 45(6):821–837, 2006. doi: 10.1175/JAM2368.1.

R. Frehlich, Y. Meillier, and M L. Jensen. Measurements of boundary layer profiles with in situ sensors and Doppler lidar. *Journal of Atmospheric and Oceanic Technology*, 25(8): 1328–1340, 2008. doi: 10.1175/2007JTECHA963.1.

T. Gal-Chen, M. Xu, and W L. Eberhard. Estimation of atmospheric boundary layer fluxes and other turbulence parameters from Doppler lidar data. *Journal of Geophysical Research*, 97(D17):18,409–18,423, 1992. doi: 10.1029/91JD03174.

J. Gottschall and J. Peinke. How to improve the estimation of power curves for wind turbines. *Environmental Research Letters*, 3(1):015005, 7 pages, 2008. doi: 10.1088/1748-9326/3/1/015005.

C J. Grund, R M. Banta, J L. George, J N. Howell, M J. Post, R A. Richter, and A M. Weickmann. High-Resolution Doppler lidar for boundary layer and cloud research. *Journal of Atmospheric and Oceanic Technology*, 18(3):376–393, 2001. doi: 10.1175/1520-0426(2001)018<0376:HRDLFB>2.0.CO;2.

F F. Hall, R M. Huffaker, R M. Hardesty, M E. Jackson, T R. Lawrence, M J. Post, R A. Richter, and B F. Weber. Wind measurement accuracy of the noaa pulsed infrared doppler lidar. *Applied Optics*, 23(15):2503–2506, 1984. doi: 10.1364/AO.23.002503.

R S. Hansen and C. Pedersen. All semiconductor laser doppler anemometer at 1.55 μm. *Optics Express*, 16(22):18288–18295, 2008. doi: 10.1364/OE.16.018288.

R M. Hardesty, J A. Korrell, and F F. Hall. Lidar measurement of wind velocity turbulence spectra encountered by a rotating turbine blade. Technical Report DOE/RL/10236-81/1, National Oceanic and Atmospheric Administration, Boulder, CO (USA), 1982.

IEC. IEC 61400-1. Wind turbines – Part 1: Design Requirements. International standard, International Electrotechnical Commission, Geneva, Switzerland, 2005a.

IEC. IEC61400-12. Wind turbines-Part 12-1: Power performance measurements of electricity producing wind turbines. International standard, International Electrotechnical Commission, Geneva, Switzerland, 2005b.

T F Q. Iversen, M L. Jakobsen, and S G. Hanson. Speckle-based three-dimensional velocity measurement using spatial filtering velocimetry. *Applied Optics*, 50(11):1523–1533, 2011. doi: 10.1364/AO.50.001523.

M L. Jakobsen, T F Q. Iversen, H T. Yura, and S G. Hanson. Speckle and fringe dynamics in imaging speckle-pattern interferometry for spatial-filtering velocimetry. *Applied optics*, 50(28):5577–5591, 2011. doi: 10.1364/AO.50.005577.

International vocabulary of metrology - Basic and general concepts and associated terms (VIM). JCGM, 3 edition, 2008.

J C. Kaimal, J C. Wyngaard, Y. Izumi, and O R. Coté. Spectral characteristics of surface-layer turbulence. *Quarterly Journal of the Royal Meteorological Society*, 98(417):563–589, 1972. doi: 10.1002/qj.49709841707.

K. Kaiser, W. Langreder, H. Hohlen, and J. Højstrup. Turbulence correction for power curves. In J. Peinke, P. Schaumann, and S. Barth, editors, *Wind Energy, Proceedings of the Euromech Colloquium*, pages 159–162. Springer, 2007.

N. Kelley, M. Shirazi, D. Jager, S. Wilde, J. Adams, M. Buhl, P. Sullivan, and E. Patton. Lamar low-level jet project interim report. Technical Report NREL/TP-500-34593, National Renewable Energy Laboratory, Colorado, USA, January 2004.

D. Kindler, A. Oldroyd, A. Macaskill, and D. Finch. An eight month test campaign of the QinetiQ ZephIR system: Preliminary results. *Meteorologische Zeitschrift*, 16(5):479–489, 2007. doi: 10.1127/0941-2948/2007/0226.

T. Klaas, L. Pauscher, and D. Callies. A comparison of lidar and mast measurements in complex terrain and its simulation using cfd. *Meteorologische Zeitschrift*, 2015. Accepted.

L. Kristensen, D H. Lenschow, P. Kirkegaard, and M. Courtney. The spectral velocity tensor for homogeneous boundary-layer turbulence. *Boundary-Layer Meteorology*, 47(1–4):149–193, 1989. doi: 10.1007/BF00122327.

L. Kristensen, P. Kirkegaard, J.Mann, T. Mikkelsen, M. Nielsen, and M. Sjöholm. Spectral coherence along a Lidar-Anemometer beam. Technical Report Risø -R-1744(EN), Risø DTU, 2010.

L. Kristensen, P. Kirkegaard, and T. Mikkelsen. Determining the velocity fine structure by a laser anemometer with fixed orientation. Technical Report Risø -R-1762(EN), Risø DTU, 2011.

L. Kristensen, P. Kirkegaard, and T. Mikkelsen. Determining the velocity fine structure by a laser anemometer in VAD operation. Technical Report DTU Wind Energy E-0008(EN), DTU Wind Energy, Lyngby, Denmark, 2012.

K E. Kunkel, E W. Eloranta, and J A. Weinman. Remote determination of winds, turbulence spectra and energy dissipation rates in the boundary layer from lidar measurements. *Journal of Atmospheric Sciences*, 37(5):978–985, 1980. doi: 10.1175/1520-0469(1980)037<0978:RDOWTS>2.0.CO;2.

S. Lang and E. McKeogh. Lidar and sodar measurements of wind speed and direction in upland terrain for wind energy purposes. *Remote Sensing*, 3(9):1871–1901, 2011. doi: 10.3390/rs3091871.

G C. Larsen, H A. Madsen, K. Thomsen, and T J. Larsen. Wake Meandering: A pragmatic approach. *Wind Energy*, 11(4):377–395, 2008. doi: 10.1002/we.267.

T R. Lawrence, D J. Wilson, C E. Craven, I P. Jones, R M. Huffaker, and J A L. Thomson. A laser velocimeter for remote wind sensing. *Review of Scientific Instruments*, 43(3):512–518, 1972. doi: 10.1063/1.1685674.

D H. Lenschow, J. Mann, and L. Kristensen. How long is long enough when measuring fluxes and other turbulence statistics? *Journal of Atmospheric and Oceanic Technology*, 11:661–673, 1994. doi: 10.1175/1520-0426(1994)011<0661:HLILEW>2.0.CO;2.

D H. Lenschow, V. Wulfmeyer, and C. Senff. Measuring second- through fourth-order moments in noisy data. *Journal of Atmospheric and Oceanic technology*, 17(10):1330–1347, 2000. doi: 10.1175/1520-0426(2000)017<1330:MSTFOM>2.0.CO;2.

P. Lindelöw-Marsden. UpWind D1. Uncertainties in wind assessment with LIDAR. Technical Report Risø-R-1681(EN), Risø DTU, 2009.

M. Lothon, D H. Lenschow, and S D. Mayor. Coherence and scale of vertical velocity in the convective boundary layer from a Doppler lidar. *Boundary-Layer Meteorology*, 121(3):521–536, 2006. doi: 10.1007/s10546-006-9077-1.

M. Lothon, D H. Lenschow, and S D. Mayor. Doppler lidar measurements of vertical velocity spectra in the convective planetary boundary layer. *Boundary-Layer Meteorology*, 132(2):205–226, 2009. doi: 10.1007/s10546-009-9398-y.

J. Mann. The spatial structure of neutral atmospheric surface-layer turbulence. *Journal of Fluid Mechanics*, 273:141–168, 1994. ISSN 0022-1120. doi: 10.1017/S0022112094001886.

J. Mann, J. Cariou, M. Courtney, R. Parmentier, T. Mikkelsen, R. Wagner, P. Lindelow, M. Sjöholm, and K. Enevoldsen. Comparison of 3D turbulence measurements using three staring wind lidars and a sonic anemometer. *Meteorologische Zeitschrift*, 18(2, Sp. Iss. SI):135–140, 2009. doi: 10.1127/0941-2948/2009/0370.

J. Mann, A. Peña, F. Bingöl, R. Wagner, and M S. Courtney. Lidar scanning of momentum flux in and above the surface layer. *Journal of Atmospheric and Oceanic Technology*, 27(6):792–806, 2010. doi: 10.1175/2010JTECHA1389.1.

S D. Mayor, D H. Lenschow, R L. Schwiesow, J. Mann, C L. Frush, and M K. Simon. Validation of NCAR 10.6-μm CO_2 Doppler lidar radial velocity measurements and comparison with a 915-MHz profiler. *Journal of Atmospheric and Oceanic Technology*, 14(5):1110–1126, 1997. doi: 10.1175/1520-0426(1997)014<1110:VONMCD>2.0.CO;2.

S D. Mayor, J P. Lowe, and C F. Mauzey. Two-component horizontal aerosol motion vectors in the atmospheric surface layer from a cross-correlation algorithm applied to scanning elastic backscatter lidar data. *Journal of Atmospheric and Oceanic Technology*, 29(11):1585–1602, 2012. doi: 10.1175/JTECH-D-11-00225.1.

J A. McKay. Modeling of direct detection Doppler wind lidar. I. The edge technique . *Applied Optics*, 37(27):6480–6486, 1998. doi: 10.1364/AO.37.006480.

T. Mikkelsen, N. Angelou, K. Hansen, M. Sjöholm, M. Harris, C. Slinger, P. Hadley, R. Scullion, G. Ellis, and G. Vives. A spinner-integrated wind lidar for enhanced wind turbine control. *Wind Energy*, 16(4):625–643, 2013. doi: 10.1002/we.1564.

R K. Newsom and R M. Banta. Shear-Flow Instability in the Stable Nocturnal Boundary Layer as Observed by Doppler Lidar during CASES-99. *Journal of the Atmospheric Sciences*, 60 (1):16–33, 2003. doi: 10.1175/1520-0469(2003)060<0016:SFIITS>2.0.CO;2.

R K. Newsom and R M. Banta. Assimilating coherent Doppler lidar measurements into a model of the atmospheric boundary layer. Part I: Algorithm development and sensitivity to measurement error. *Journal of Atmospheric and Oceanic Technology*, 21(9):1328–1345, 2004a. doi: 10.1175/1520-0426(2004)021<1328:ACDLMI>2.0.CO;2.

R K. Newsom and R M. Banta. Assimilating coherent Doppler lidar measurements into a model of the atmospheric boundary layer. Part II: Sensitivity analyses. *Journal of Atmospheric and Oceanic Technology*, 21(12):1809–1824, 2004b. doi: 10.1175/JTECH-1676.1.

R K. Newsom, L K. Berg, W J. Shaw, and M L. Fischer. Turbine-scale wind field measurements using dual-Doppler lidar. *Wind Energy*, 18(2):219–235, 2015. doi: 10.1002/we.1691.

E J. O'Connor, A J. Illingworth, I M. Brooks, C D. Westbrook, R J. Hogan, F. Davies, and B J. Brooks. A method for estimating the turbulent kinectic energy dissipation rate from a vertically pointing Doppler lidar, and independent evaluation from balloon-borne in situ measurements. *Journal of Atmospheric and Oceanic Technology*, 27(10):1652–1664, 2010. doi: 10.1175/2010JTECHA1455.1.

H A. Panofsky and J A. Dutton. *Atmospheric Turbulence*. John Wiley & Sons, New York, 1984.

A. Peña, S-E. Gryning, and C B. Hasager. Measurement and modelling of the wind speed profile in the marine atmospheric boundary layer. *Boundary-Layer Meteorology*, 129(3): 479–495, 2008. doi: 10.1007/s10546-008-9323-9.

A. Peña, C B. Hasager, S-E. Gryning, M. Courtney, I. Antoniou, and T. Mikkelsen. Offshore wind profiling using light detection and ranging measurements. *Wind Energy*, 12(2):105–124, 2009. doi: 10.1002/we.283.

A. Peña, S-E. Gryning, and J. Mann. On the length scale of the wind profile. *Quarterly Journal of the Royal Meteorological Society*, 136(653):2119–2131, 2010. doi: 10.1002/qj.714.

Y L. Pichugina and R M. Banta. Stable boundary layer depth from high resolution measurements of the mean wind profile. *Journal of Applied Meteorology and Climatology*, 49(1): 20–35, 2010. doi: 10.1175/2009JAMC2168.1.

Y L. Pichugina, R M. Banta, N D. Kelly, B. J. Jonkman, S C. Tucker, R K. Newsom, and W A. Brewer. Horizontal-velocity and variance measurements in the stable boundary layer using Doppler lidar: Sensitivity to averaging procedures. *Journal of Atmospheric and Oceanic Technology*, 25(8):1307–1327, 2008. doi: 10.1175/2008JTECHA988.1.

R A. Pielke and H A. Panofsky. Turbulence characteristics along several towers. *Boundary-Layer Meteorology*, 1:115–130, 1970. doi: 10.1007/BF00185733.

M. Pitter, C. Abvien, K. Vogstad, M. Harris, W. Barker, and O. Braduy. Lidar and computational fluid dynamics for resource assessment in complex terrain. In *Proceedings EWEA*, Copenhagen, Denmark, 2012. EWEA.

S B. Pope. *Turbulent Flows*. Cambridge University Press, New York, 2000. ISBN 978-0-521-59886-6.

G S. Poulos, W. Blumen, D C. Fritts, J K. Lundquist, J. Sun, S P. Burns, C. Nappo, R. Banta, R. Newsom, J. Cuxart, E. Terradellas, B. Balsley, and M. Jensen. CASES-99: A comprehensive investigation of the stable nocturnal boundary layer. *Bulletin of American Meteorological Society*, 83(4):555–581, 2002. doi: 10.1175/1520-0477(2002)083<0555:CACIOT>2.3.CO;2.

A. Rettenmeier, O. Bischoff, D. Schlipf, J. Anger, M. Hofsäß, P W. Cheng, R. Wagner, M. Courtney, and J. Mann. Turbulence and wind speed investigations using a nacelle-based lidar scanner and a met mast. In *Presentation at the European Wind Energy Association annual event*, Copenhagen, Denmark, 2012.

P J. Rodrigo and C. Pedersen. Reduction of phase-induced intensity noise in a fiber-based coherent doppler lidar using polarization control. *Optics Express*, 18(5):5320–5327, 2008. doi: 10.1364/OE.18.005320.

P J. Rodrigo and C. Pedersen. Field performance of an all-semiconductor laser coherent Doppler lidar. *Optics Letters*, 37(12):2277–2279, 2012. doi: 10.1364/OL.37.002277.

A. Sathe. *Influence of wind conditions on wind turbine loads and measurement of turbulence using lidars*. PhD Thesis, Delft University of Technology, 2012.

A. Sathe and J. Mann. Measurement of turbulence spectra using scanning pulsed wind lidars. *Journal of Geophysical Research*, 117(D1):D01201, 11 PP., 2012. doi: 10.1029/2011JD016786.

A. Sathe and J. Mann. A review of turbulence measurements using ground-based wind lidars. *Atmospheric Measurement Techniques*, 6(11):3147–3167, 2013. doi: 10.5194/amt-6-3147-2013.

A. Sathe, S-E. Gryning, and A. Peña. Comparison of the atmospheric stability and wind profiles at two wind farm sites over a long marine fetch in the North Sea. *Wind Energy*, 14 (6):767–780, 2011a. doi: 10.1002/we.456.

A. Sathe, J. Mann, J. Gottschall, and M S. Courtney. Can wind lidars measure turbulence? *Journal of Atmospheric and Oceanic Technology*, 28(7):853–868, 2011b. doi: 10.1175/JTECH-D-10-05004.1.

A. Sathe, J. Mann, T. Barlas, W A A M. Bierbooms, and G J W. van Bussel. Influence of atmospheric stability on wind turbine loads. *Wind Energy*, 16(7):1013–1032, 2013. doi: 10.1002/we.1528.

A. Sathe, J. Mann, N. Vasiljevic, and G. Lea. A six-beam method to measure turbulence statistics using ground-based wind lidars. *Atmospheric Measurement Techniques*, 8(2):729–740, 2015. doi: 10.5194/amt-8-729-2015.

D. Schlipf. *Lidar-Assisted Control Concepts for Wind Turbines.* PhD thesis, University of Stuttgart, under review, 2015.

D. Schlipf, A. Rettenmeier, F. Haizmann, M. Hofsäß, M. Courtney, and P W. Cheng. Model based wind vector field reconstruction from lidar data. In *Proceedings of the German Wind Energy Conference DEWEK*, Bremen, Germany, 2012.

D. Schlipf, D J. Schlipf, and M. Kühn. Nonlinear model predictive control of wind turbines using LIDAR. *Wind Energy*, 16(7):1107–1129, 2013. doi: 10.1002/we.1533.

D. Schlipf, F. Haizmann, N. Cosack, T. Siebers, and P W. Cheng. Detection of wind evolution and lidar trajectory optimization for lidar-assisted wind turbine control. *Meteorologische Zeitschrift, in press*, 2015.

N. Sela and S. Tsadka. System for monitoring wind characteristics to install wind turbines for generating electricity, has data processing subsystem for receiving data from laser anemometers and providing output data that represents wind characteristics. Patent no WO2011036553-A1, 2011.

E. Simley and L Y. Pao. A longitudinal spatial coherence model for wind evolution based on large-eddy simulation. In *Proceedings of the American Control Conference*, Chicago, USA, 2015.

E. Simley, L Y. Pao, R. Frehlich, B. Jonkman, and N. Kelley. Analysis of light detection and ranging wind speed measurements for wind turbine control. *Wind Energy*, 2013. doi: 10.1002/we.1584. Early online view.

M. Sjöholm, T. Mikkelsen, J. Mann, K. Enevoldsen, and M. Courtney. Spatial averaging-effects on turbulence measured by a continuous-wave coherent lidar. *Meteorologische Zeitschrift*, 18(3, Sp. Iss. SI):281–287, 2009. doi: 10.1127/0941-2948/2009/0379.

I. Smalikho, F. Kopp, and S. Rahm. Measurement of atmospheric turbulence by 2-μm Doppler lidar. *Journal of Atmospheric and Oceanic Technology*, 22(11):1733–1747, 2005. doi: 10.1175/JTECH1815.1.

I N. Smalikho. On measurement of dissipation rate of the turbulent energy with a CW Doppler lidar. *Atmospheric and Oceanic Optics*, 8(10):788–793, 1995.

D A. Smith, M. Harris, A S. Coffey, T. Mikkelsen, H E. Jørgensen, J. Mann, and R. Danielian. Wind lidar evaluation at the Danish wind test site in Høvsøre. *Wind Energy*, 9:87–93, 2006. doi: 10.1002/we.193.

C M. Sonnenschein and F A. Horrigan. Signal-to-noise relationships for coaxial systems that heterodyne backscatter from atmosphere. *Applied optics*, 10(7):1600, 1971. doi: 10.1364/AO.10.001600.

R B. Stull. *An Introduction to Boundary Layer Meteorology.* Kluwer Academic Publishers, 1988. ISBN 90-277-2768-6.

G I. Taylor. The spectrum of turbulence. *Proceedings of the Royal Society of London. Series A, Mathematical and Physical*, 164(919):476–490, 1938.

R. Thresher, W. Holley, C. Smith, N. Jafarey, and S-R. Lin. Modeling the response of wind turbines to atmospheric turbulence. Technical Report RL0/2227-81/2, Department of Mechanical Engineering, Oregon State University, 1981.

S C. Tucker, W A. Brewer, R M. Banta, C J. Senff, S P. Sandberg, D C. Law, M. Weickmann, and R M. Hardesty. Doppler lidar estimation of mixing height using turbulence, shear and aerosol profiles. *Journal of Atmospheric and Oceanic Technology*, 26(4):673–688, 2009. doi: 10.1175/2008JTECHA1157.1.

M. Valla. *Etude d'un lidar doppler impulsionnel à laser Erbium fibré pour des mesures de champ de vent dans la couche limite de l'atmosphère*. PhD. Thesis, L'ècole Tèlècom ParisTech, 2005.

N. Vasiljevic. A time-space synchronization of coherent doppler scanning lidars for 3d measurements of wind fields. Ph.D. Thesis PhD-0027 (EN), Technical University of Denmark, 2014.

D. Vickers and L. Mahrt. The cospectral gap and turbulent flux calculations. *Journal of Atmospheric and Oceanic Technology*, 20(5):660–672, 2003. doi: 10.1175/1520-0426(2003)20<660:TCGATF>2.0.CO;2.

D. Vickers and L. Mahrt. A solution for flux contamination by mesoscale motions with very weak turbulence. *Boundary-Layer Meteorology*, 118(3):431–447, 2006. doi: 10.1007/s10546-005-9003-y.

K. Vogstad, A H. Simonsen, K. Brennan, and J A. Lund. Uncertainty of lidars in complex terrain. In *Proceedings EWEA 2013*, Vienna, Austria, 2013. EWEA.

T. von Kármán. Progress in the statistical theory of turbulence. In *Proceedings of National Academy of Sciences, USA*, volume 34, pages 530–539. California Institute of Technology, Pasadena, June 1948.

R. Wagner, T. Mikkelsen, and M. Courtney. Investigation of turbulence measurements with a continuous wave, conically scanning lidar. Technical Report Risø-R-1682(EN), Risø DTU, 2009.

R. Wagner, M. Courtney, J. Gottschall, and P. Lindelöw-Marsden. Accounting for the speed shear in wind turbine power performance measurement. *Wind Energy*, 14(8):993–1004, 2011. doi: 10.1002/we.509.

J M. Wilczak, E E. Gossard, W D. Neff, and W L. Eberhard. Ground-based remote sensing of the atmospheric boundary layer: 25 years of progress. *Boundary-Layer Meteorology*, 78(3–4):321–349, 1996. doi: 10.1007/BF00120940.

J M. Wilczak, S P. Oncley, and S A. Stage. Sonic anemometer tilt correction algorithms. *Boundary-Layer Meteorology*, 99(1):127–150, 2001. doi: 10.1023/A:1018966204465.

J C. Wyngaard. *Turbulence in the Atmosphere*. Cambridge University Press, New York, 2010. ISBN 978-0-521-88769-4.

H. Xia, D. Sun, Y. Yang, F. Shen, J. Dong, and T. Koboyashi. Fabry-perot interferometer based mie doppler lidar for low tropospheric wind observation. *Applied Optics*, 46(29):7120–7131, 2007. doi: 10.1364/AO.46.007120.

List of Participants

No.	Name	Company/Institute	Country
1	Ameya Sathe	DTU Wind Energy	Denmark
2	Michael Courtney	DTU Wind Energy	Denmark
3	Rozenn Wagner	DTU Wind Energy	Denmark
4	Nicolai Nygaard	DONG Energy	Denmark
5	Andrew Clifton	NREL	USA
6	Robert Banta	NOAA	USA
7	Klaus Vogstad	Meventus	Norway
8	Valerie Kumer	University of Bergen	Norway
9	Lukas Pauscher	Fraunhofer IWES	Germany
10	Tobias Klaas	Fraunhofer IWES	Germany
11	Julia Gottschall	Fraunhofer IWES	Germany
12	David Schlipf	University of Stuttgart	Germany
13	Florian Haizmann	University of Stuttgart	Germany
14	Beatriz Canadillas	DEWI	Germany
15	Carolin Schmitt	Juwi	Germany
16	David Hilbert	Senvion	Germany
17	Matthieu Boquet	Leosphere	France
18	Jonathan Chauvin	IFP Energies Nouvelles	France
19	Mike Harris	ZephIR Ltd.	UK
20	Scott Wylie	ZephIR Ltd.	UK
21	Peter Clive	Sgurr Energy	UK
22	Will Barker	Sgurr Energy	UK
23	Andy Oldroyd	Oldbaum Services	UK
24	Rory Donnell	3E	Belgium
25	Lena Klasén	Windvector	Sweden

DTU Wind Energy
Department of Wind Energy
Technical University of Denmark

Frederiksborgvej 399
4000 Roskilde
www.vindenergi.dtu.dk/english